STABILITY AND CONTROL OF A COMPASS GAIT MODEL WALKING WITH SERIES-ELASTIC ANKLE ACTUATION

A DISSERTATION SUBMITTED TO

THE GRADUATE SCHOOL OF ENGINEERING AND SCIENCE

OF BILKENT UNIVERSITY

IN PARTIAL FULFILLMENT OF THE REQUIREMENTS FOR

THE DEGREE OF

DOCTOR OF PHILOSOPHY

IN

ELECTRICAL AND ELECTRONICS ENGINEERING

By
Deniz Kerimoğlu
November 2017

Stability and Control of a Compass Gait Model Walking with Series-Elastic Ankle Actuation
By Deniz Kerimoğlu
November 2017

We certify that we have read this dissertation and that in our opinion it is fully adequate, in scope and in quality, as a dissertation for the degree of Doctor of Philosophy.

_____
Ömer Morgül(Advisor)

_____
Uluç Saranlı(Co-Advisor)

_____
Hitay Özbay

_____
Melih Çakmakçı

_____
M. Kemal Leblebicioğlu

_____
Coşku Kasnakoğlu

Approved for the Graduate School of Engineering and Science:

_____
Ezhan Karaşan
Director of the Graduate School

ABSTRACT

STABILITY AND CONTROL OF A COMPASS GAIT MODEL WALKING WITH SERIES-ELASTIC ANKLE ACTUATION

Deniz Kerimoğlu
Ph.D. in Electrical and Electronics Engineering
Advisor: Ömer Morgül
Co-Advisor: Uluç Saranlı
November 2017

Passive dynamic walking models are capable of capturing basic properties of walking behaviors and can generate stable human-like walking without any actuation on downhill surfaces. The passive compass gait model is among the simplest of such models, consisting of a planar point mass and two stick legs. A number of different actuation methods have been proposed both for this model and its more complex extensions to eliminate the need for a downhill sloped ground, balancing collision losses using gravitational potential energy. In this thesis, we introduce and investigate an extended compass gait model with series-elastic actuation at the ankle towards a similar goal, realizing stable walking on various terrains such as level ground, inclined surfaces and rough terrains. Our model seeks to capture the basic structure of how humans utilize toe push-off prior to leg liftoff, and is intended to eventually be used for controlling the ankle joint in a lower-body robotic orthosis.

We derive hybrid equations of motion for this model and obtain limit cycle walking on level and inclined grounds. We then numerically identify fixed points of this system and and show numerically through Poincaré analysis that it can achieve asymptotically stable walking on level and inclined ground for certain choices of system parameters. The dependence of limit cycles and their stability on system parameters such as spring precompression and stiffness for level ground walking is identified by studying the bifurcation regimes of period doubling of this model, leading to chaotic walking patterns. We show that feedback control on the initial extension of the series ankle spring can be used to improve and extend system stability on level ground walking. Then, we investigate and identify the period doubling bifurcation regions of our model for spring precompression and ground slope parameter leading to various maps that we utilize for rough terrain

walking. Furthermore, we evaluate the performance of our model on rough terrains by applying ground slope feedback controllers on the spring precompression. Thereafter, we demonstrate that slope feedback along with stance leg apex velocity feedback control on the extension of the series ankle spring improves walking performance on rough terrains.

The implementation of series elastic actuation on the ankle joint is realized with an experimental instantiations of active ankle foot orthosis system for the patients walking unnaturally and inefficiently with impaired ankles. Finally, we integrate the active ankle foot orthosis platform with an active knee orthosis platform where the experimentation results indicate that the integrated platform can generate efficient walking patterns.

ÖZET

PERGEL YÜRÜME MODELİNİN BİLEKTE SERİ YAYLI EYLEYİCİ İLE DENETİMİ VE KONTROLÜ

Deniz Kerimoğlu
Elektrik ve Elektronik Mühendisliği, Doktora
Tez Danışmanı: Ömer Morgül
İkinci Tez Danışmanı: Uluç Saranlı
Kasım 2017

Pasif dinamik yürüme modelleri, eğimli yüzeylerde herhangi bir eyleyici olmaksızın insan benzeri bir yürüyüş sergileyebilen ve yürüme davranışının temel özelliklerini ifade edebilen modellerdir. Bunlar arasında en yaygın olanı, noktasal bir gövde ve iki bacaktan oluşan pasif pergel yürüyüş modelidir. Literatürde bu modele ve bu modelin gelişkin örneklerine eklenen çeşitli eyleyiciler ile eğimli yüzey gereksinimini ortadan kaldırarak yerçekim potensiyel enerjisi ile çarpışma kayıplarını dengeleyen çalışmalar mevcuttur. Bu tez çalışmasında, benzer bir amaca yönelik olarak, düz, eğimli ve engebeli yüzeylerde kararlı yürüyüş gerçekleştiren, ayak bileğinde seri-elastik eyleyici kullanılarak geliştirilmiş bir pergel yürüme modeli öne sürüp incelemekteyiz. Modelimiz insan yürüyüşünün topuk kalkışı fazında gerçekleşen itme eyleminin temel prensiplerini yakalamayı amaçlanmaktadır ve bir alt-vücut robotik ortezin ayak bileği kontrolünde kullanması hedeflenmektedir.

Modelin karma dinamik denklemlerini türeterek düz ve eğimli yüzeylerde limit çevrimi yürüme profilleri elde ettik. Ardından, sistemin sabit noktalarını nümerik yöntemlerle belirledik ve Poincaré analiziyle, çeşitli sistem parametreleri için modelin düz ve eğimli yüzeyde asimptotik kararlı bir şekilde yürüyebildiğini gösterdik. Modelin, kaotik yürüyüş profillerine kadar varan, periyot katlanarak çatallanma rejimlerini bularak düz zeminde yürüyüş için limit çevrimlerinin ve kararlılıklarının yay sıkışması ve yay sabiti gibi sistem parametrelerine bağlılığını belirledik. Bilekteki yay uzunluğu üzerine geribesleme denetleyicisi kullanarak düz zemin yürüyüşlerinde sistem kararlılığını geliştirebileceğimizi gösterdik. Ardından, modelimizi engebeli yüzeyde yürütmek amacıyla kullandığımız çeşitli fonksiyonları elde etmek için modelimizin yay sıkışması ve zemin eğimi parametrelerine bağlı periyot katlanarak çatallanma bölgelerini belirleyip inceledik.

Ayrıca, yay sıkışması üzerinde yüzey eğimi geribesleme denetleyicileri uygulayarak modelimizin engebeli yüzeylerdeki yürüyüş performansını değerlendirdik. Sonrasında, yay sıkışması üzerinde yüzey eğimi geribeslemesi ile birlikte temas bacağının tepe noktası hızının geribesleme denetleyicisi uygulayarak engebeli yüzeylerde yürüyüş performansının artırılabildiğini gösterdik.

Bilek rahatsızlığı dolayısıyla doğal ve verimli yürüyemeyen hastalar için bilek ekleminde seri elastik eyleyici bulunan deneysel aktif bilek ayak ortez platformu geliştirilmiştir. Son olarak, aktif bilek ayak orteziyle aktif diz ortezini entegre ettik ve gerçekleştirdiğimiz deney sonuçlarından görüleceği üzere entegre platform verimli yürüyüş profilleri oluşturabilmektedir.

Anahtar sözcükler: dinamik yürüme, pasif pergel yürüyüş, seri-elastik eyleyici, ayak bileği eyleyicisi, çatallanma analizi, geri-beslemeli kontrol, bilek ayak ortezi.

Acknowledgement

The last six years was truly an amazing journey for me and reaching to a successful end would not have been possible without the inspiration and support of many great people.

Firstly, I owe my deepest gratitudes to my supervisors, Ömer Morgül and Uluç Saranlı for their guidance, encouragement and continuous support. They were always there to listen and to give advice when I needed, encouraging me to become an independent researcher and helped me to discover and grow the creativity and enthusiasm that I didn't know I had.

I would like to thank the distinguished members of my thesis jury Hitay Özbay, Melih Çakmakçı, M.Kemal Leblebicioğlu and Coşku Kasnakoğlu for approving my work and guiding me all the way up to this point.

Additionally, the members of our research group have contributed immensely to my personal and academic time at Bilkent. I am very thankful to İsmail Uyanık, Hasan Hamzaçebi, Ali Nail İnal for our wonderful times at Bilkent.

Finally, but forever I owe my loving thanks to my wife Pınar Necmiye Gülsoy Kerimoğlu for unconditional love. I also would like to thank my family Hanım Kerimoğlu, Sait Kerimoğlu, Serhat Kerimoğlu, Muzaffer Gülsoy, Sultan Esin Gülsoy, Sezen Gülsoy, Hilal Gülsoy for their support and encouragement.

Contents

List of Figures

List of Tables

Chapter 1

Introduction

1.1 Bipedal Walking Models and Platforms

Animals generate locomotion through the neuro-muscular coordination of their joints. Complete models of such systems would be excessively complex since they would need to take into account multiple layers of chemical, electrical, neural, muscular and mechanical processes, most of which are not fully understood with all of their details. Moreover, the complexity of such models would not be suitable for mathematical analysis and subsequent design of controllers for similarly structured robotic systems. In contrast, capturing locomotory behaviors using as simple models as possible, while keeping their basic characteristics could be sufficiently expressive, while also yielding a feasible basis for theoretical analysis. In the context of bipedal locomotion, passive dynamic walking has been proposed as a simple model of human walking [1, 2, 3]. In this context, mechanical principles underlying human walking were captured as the interaction of momentum and gravity in a simple and general fashion, with walking behaviors exhibited as asymptotically stable limit cycles of a very low degree of freedom model lacking any active components. In this work, we study the walking behaviour of the Passive Compass Gait (PCG) model and its possible extensions on different terrain model such as level, slope and rough terrains.

Even though passive dynamic walking models can be asymptotically stable even in the absence of any actuation or active control, the corresponding basins of attraction tend to be rather small and a downhill sloped ground is needed to replenish energy loss from toe collisions. In this respect, PCG models cannot walk over level, uphill and rough terrains. To improve stability and to eliminate the need for a sloped ground, a variety of active control methods have been proposed for this model in the literature based on different mechanisms for providing energy input to the system. Some of these methods are listed below.

- Impulsive energy injection following foot collision [4],

- Torque actuation on the hip or ankle joints [5, 6],

- Utilization of compliant legs with tunable properties [7].

For example, [5, 6] used passivity mimicking control with hip and ankle torque actuation to obtain slope invariant walking even on positive slopes. In [4], the authors used impulsive input along the support leg immediately before heel strike together with torque on the support leg to achieve energetically efficient walking. To achieve slope invariance and to increase the basin of attraction, [8] considered passivity-based control, using total energy shaping, increasing the robustness of the system to external disturbances and variations in ground slope.

Several studies on the compass gait also proposed methods of actuation through ankle mechanisms. For example, [9, 10] considered including an explicit model of the foot acting as a lever arm to provide thrust to the body through the leg. Impulsive input applied at toe-off immediately before heel strike was also studied separately by [11, 4]. In [7], the authors extended the PCG model with radial spring actuation on the stance leg, activated during mid-stance by instantaneously changing its stiffness. The authors in [12] considered parametric excitation using telescopic leg actuation with spring and damper to obtain walking on level ground. A simple dynamic walking model with feet and series elasticity at the ankle joint is developed in [13]. The authors in [13] show that the trailing leg push-off which starts before the collision of the leading leg, reduces

collision losses. In [14], the authors introduced a spring mechanism on the ankle joint of a PCG with foot in order to store part of the energy during the collision and to release it during the double stance phase passively. A three degree of freedom (DOF) spatial PCG model with under-actuated ankles and with only one actuator in the hip joint is considered in [15]. The authors in [15] obtained an open loop limit cycle and stabilized this limit cycle utilizing a discrete-time linear quadratic regulator (DLQR) method which was shown to have larger basin of attraction. In [16], the authors introduced a compass gait model with foot by including a constraint mechanism in the hip joint and rotary springs in the ankles which can walk with a minimal cost of transport. Symmetric and steady stable gaits of the PCG model, which gradually evolves through a regime of bifurcations and eventually exhibits an apparently chaotic gait is studied in [17]. In [18], the authors analyzed walker designs with and without knees, as well as with different foot structures to study bifurcation regimes of a passive walker model with knees.

In this respect, various passive and active dynamic walker prototypes have been described in the literature. The authors in [19] presented a three-dimensional dynamic walker platform, actuated by adding two active joints on the ankle to generate pitch and roll motions. The effects of ankle actuation on energy expenditure, disturbance rejection and the versatility of passive walking with the use of two mathematical models and one physical walker prototype is studied in [20]. An autonomous, three dimensional bipedal walking robot with efficient and human-like motions, consisting only of ankle actuation through a spring is presented in [21]. In [22], the authors developed energy-effective humanoid robots which utilize series elasticity at knee and ankle joints. In [23], the authors built a three-dimensional passive-dynamic walking robot with two legs and knees.

There are only a few bipedal robots that are capable of walking outside of highly controlled lab environments. This is due to the challenges arising from the stability, controllability and energy efficiency of walking on rough terrains. In this respect, the capabilities of an actuated PCG model on rough terrains using a control strategy combining a toe-off torque just prior to ground collision with a PD control loop on the desired inter-leg angle were investigated in [24]. The authors in [25] considered simulating a PCG model walking downhill on a

3

rough terrain in order to investigate the relation between stability of walking of the model with the increasing terrain roughness. It was shown in [25] that the passive walker model can tolerate only small amounts of roughness on the surface. The kinematics of compass walking are driven by the passive dynamics of the model to a large extent, however adaptation to rough terrain conditions and compensating for the perturbations require some form of active control. In [26], the authors presented a downhill walking, hip actuated compass gait walker by applying trajectory-based policy gradient algorithm where walking on rough surface slopes up to 0.15 radians was achieved. In [27], the authors study the robustness of a bipedal model on unknown terrains. For a desired walking pattern, the authors define an error signal for the model, quantify the robustness by the $L2$ gain of the closed-loop system and optimize that $L2$ gain via a robust controller. It was shown in [27] that their controller can increase the capability of the model for traversing unknown terrains.

Several studies in the literature proposed methods of actuation through an ankle mechanism on uneven terrains. For example, [24] extended the PCG model with a torque input at the hip joint and an impulsive toe push-off applied prior to ground collision. The authors in [24] conclude that their model, relying on passive dynamic principles, is capable of walking on significantly rough terrains. In [28], an open loop controller for an ankle and hip actuated compass gait biped is designed for walking over rough terrain. The results in [28] state that the biped robot can achieve walking on rough terrains. In [29], the authors introduced a compass gait model with feet actuated via hip and ankle torques. The authors conclude that the bio-inspired controller implemented on the model can generate stable walking patterns on various range of downhill and uphill slopes. The authors in [30] studied compass biped model with underactuated ankle walking on slight uphill and downhill slopes where the model incorporates a constraint mechanism at hip in order to lock the hip angle as the swing leg retracts to a desired angle. The studies focusing on ankle actuation of compass gait model over sloped and rough terrain mostly utilize hip joint along with ankle joint. In our study, however, we only introduce series-elastic ankle actuation which is related with our long term goal of developing active ankle foot orthosis systems

where we consider ankle spring precompression and ground slope as the primary parameters of interest.

1.2 Orthosis and Prosthesis Platforms

In this thesis, we propose to use a series-elastic actuation structure on the compass gait model to provide thrust during the push-off phase of walking. Our motivation for studying the effects of an actuated ankle comes from our longer term goal of implementing actuated ankles for powered lower-extremity robotic orthoses. Such orthoses seek to eliminate ambulatory limitations of individuals who have lost function in their lower extremities, providing increased mobility. Existing research in this direction, however, almost exclusively focuses on restoring knee and hip joint functionality. The actuated ankle joint, despite its key role for the energetics and stability of human walking, is only considered for exoskeletons designed for power augmentation. Consequently, the lack of actuated ankle joints in robotic orthoses limits their energetic efficiency and results in unnatural walking patterns, possibly impairing their utility and adoption. In light of these observations, our study seeks to understand the impact of series-elastic actuation (SEA) for an Ankle Foot Orthosis (AFO) on walking dynamics, towards eventual integration with a powered robotic lower-body orthosis. In this respect, an active AFO prototype is developed with the objective of utilizing passive energy storage components in conjunction with actuators in the ankle joint, employing natural dynamics of walking.

Series elastic actuation, wherein a position controlled actuator is used in series with a passive spring, has been used by the robotics community to achieve efficient and high bandwidth force control [31]. Such mechanisms received particular attention in the legged locomotion community, motivated by similarly compliant mechanisms adopted by muscles and tendons as well as the success of compliant models as accurate representations of locomotory tasks. SEA controls orthotic joint stiffness and damping for plantar and dorsiflexion ankle rotations and they are primarily used for portable, complementary assistive AFO actuation. The

5

study explained in [32, 33] introduces a portable wearable device for the ankle-impaired individuals that can be used in specific gait tasks such as walking in unstructured environments, modulating speed, climbing stairs, etc. And rather than using just active elements, the peak power required by the motor during push off can be decreased by using both active and passive elements. In [34], the authors used a force controllable SEA to control the impedance of the orthotic ankle joint throughout the walking cycle to treat the drop-foot gait disorder. In [35], the authors developed an active ankle foot prosthesis (AAFP) which utilizes SEA to prevent the need for a large and heavy impedance-controlled motor. Using both series and parallel elasticity, [36] developed an AAFP that fulfills the demanding human-like ankle specifications and decreases the metabolic cost of amputee locomotion compared to a conventional passive-elastic prostheses.

1.3 Contributions of the Thesis

The novel contributions of this thesis can be summarized as follows. Firstly, we model the action of a series-elastic actuation mechanism on the PCG model by adding a radial spring at the ankle, obtaining stable walking on level ground for large ranges of model parameters. Seeking to model the function of human ankle, the proposed model is simpler than alternatives in the literature, with only a linear spring and point foot to provide thrust during a non-instantaneous toe push-off phase. The spring is assumed to be compressed slowly during the stance phase and released immediately after heel strike. Then, we thoroughly explore and investigate the effects of ankle spring parameters on walking by deriving the hybrid dynamics of the model, finding and characterizing the stability of fixed points and performing parameter dependent stability analysis via Poincaré methods for level ground walking. In a real platform, since the SEA would be used to adjust the precompression of the spring, we focus our analysis on the dependence of stability on this spring precompression parameter. As we increase the amount of precompression, we inject more energy into the model and observe stable, period doubling bifurcations, chaotic and eventually unstable gaits. This study on energy injection into the model assumes the precompression

6

to be chosen in an open-loop manner, and hence does not yield stable gaits for all velocities. To address this issue, we propose an active feedback controller on the spring precompression which can stabilize gaits that were previously period 2^n ($n = 1, 2, 4, 8, ...,$), chaotic and unstable gaits, reducing them to regular, period-one walking gaits. The proposed controller uses forward velocity feedback to perform once-per-step adjustments on the spring precompression. Computing the eigenvalues of the return map Jacobian, we show that the controller not only improves the stability of the walking model across a large range of precompression values, but also provides a control policy to achieve, robust walking for desired speed and step length values from a large range.

Second, we extend the capabilities of the ankle compass biped model to walk on a large range of downhill and uphill ground slopes and eventually on rough terrain. The model can walk in a stable manner on downhill and uphill slopes up to -3.9^o to $+4.45^o$, respectively. We, then obtain a map of stable walking regions with different periodicities as a function of spring precompression and ground slope. Moreover, we also find eigenvalues as well as gait velocities for all period-1 stable regions. These maps are utilized in order to implement a ground slope feedback controller on the ankle spring that can achieve stable walking on rough terrain. We, then characterize locomotion performance over terrains with gradually increasing roughness profiles. We observe that the ground slope feedback controller performs better over the less rough terrains. Furthermore, the locomotion performance is enhanced by applying stance leg velocity feedback along with the ground slope feedback.

Finally, our results provide a step in understanding parametric design and stability trade-offs in achieving dynamic walking with series-elastic actuation on the ankle. Towards an implementation of the principles developed in this thesis, an experimental instantiation of an active AFO system was also developed. We have also been able to integrate this active AFO with an active knee orthosis system. Our initial observations on able bodied individuals have shown that the assistive torque generated by the SEA propels the body forward while decreasing energy loss due to ground collision.

This thesis is organized as follows. In Chapter 2, we introduce the serially-actuated compass gait model, describing its underlying assumptions and the resulting equations of motion. In Chapter 3, we use Poincaré methods to identify limit cycles of the model for a specific choice of model parameters, and subsequently perform parameter dependent stability analysis leading to our investigation of bifurcation regimes of the model. Then, we propose the stance leg apex velocity feedback control on the spring precompression to stabilize otherwise unstable limit cycles. Chapter 4 continues with spring precompression and ground slope dependent stability analysis leading to useful versions of spring precompression versus ground slope map. Chapter 5 introduces walking on rough terrains via the ground slope based feedback control on the spring precompression. Then, the performance enhancement of rough terrain walking via the ground slope feedback along with stance leg velocity feedback on ankle spring in presented. In, Chapter 6 we introduce active AFO platform and present the experimental results. Then, we demonstrate the integration of the active AFO and active knee orthosis systems and consequently present experimental results showing that the integrated system can generate efficient walking patterns. We conclude the thesis in Chapter 7.

Chapter 2

The Ankle Actuated Compass Gait Model (AACG)

In this chapter, we first review the equations of motion and modeling assumptions for the Passive Compass-Gait (PCG) model. We then propose a series elastic ankle actuation method for the PCG model, resulting in the definition of our Ankle-Actuated Compass Gait (AACG) Model. This is followed by the derivation of the hybrid dynamical equations of motion for the new model. Subsequently, we illustrate representative locomotion trajectories for this system over level ground.

2.1   The Passive Compass Gait Model

The passive compass gait model is one of the simplest models of bipedal locomotion, consisting of two rigid legs without knee or foot components, connected by a frictionless hinge at the hip joint as illustrated in Fig. 2.1.

The motion of the PCG model is restricted to two dimensional sagittal plane. A point mass M is situated at the body, which coincides with the hip joint connecting two identical rigid legs of length l. Each leg also has a point mass m
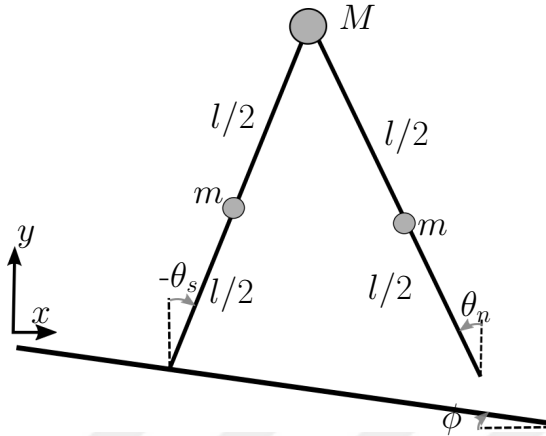
Figure 2.1: The passive compass gait model.

centered on the leg. The system has no actuation, and hence must walk down a ground with slope ϕ. The motion of the PCG model is constrained in the sagittal plane and consists of the following stages:

- Swing: During this stage, the hip joint pivots around the point of support on the ground of its support leg. The other leg, called the nonsupport leg or the swing leg swings forward.

- Collision Event: This occurs instantaneously when the swing leg touches the ground and the previous support leg leaves the ground.

During walking, the impact of the swing leg with the ground is assumed to be slipless plastic. This implies that during the instantaneous transition stage:

- The model configuration remains unchanged,

- The angular momentum of the model about the impacting foot as well as the angular momentum of the pre-impact support leg about the hip are conserved. These conservation laws lead to a discontinuous change in the mass velocities.

Similar to other planar biped models lacking knee joints, the swing leg is

assumed to be sufficiently retracted to clear the ground, returning to its original length prior to the ground collision.

During the swing phase, the model configuration can be described by $\boldsymbol{\theta} := [\theta_n, \theta_s]^T$, where θ_n and θ_s are the angles of non-stance and stance leg with the vertical (counterclockwise positive), respectively (see Fig. 2.1). The state vector $\boldsymbol{q}$ associated with the PCG model is then defined as

$$\boldsymbol{q} := [\boldsymbol{\theta}, \dot{\boldsymbol{\theta}}]^T = [\theta_n, \theta_s, \dot{\theta}_n, \dot{\theta}_s]^T. \tag{2.1}$$

The governing equations for the PCG model consist of nonlinear differential equations for the swing stage, together with algebraic equations for the collision. Since the model is well studied in the literature, we only give the equations of motion of PCG model as follows. For exact derivations, the reader is referred to [6]. During the swing phase, system trajectories satisfy

$$\boldsymbol{M}(\boldsymbol{\theta})\ddot{\boldsymbol{\theta}} + \boldsymbol{B}(\boldsymbol{\theta}, \dot{\boldsymbol{\theta}})\dot{\boldsymbol{\theta}} + \boldsymbol{G}(\boldsymbol{\theta}) = \boldsymbol{0}, \tag{2.2}$$

where $\boldsymbol{M}(\boldsymbol{\theta})$ is the 2×2 inertia matrix given derived as

$$\boldsymbol{M}(\boldsymbol{\theta}) := \begin{bmatrix} (l^2 m)/4 & -(1/2)l^2 m \cos{(\theta_s - \theta_n)} \\ -(1/2)l^2 m \cos{(\theta_s - \theta_n)} & (1/4)l^2(5m + 4M) \end{bmatrix}, \tag{2.3}$$

$\boldsymbol{B}(\boldsymbol{\theta}, \dot{\boldsymbol{\theta}})$ is the 2×2 centrifugal coefficient matrix derived as

$$\boldsymbol{B}(\boldsymbol{\theta}, \dot{\boldsymbol{\theta}}) := \begin{bmatrix} 0 & (1/2)l^2 m \dot{\theta}_s \sin{(\theta_s - \theta_n)} \\ -(1/2)l^2 m \dot{\theta}_{ns} \sin{(\theta_s - \theta_n)} & 0 \end{bmatrix}, \tag{2.4}$$

and $\boldsymbol{G}(\boldsymbol{\theta})$ is the 2×1 vector of gravitational torque components derived as

$$\boldsymbol{G}(\boldsymbol{\theta}) := \begin{bmatrix} (1/2)lmg\sin{(\theta_n)} \\ -(M1 + (3/2)lm)g\sin{(\theta_s)} \end{bmatrix}. \tag{2.5}$$

During the instantaneous collision, the swing leg touches the ground and the support leg leaves the ground. For an inelastic, non-sliding collision of the foot with the ground, the angular momentum of the model is conserved during the

11

collision. This allows us to linearly relate the post-impact and the pre-impact angular velocities of the model with

$$\dot{\boldsymbol{\theta}}(\boldsymbol{T})^+ = \boldsymbol{H}(\boldsymbol{\theta}(\boldsymbol{T}))\dot{\boldsymbol{\theta}}(\boldsymbol{T})^-, \tag{2.6}$$

where $\dot{\boldsymbol{\theta}}(\boldsymbol{T})^-$ and $\dot{\boldsymbol{\theta}}(\boldsymbol{T})^+$ are the angular velocities just before and after the transition that takes place at time $t = T$ and $\boldsymbol{H}(\boldsymbol{\theta}(\boldsymbol{T}))$ is given as

$$\boldsymbol{H}(\boldsymbol{\theta}(\boldsymbol{T})) := \begin{bmatrix} \frac{m-4(m+M)\cos(2(\theta_s-\theta_n))}{2\cos(2(\theta_s-\theta_n)m-3m-4M} & \frac{2m\cos(\theta_s-\theta_n)}{2\cos(2(\theta_s-\theta_{ns}))m-3m-4M} \\ -\frac{2(m+2M)\cos(\theta_s-\theta_n)}{2\cos(2(\theta_s-\theta_n))m-3m-4M} & \frac{m}{2\cos(2(\theta_s-\theta_n))m-3m-4M} \end{bmatrix}. \tag{2.7}$$

Once the transition event occurs, stance and swing legs are renamed and the system proceeds with the same swing dynamics as the previous stride.

2.2 Modelling Assumptions for the AACG Model

During normal human walking, the ankle torque is transmitted to the leg through the lever arm of the foot and the resulting force on the body depends on the internal dynamics of the leg. Nevertheless, a sufficiently accurate model can still be obtained if the masses of both the leg and the toe, together with ankle kinematics are assumed to be negligible, allowing a direct model of the ankle torque as a radial force on the leg as shown in Fig. 2.2. Based on this observation, our model will represent the foot as a point contact, and the action of ankle joint as a linear force component acting along the leg. The resulting serially-actuated active prismatic joint will then be used to compensate for energy losses due to ground collisions during toe push-off.

This assumption leads to our simplified model, which we call the Ankle-Actuated Compass Gait (AACG) model, shown in Fig. 2.3. It consists of a point mass M modeling the torso, to which two legs of length l with small mid-length masses m are attached. For the stance leg, we assume that a linear ankle spring with stiffness k and rest length r_o is available and can be engaged before the leg
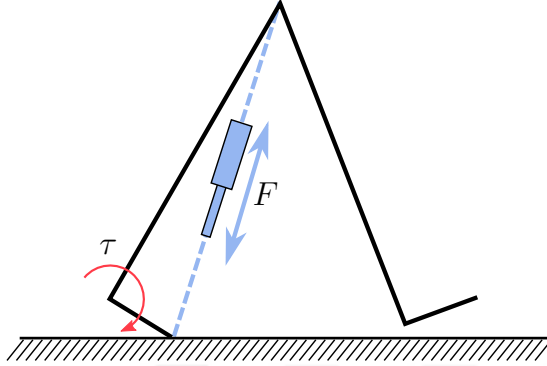
Figure 2.2: Modeling of the action of ankle torque τ as a radial force F on the body.

lifts off. The length of the spring, r is constrained with $r > 0$, capturing the unidirectional nature of heel contact with the ground. The remaining configuration variables θ_s and θ_n represent the angles of the supporting and non-supporting leg angles relative to the vertical, respectively and p_{toe} denotes the position of the non-stance toe. The AACG model is constrained to planar walking with sloped ground and the angle for ground slope is denoted by ϕ whose negative and positive values respectively correspond to downhill and uphill slopes as shown in see Fig. 2.3.
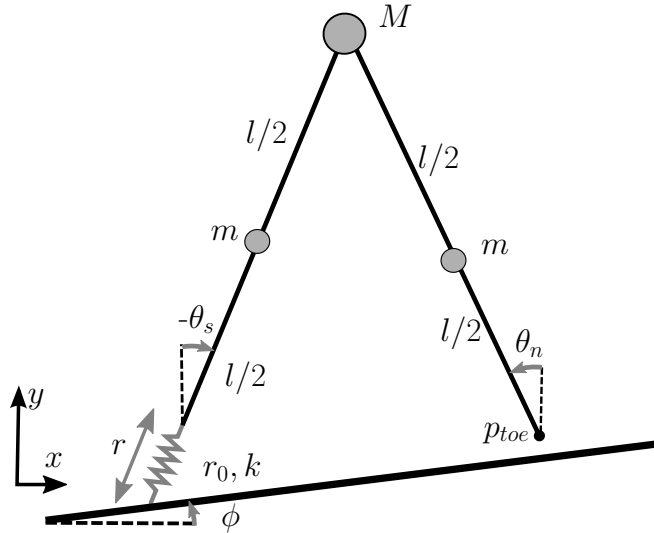
Figure 2.3: The Ankle-Actuated Compass Gait Model.

For normal, steady-state walking, the AACG model is assumed to go through two phases, single support and double support, separated by an infinitesimal

13

"collision event" to capture the effects of weight transfer from one foot to the other as shown in Fig. 2.4. During the single support phase, the AACG model exhibits the dynamics of a double pendulum similar to the standard PCG model. The *supporting leg* is in contact with the ground and the other leg is free to swing, with the stance leg spring assumed to be locked with $r = 0$, capturing the effect of human heel contact with the ground. Similar to the standard PCG model, we ignore foot scuffing collisions occurring at the instance when swing leg passes the stance leg. The single support phase ends when the swing leg comes into contact with the ground ahead of the stance leg.

Since the collision with the ground is slip-free and inelastic, it preserves configurations, but results in a discrete change in velocities due to impulsive collision forces. Following the collision, the standard PCG model performs an immediate weight transfer and resumes with the subsequent single support phase. The AACG model, however, follows the collision with a non-instantaneous double support phase, wherein both legs remain on the ground and a "precompressed" ankle spring in series with the trailing stance leg is released. This results in a forward thrust supported by the fixed trailing toe, with the front leg pivoting freely around its newly acquired toe contact. The ankle spring continues to extend until it reaches its rest length (which we also refer to as the spring precompression), at which point the trailing stance leg lifts off and the spring is brought back to $r = 0$ in preparation for the next toe push-off. The system then continues on to the next single support phase. Fig. 2.4 depicts the two phases of the model as well as the collision event. The following sections present models associated with each phase.

2.3   Dynamics of The Single Support Phase

The single support phase for the AACG model has the same structure as the PCG model, with identical equations of motion. We parameterize the two dimensional configuration space in this phase with the angles of the support and non-support
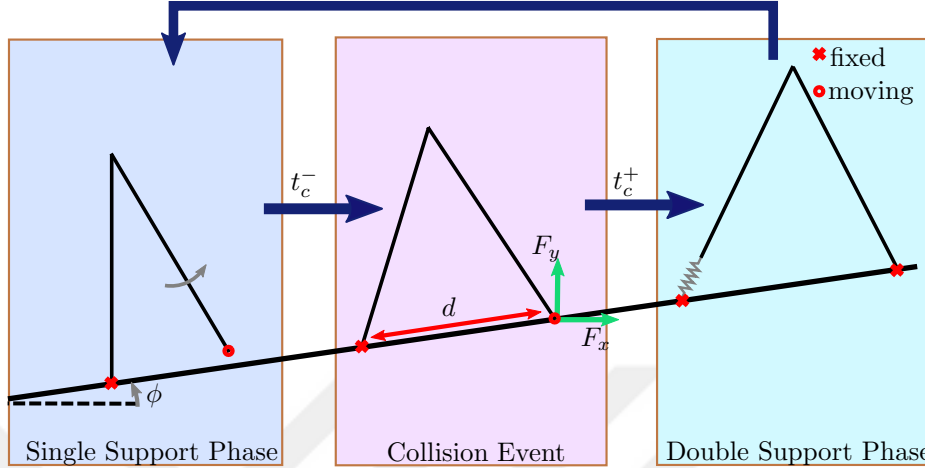
Figure 2.4: Hybrid phases of walking with the Ankle-Actuated Compass Gait Model. The collision event is instantaneous and is modeled with a discontinuous change in system velocities.

legs to yield the definition

$$\boldsymbol{q}_{ss} := [\theta_s, \theta_n]^T \, , \tag{2.8}$$

where $\boldsymbol{q}_{ss}$ is the configuration vector for single support phase. Detailed derivations for the dynamics during the single support phase have been extensively covered in the literature and have been presented in Section 2.1.

2.4 The Collision Map

When the swing leg collides with the ground, the AACG model experiences impulsive forces, resulting in an instantaneous change in system velocities, while the model configuration remains unchanged. However, unlike the standard PCG model, both legs remain fixed on the ground for the AACG model and the angular momentum of the system is no longer conserved around either toe. Consequently, we fall back to Lagrangian methods with impulsive forces, similar to the methods used in [37], to derive the post-collision velocities. This method uses the unconstrained, three degree of freedom (DOF) AACG model with a released spring shown in Fig. 2.3 and identifies impulsive constraint forces on the swing toe that would bring its velocity to zero.

The three dimensional configuration space of the system during this instantaneous collision phase can be defined as

$$\boldsymbol{q}_c := [\theta_s, \theta_n, r]^T. \tag{2.9}$$

Impulsive forces experienced by the swing leg during the collision event are illustrated in the middle diagram in Fig. 2.4. Writing the system kinetic and potential energy expressions as a function of $\boldsymbol{q}_c$, we first obtain the Lagrangian, which is then used to derive the equations of motion

$$\mathbf{M}_c(\mathbf{q}_c)\ddot{\mathbf{q}}_c + \mathbf{B}_c(\mathbf{q}_c, \dot{\mathbf{q}}_c)\dot{\mathbf{q}}_c + \mathbf{G}_c(\mathbf{q}_c) = \mathbf{J}_c^T(\mathbf{q}_c)\mathbf{F}_I\delta(t - t_c) \ , \tag{2.10}$$

that remain valid only instantaneously with $t \in [t_c^-, t_c^+]$. Here, the Dirac delta function $\delta(t - t_c)$ is used to represent the impulsive forces acting on the swing toe at $t = t_c$, where t_c is the instance of collision. The left side of the equation captures the continuous dynamics of the three DOF model, detailed derivations are given in Appendix A.

$\mathbf{M}_c(\mathbf{q}_c)$ is the 3×3 mass matrix, $\mathbf{B}_c(\mathbf{q}_c, \dot{\mathbf{q}}_c)$ is the 3×3 matrix which represents Coriolis forces and $\mathbf{G}_c(\mathbf{q}_c)$ is the 3×1 vector which captures gravitational forces. The transposed Jacobian $\mathbf{J}_c^T(\mathbf{q}_c)$ is a 3×2 matrix which maps velocities from swing toe coordinates to generalized coordinates and $\mathbf{F}_I := [F_x, F_y]^T$ is a 2×1 vector which represents external impulsive forces along x and y axes acting on the system during collision.

Solving for system accelerations, we have

$$\ddot{\mathbf{q}}_c = \mathbf{M}_c(\mathbf{q}_c)^{-1}\big(\mathbf{J}_c^T(\mathbf{q}_c)\mathbf{F}_I\delta(t - t_c) - \mathbf{B}_c(\mathbf{q}_c, \dot{\mathbf{q}}_c)\dot{\mathbf{q}}_c - \mathbf{G}_c(\mathbf{q}_c)\big) \ , \tag{2.11}$$

where $\mathbf{M}_c(\mathbf{q}_c)$ is assumed to be invertible.

Model velocities before and after the collision are related through the integral of these dynamics, yielding

$$\int_{t_c^-}^{t_c^+} \ddot{\mathbf{q}}_c dt = \int_{t_c^-}^{t_c^+} \mathbf{M}_c(\mathbf{q}_c)^{-1}\big(\mathbf{J}_c^T(\mathbf{q}_c)\mathbf{F}_I\delta(t - t_c) - \mathbf{B}_c(\mathbf{q}_c, \dot{\mathbf{q}}_c)\dot{\mathbf{q}}_c - \mathbf{G}_c(\mathbf{q}_c)\big)dt \ , \tag{2.12}$$

where t_c^- and t_c^+ represent time instants just before and after collision, respectively. Since $\mathbf{q}_c$ is differentiable and $\dot{\mathbf{q}}_c$ is continuous, the non-impulsive terms

16

$\mathbf{B}_c(\mathbf{q}_c, \dot{\mathbf{q}}_c)\dot{\mathbf{q}}_c$ and $\mathbf{G}_c(\mathbf{q}_c)$ vanish in the infinitesimal integration which takes place from time t_c^- to t_c^+. Since configurations remain continuous, the integral on the left hand side also reduces to the difference in configuration velocities. Hence, the result of the integration is equal to the post collision velocities and the effects of the non-instantaneous variables are cancelled yielding the following simplified collision map

$$\dot{\mathbf{q}}_c\left(t_c^+\right) - \dot{\mathbf{q}}_c\left(t_c^-\right) = \mathbf{M}_c(\mathbf{q}_c(t_c))^{-1}\mathbf{J}_c^T(\mathbf{q}_c(t_c))\mathbf{F}_I \; , \tag{2.13}$$

where $\dot{\mathbf{q}}_c(t_c^-)$ and $\dot{\mathbf{q}}_c(t_c^+)$ denote system velocities just before and after the collision, respectively. For simplicity, we define $\dot{\mathbf{q}}_c(t_c^-)$ as $\dot{\mathbf{q}}_c^-$ and $\dot{\mathbf{q}}_c(t_c^+)$ as $\dot{\mathbf{q}}_c^+$ from now on. In order to find this unknown collision force, we impose the constraint that the swing toe must come to rest following the plastic collision. Forward kinematics yields the swing toe velocities as a function of the generalized coordinates as

$$\begin{bmatrix} \dot{x}_{toe} \\ \dot{y}_{toe} \end{bmatrix} = \begin{bmatrix} r\cos\theta_s & -l\cos\theta_n & \sin\theta_s \\ -r\sin\theta_s & l\sin\theta_n & \cos\theta_s \end{bmatrix} \begin{bmatrix} \dot{\theta}_s \\ \dot{\theta}_n \\ \dot{r} \end{bmatrix} = \mathbf{J}_c(\mathbf{q}_c)\dot{\mathbf{q}}_c \; . \tag{2.14}$$

The plastic collision requires that post-collision toe velocities become zero, which can be expressed with the constraint

$$\mathbf{J}_c(\mathbf{q}_c)\dot{\mathbf{q}}_c^+ = \mathbf{0} \; . \tag{2.15}$$

Combining (2.13) and (2.15), we have

$$\mathbf{J}_c(\mathbf{q}_c)\left(\dot{\mathbf{q}}_c^- + \mathbf{M}_c(\mathbf{q}_c)^{-1}\mathbf{J}_c^T(\mathbf{q}_c)\mathbf{F}_I\right) = \mathbf{0} \; , \tag{2.16}$$

which can be solved for $\mathbf{F}_I$, which yields the final solution for post-collision configuration velocities as

$$\dot{\mathbf{q}}_c^+ = \left(\mathbf{I} - \mathbf{M}_c(\mathbf{q}_c)^{-1}\mathbf{J}_c^T(\mathbf{q}_c)\left(\mathbf{J}_c(\mathbf{q}_c)\mathbf{M}_c(\mathbf{q}_c)^{-1}\mathbf{J}_c^T(\mathbf{q}_c)\right)^{-1}\mathbf{J}_c(\mathbf{q}_c)\right)\dot{\mathbf{q}}_c^- = \mathbf{H}_c(\mathbf{q}_c^-)\dot{\mathbf{q}}_c^- \; . \tag{2.17}$$

Here, we assume that $\mathbf{J}_c(\mathbf{q}_c)\mathbf{M}_c(\mathbf{q}_c)^{-1}\mathbf{J}_c^T(\mathbf{q}_c)$ is invertible. We note that $\mathbf{M}_c(\mathbf{q}_c)$ is a symmetric positive definite matrix which is assumed to be invertible. Hence, we have $rank(\mathbf{J}_c(\mathbf{q}_c)\mathbf{M}_c(\mathbf{q}_c)^{-1}\mathbf{J}_c^T(\mathbf{q}_c)) = rank(\mathbf{J}_c(\mathbf{q}_c))$. From (2.14), it easily follows

that when $\theta_s - \theta_n \neq \pi/2$ or $r \neq 0$, we have $rank(\mathbf{J}_c(\mathbf{q}_c)) = 2$, which implies that $\mathbf{J}_c(\mathbf{q}_c)\mathbf{M}_c(\mathbf{q}_c)^{-1}\mathbf{J}_c^T(\mathbf{q}_c)$ is invertible. Since these conditions always hold in our system, it follows that $\mathbf{J}_c(\mathbf{q}_c)\mathbf{M}_c(\mathbf{q}_c)^{-1}\mathbf{J}_c^T(\mathbf{q}_c)$ is also always invertible.

Detailed expressions for general form of $\mathbf{H}_c$, which is a 3×3 matrix capturing a general collision map with arbitrary initial states for the ankle spring, are given in Appendix A. In this paper, we focus on the AACG model with the ankle spring activated right before the collision, meaning that we have $r^- = 0$ and $\dot{r}^- = 0$. This simplifies the collision map to

$$\dot{r}^+ = \frac{2ml\sin(\theta_s^- - \theta_n^-)\dot{\theta}_n^- - (3m + 4M)\sin(2(\theta_s^- - \theta_n^-))\dot{\theta}_s^-}{7m + 8M + 3\cos(2(\theta_s^- - \theta_n^-))} , \tag{2.18}$$

which is the form we use for all our simulations. Note that we only need to compute $\dot{r}^+$ since the system has only a single degree of freedom, the spring length, during double stance.

2.5   Dynamics of the Double Support Phase

During the double support phase, both legs maintain contact with the ground and the ankle spring for the trailing leg spring is activated, resulting in a model with only the single, prismatic ankle DOF, r. The remaining joint variables are constrained by the closed kinematic chain of the legs as shown in Fig. 2.3. The single dimensional configuration space associated with the double support phase is hence defined as

$$\mathbf{q}_{ds} := r .$$

The leg angles, θ_s and θ_n, are kinematically related to the ankle extension with

$$\theta_s = -\pi/2 + \arccos(\frac{d^2 - l^2 + (l + r)^2}{2d(l + r)}) + \phi,$$

$$\theta_n = \pi/2 - \arccos(\frac{d^2 + l^2 - (l + r)^2}{2dl}) + \phi,$$

where ϕ is the ground slope and d is the distance between the toes that is fixed at the moment of collision and is given as,

$$d = 2l\cos(\pi/2 - \theta_n + \phi). \tag{2.19}$$

The dynamics of this phase is given in appendix in detail. This phase continues until the ankle spring becomes fully extended, having transferred all of its potential energy into the system. At that point, the double support phase ends and the spring length is brought back to its precompressed state with $r = 0$ in preparation for the next collision. The prismatic joint is then locked, and the trailing stance leg ceases contact with the ground. The model then transitions into the next single stance phase as shown in Fig. 2.4. Prior to this transition, stance and swing legs are renamed, using the same single stance dynamics as the previous stride. All of our results in subsequent sections are based on numerical integration of these dynamics through one or more strides.

2.6   System Trajectories

Having derived all of the components necessary to obtain the trajectories of the hybrid dynamics for the AACG system, we used Matlab to numerically integrate its equations of motion. The main reasons for demonstrating these simulation results are the following. First, we want to show the possibility of obtaining a stable periodic walking gait on level ground, which is not possible in PCG model. We also want to show the effect of impact collision where the continuous phase variables (θ_s, θ_n) do not change, but a discontinuity occurs on system velocities $(\dot{\theta}_s, \dot{\theta}_n)$. Our simulations in this thesis use $M = 1kg$, $m = 0.01kg$ and $l = 1m$ to illustrate the behavior of the AACG model. Fig. 2.5 shows an example trajectory for the AACG model with spring stiffness $k = 500N/m$ and spring rest length $r_0 = 0.014m$, starting from an initial condition within the single stance with $\theta_s = 0$, $\dot{\theta}_s = -0.364$, $\theta_n = -0.011$, $\dot{\theta}_n = 1.328$ for level ground $\phi = 0$. For this example, model trajectories converge to a limit cycle, sustaining stable locomotion across level ground.

Fig. 2.6 shows the length of the ankle spring during the double support phase for the same simulation. As shown by the top plot, the spring starts extension after collision, injecting its potential energy into the system until it reaches its rest length of $r_0 = 0.014m$. The derivations and results given here are presented

19
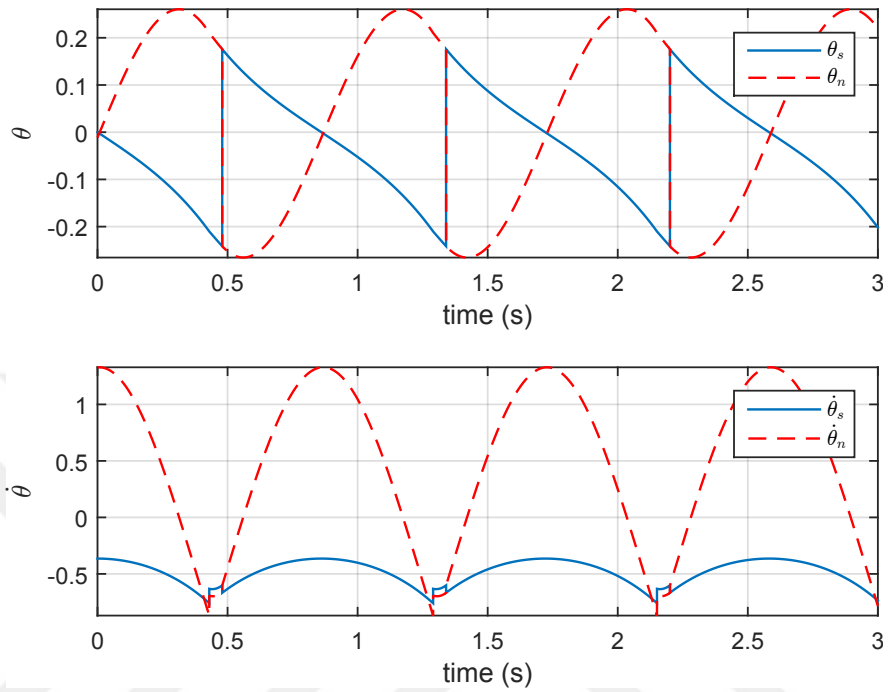
Figure 2.5: Example trajectories for the Ankle Actuated Compass Gait model with $M = 1kg$, $m = 0.01kg$, $l = 1m$, $k = 500N/m$ and $r_0 = 0.014m$. Trajectories of both the stance leg (blue) and the swing leg (red) are shown.

in [38].
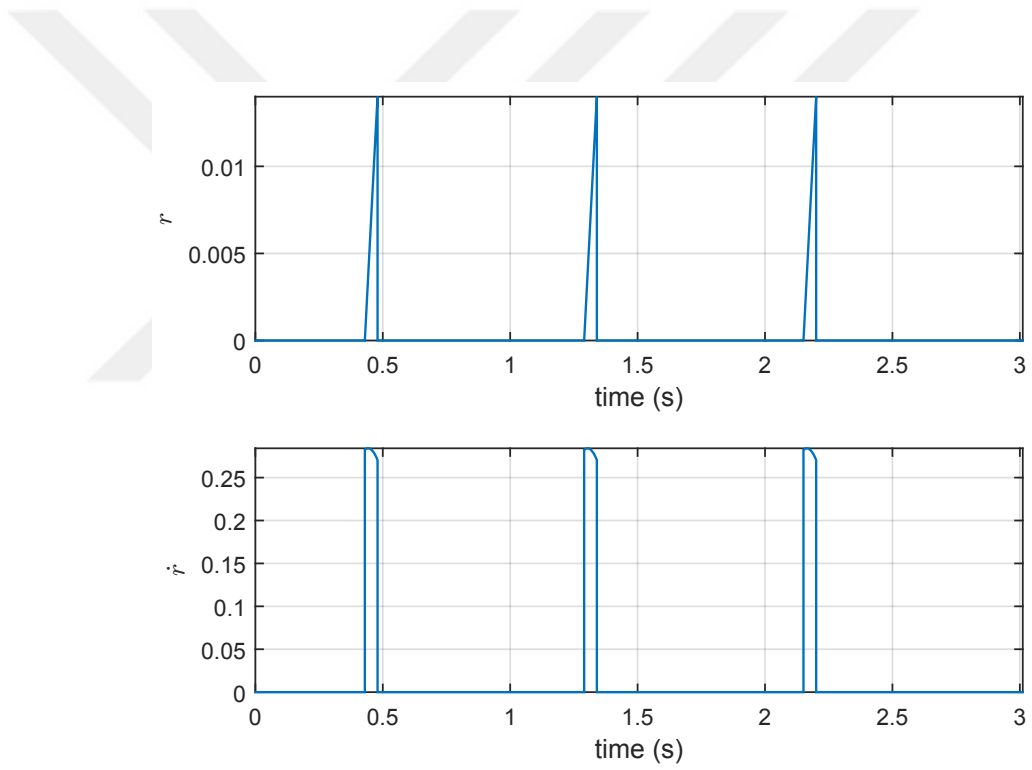
Figure 2.6: Ankle spring length (top) and extension speed (bottom) for the AACG model. The spring is only active during the double support phase.

Chapter 3

Stability and Control of Walking with the AACG Model over the Level Ground

In this chapter, our aim is to perform stability analysis on our proposed model by applying Poincaré methods. Then, we investigate the stability of the model with respect to various system parameters. Finally, we extend the stability of the model by applying a feedback control on the ankle spring.

3.1 Periodic Walking Gaits and Apex Return Map

We begin our analysis of AACG walking behaviors by identifying periodic walking gaits, which corresponds to limit cycles of AACG model, when all system parameters, including the precompressed spring length, are fixed. For simplicity, let us define the initial swing and support as Leg A and Leg B, respectively. To demonstrate the existence of a limit cycle corresponding to a periodic walking gait, indicating different phases of walking behaviour, we illustrate a simulation

result as given in Fig. 3.1 where trajectories for only one leg (leg A) are shown. At the point marked with 1, the swing leg (leg B) collides with the ground, resulting in a discontinuous change in velocities. Subsequently, the ankle spring in leg A decompresses until point 2, which is when the ankle spring in leg A lifts off after injecting all of its stored energy into the model and reaches its rest length. Leg A then becomes the new swing leg. Points marked with 3 and 4 correspond to the collision of leg A with the ground, and the liftoff event for leg B completing the limit cycle.
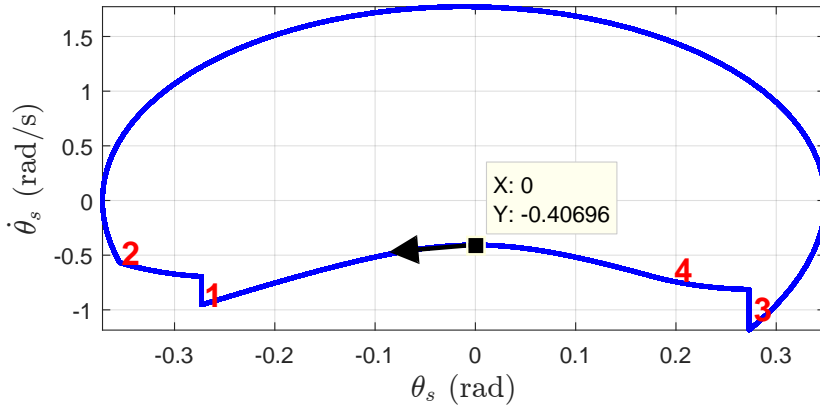

Figure 3.1: Phase space trajectories for an example periodic gait generated by the AACG model with $M = 1$ kg, $m = 0.01$ kg, $l = 1$ m, $k = 100$ N/m, $r_0 = 0.05$ m. Only the states for one of the legs (leg A) are plotted, going through the stance phase at the bottom half and the swing phase at the top half. One cycle in the figure corresponds to two steps of the model. Events marked with 1,2,3 and 4 correspond to the beginning of toe push-off for leg A, leg A liftoff, ground collision for leg B and the end of the toe push-off for leg B, respectively.

A commonly used method for the identification and characterization of limit cycles in locomotory systems is Poincaré analysis, which relies on defining a co-dimension one subset of the state space, called the Poincaré section, which transversally intersects all system trajectories. Successive intersections of system trajectories with this subset generate a discrete sequence, formally defined through the Poincaré map (also called return map) that takes one intersection to the next. Fixed points of this map (and their stability) correspond to the presence (and stability) of limit cycles in the original system.

For the AACG model, we choose the Poincaré section as the vertical, forward

moving configurations of the supporting leg with $\theta_s = 0$ and $\dot{\theta}_n > 0$. This configuration corresponds to the highest point of the torso trajectory during the single support phase, which we call the *apex point*. As an example, the limit cycle illustrated in Fig. 3.1 repeatedly intersects this section at $\theta_s = 0$ rad, $\dot{\theta}_s = -0.4069$ rad/s, $\theta_n = -0.0596$ rad, $\dot{\theta}_n = 1.7568$ rad/s, corresponding to a fixed point of the Poincaré map.

In addition to help identify limit cycles, the return map also allows the characterization of their stability properties through its linearization around fixed points. Eigenvalues of the resulting Jacobian can be used to characterize local stability properties for the limit cycles, with local asymptotic stability corresponding to all eigenvalues of the Jacobian falling within the unit circle.

Note that for a valid Poincaré analysis, the trajectories should cross the Poincaré section transversally. The trajectories which do not satisfy this requirement will result in an invalid Poincaré analysis. For this reason, in order to ensure the validity of the Poincaré map, we check a number of fault conditions during our simulations. In particular, we discard and disregard trajectories that

- Locomote backwards with $\dot{\theta}_s \geq 0$,

- Do not admit full extension of the ankle spring, with $d \leq r_0$,

- Require the heel to go underground with $\dot{r}^+ < 0$,

- Result in fault conditions such as the torso mass M going underground, angle between the legs becoming unreasonably large or spring thrust being insufficient to ensure liftoff.

Elimination of such problematic cases ensures that all remaining trajectories of the AACG model pass transversally through the Poincaré section at the apex point. More formally, let $x := [\dot{\theta}_s, \theta_n, \dot{\theta}_n]^T$ denote the state vector within the Poincaré section. Given Poincaré states x_i and x_{i+1} for the ith and $i+1^{th}$ apex points, respectively, the AACG return map, $G : \mathbb{R} \times \mathrm{S}^1 \times \mathbb{R} \to \mathbb{R} \times \mathrm{S}^1 \times \mathbb{R}$, is

defined as

$$\mathbf{x}_{i+1} = \mathbf{G}(\mathbf{x}_i) \ . \tag{3.1}$$

Note that the map $\mathbf{G}$ given by (3.1), in theory, can be found by solving the dynamic equations of motion for AACG model given by (2.2). However, due to the highly non-linear nature of these equations, finding an analytical expression of $\mathbf{G}$ is extremely difficult and even may not be possible. Note that even for simpler systems, e.g. in Spring Loaded Inverted Pendulum model which contains a single leg and captures the basic running behaviour, the equations of motion are known to be non-integrable, hence, obtaining an analytical expression for the resulting apex-to-apex return map is impossible [39]. To the best of our knowledge, an analytical expression for the map $\mathbf{G}$ given in (3.1) is not available in literature. Hence, as is done in most of the literature, we resort to numerical computation of this apex return map to identify limit cycles for the AACG model together with their stability. In particular, limit cycles of the model correspond to fixed points x^* of $\mathbf{G}$, defined through

$$\mathbf{x}^* = \mathbf{G}(\mathbf{x}^*) \ . \tag{3.2}$$

Once we identify limit cycles in this fashion, we can determine their local stability by linearizing $\mathbf{G}$ around the corresponding fixed point. This yields a local, linear approximation to the return map with

$$\mathbf{x}_{i+1} - \mathbf{x}^* \approx D\mathbf{G}|_{\mathbf{x}^*}(\mathbf{x}_i - \mathbf{x}^*) \ , \tag{3.3}$$

where $D\mathbf{G}$ denotes the Jacobian of $\mathbf{G}$. The limit cycle is then locally asymptotically stable if all eigenvalues of Jacobian matrix $D\mathbf{G}|_{\mathbf{x}^*}$ are within the unit circle. Due to the hybrid nature of the AACG model and the complexity of its dynamics, there are no currently known closed-form expressions for the apex return map. Consequently, we use a second-order numerical approximation to compute the Jacobian matrix $D\mathbf{G}|_{\mathbf{x}^*}$ for all of our simulations.

For illustration purposes, the limit cycle shown in Fig. 3.1 corresponds to the fixed point $\mathbf{x}^* = [-0.4069, -0.0596, 1.7568]$ for the apex return map, whose Jacobian matrix has eigenvalues $\lambda_1 = -0.5715$, $\lambda_2 = -0.1102$, $\lambda_3 = 0$. Since all eigenvalues are within the unit circle, this limit cycle was found to be locally

asymptotically stable, which was also confirmed by the convergence of simulations starting from initial conditions close to the limit cycle.

Before we proceed with a more thorough characterization of limit cycles for the AACG model, we note that throughout all of our simulations, we observed one of the eigenvalues for all fixed points of the return map to be zero, meaning that the system recovers from perturbations along the associated eigenvector in a single step. For the example in Fig. 3.1, this eigenvector is $\mathbf{x}_0 = [0.0031, 0.4389, 0.8985]$. Fig. 3.2 illustrates AACG trajectories (dashed line) recover from a perturbation in this direction in a single step, right after the swing leg collision. An intuitive explanation for this phenomenon is offered by the fact that the initial swing leg position and velocity are coupled, for which there is a continuum of value pairs that result in the same collision configuration. Consequently, small perturbations which change these two DOF in a coupled fashion are rejected in a single step.
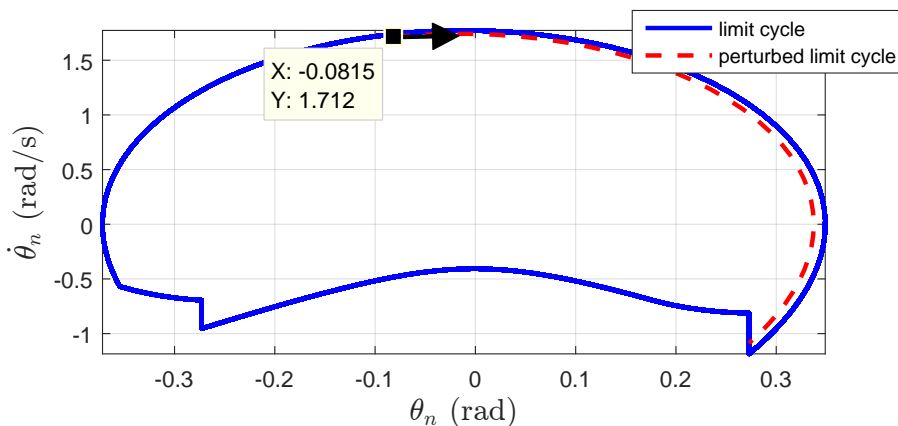

Figure 3.2: AACG trajectories resulting from a perturbation of the limit cycle in the direction of the eigenvector associated with the eigenvalue $\lambda = 0$ for the apex return map. Model completely recovers from this perturbation immediately after toe collision.

In this respect, applying and random perturbation to the limit cycle will not recover in single step. Fig. 3.2 illustrates AACG trajectories (dashed line) recovering from a random perturbation in multiple steps.
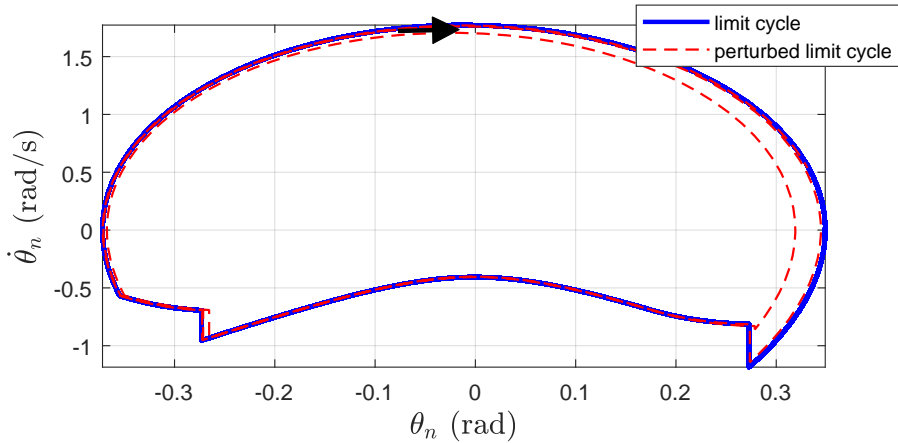
Figure 3.3: AACG trajectories resulting from a random perturbation of the limit cycle. Model recovers from this perturbation after several toe collision.

3.2 Dependence of Gait Stability on Model Parameters

For a more complete picture of system behavior, we investigate the dependence of fixed points of the apex return map and their stability as a function of the ankle spring parameters precompression r_o and stiffness k. In this respect, we start investigating the stability of the model as a function of spring stiffness k where we vary k by an amount of 0.1N/m. Our simulations indicate that for a fixed r_o, there exists a k_{cr}, which may depend on r_o, such that for $k < k_{cr}$ the map $\mathbf{G}$ has only one fixed point which is unstable, whereas for $k > k_{cr}$ the map $\mathbf{G}$ has two fixed points one of which is stable and the other one is unstable. This point is illustrated in Fig. 3.4 for $r_o = 0.01$m, where k_{cr} is found as $k_{cr} = 28.7$N/m. The transition of the stable fixed point to an unstable one is a result of our restriction to a single stride return map since trajectories associated with these fixed points were found to exhibit orbits that were period two and above. We leave a more careful study of these trajectories for future work.

Furthermore, Fig. 3.5 shows all three eigenvalues associated with the stable fixed points and their unstable continuation for small stiffness values as a function of the ankle spring stiffness for three different values of the rest length. Let λ_1,
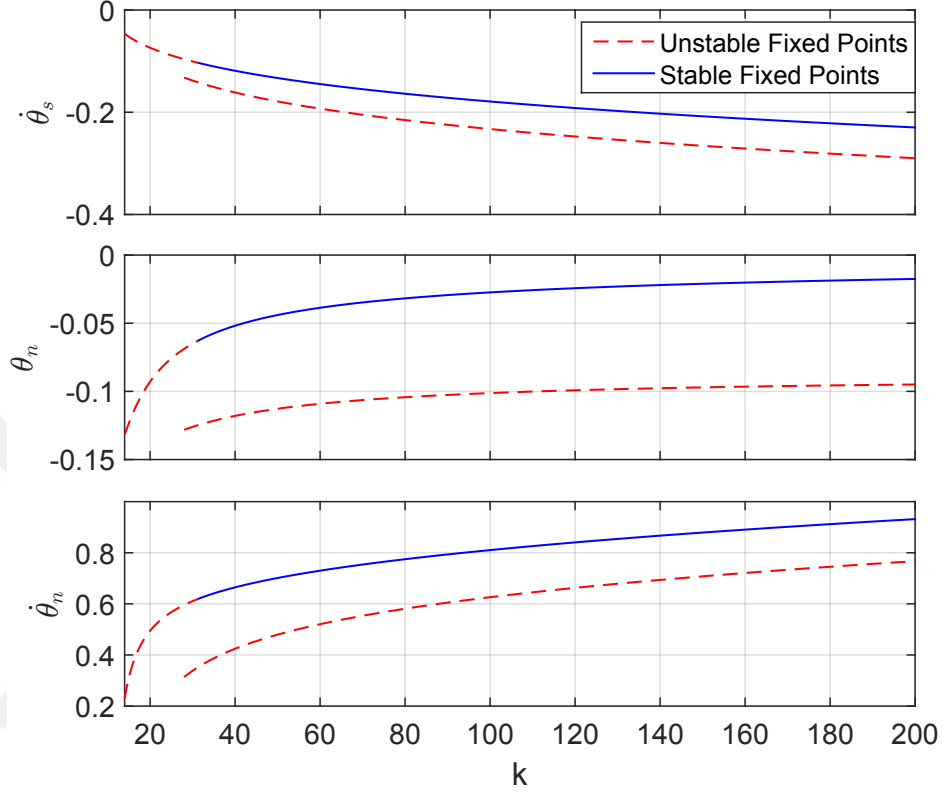
Figure 3.4: State components for fixed points of the AACG model with $r_0 = 0.01m$ as a function of the ankle spring stiffness. Dashed red plot shows unstable fixed points whereas solid blue plots show stable fixed points.

λ_2, λ_3 denote the eigenvalues of $D\mathbf{G}|_{\mathbf{x}^*}$. Note that one of the eigenvalues, say λ_1, is always zero, e.g., $\lambda_1 = 0$ (see the blue line in Fig. 3.5). Also, for a given r_o there exists a k_{cr1} (depending on r_o), such that for $k < k_{cr1}$ the fixed point is unstable, hence at least one eigenvalue has magnitude greated than 1, which is the red portion of one of the eigenvalues. Likewise, for $k > k_{cr1}$, we have a stable fixed point, hence the magnitude of the eigenvalues are less than 1, see Fig. 3.5. Moreover, for a given r_o there exists another critical value k_{cr2} such that for $k < k_{cr2}$ the eigenvalues λ_2 and λ_3 are complex conjugate of each other. Also, our simulations suggest that as r_o is increased, k_{cr1} increases and k_{cr2} decreases.

These results show that the AACG model exhibits stable limit cycles for a large range of spring stiffness and rest length values. This suggests that the use of series elastic actuation for the ankle joint of a walking platform is feasible with
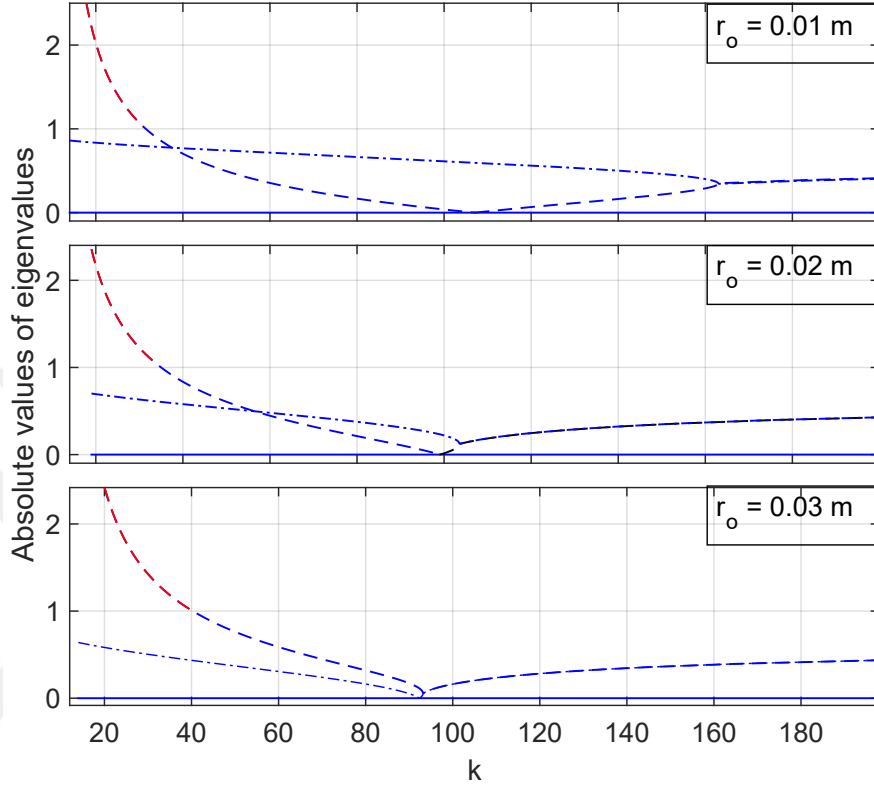
Figure 3.5: Eigenvalues of the linearized apex return map for the stable fixed point with respect to the ankle spring stiffness k and different values of the spring rest length r_0.

promising stability properties.

Then, we investigate the dependence of limit cycles and their stability on the amount of precompression r_0 in the ankle spring prior to its release. Physically, this precompression is often achieved with an actuator connected in series with the ankle spring, changing its rest length before its energy is released through the ankle joint. The left plot in Fig. 3.6 presents the dependence of all three coordinates for the fixed points of the apex return map on this precompression parameter. For a given k, we found the fixed points of $\mathbf{G}$ given by (3.1) as a function of r_o. As depicted in Fig. 3.6, for all choices of precompression with $r_0 \in [0, 0.3]$m, we have found two fixed points. One of these fixed points is always unstable. For the other fixed point, there exists two r_o values r_{omin}, r_{omax} such that for for $r_o < r_{omin}$ and $r_o > r_{omax}$, the fixed point is stable whereas for $r_{omin} < r_o < r_{omax}$ the fixed point is unstable.
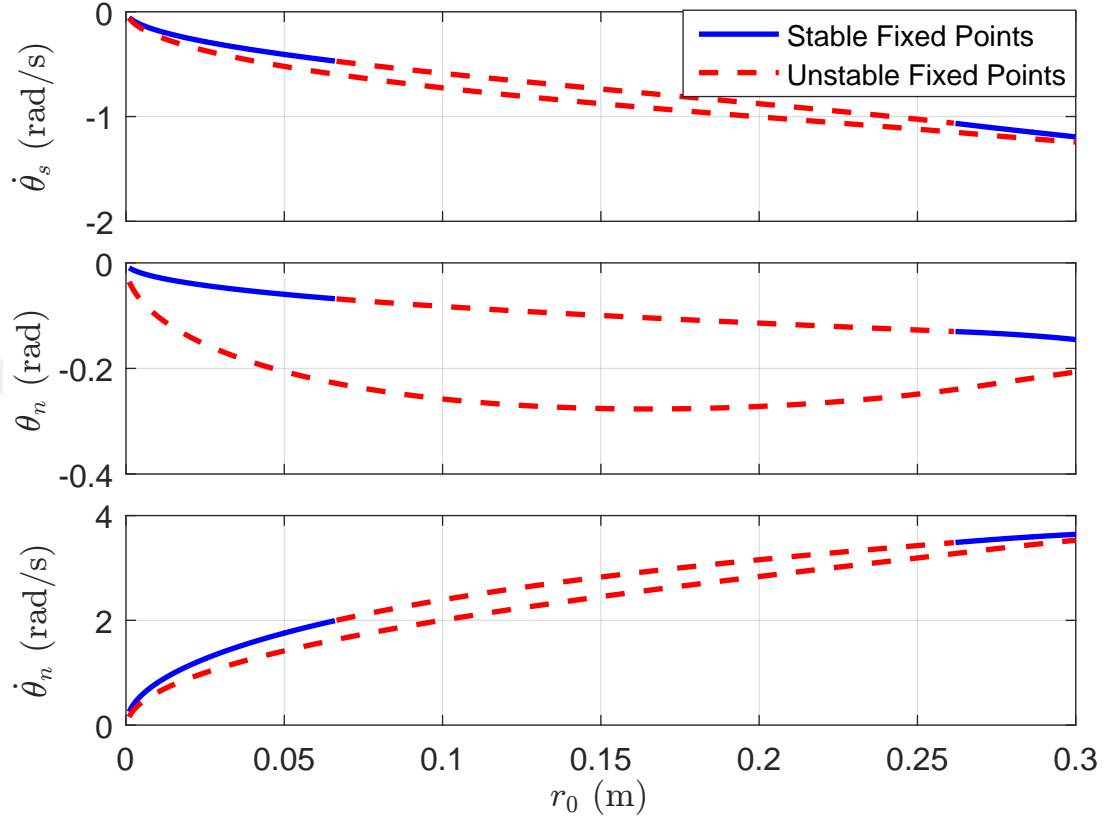
Figure 3.6: Fixed points of the AACG model with $k = 100 \; N/m$ as a function of ankle spring precompression. Solid and dashed plots show stable and unstable fixed points, respectively.

We have also shown cross sections of the basins of attraction associated with stable fixed point associated with $r_0 \in [0, 0.07]$m having grid length of 0.0005m in the plot of Fig. 3.7. These regions were obtained by fixing two coordinates on the stable limit cycle and applying a grid search on the remaining coordinate in a broad range of initial conditions. The parameters of the grid search are r_o, $\dot{\theta}_s$, θ_n and $\dot{\theta}_n$, respectively. The grid size and interval of the initial conditions are given as below. $\dot{\theta}_s$ is varied within the interval $-1.1 < \dot{\theta}_s < -0.02$ rad with grid size of 0.05 rad, θ_n is varied within the interval $-0.13 < \theta_n < 0.14$ rad with grid size of 0.05 rad, $\dot{\theta}_n$ is varied within the interval $0.2 < \dot{\theta}_n < 2.15$ rad with grid size of 0.1 rad.

We also investigated the eigenvalues of $D\mathbf{G}|_{\mathbf{x}^*}$ as a function of r_o. Let λ_1, λ_2, λ_3 indicate the eigenvalues of $D\mathbf{G}|_{\mathbf{x}^*}$. The plots of $|\lambda_1|$, $|\lambda_2|$, $|\lambda_3|$ as a function
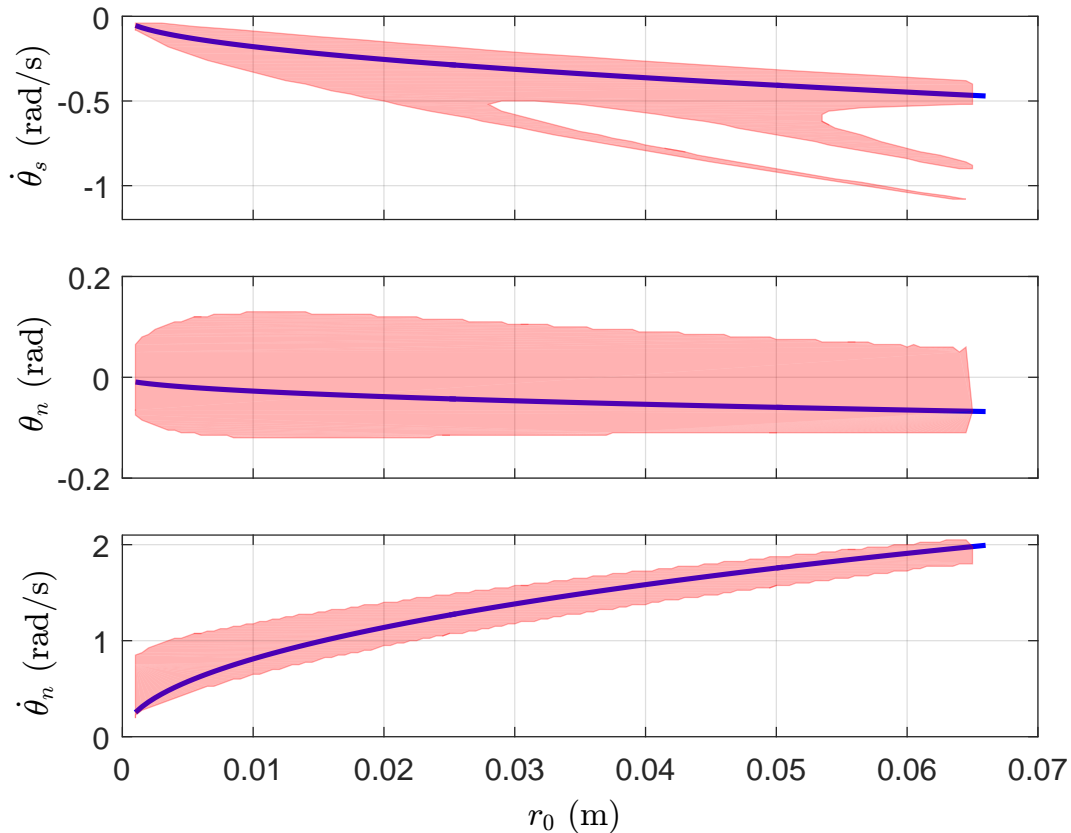
Figure 3.7: Red regions show cross sections of the basin of attraction for stable fixed points associated with $k = 100 \ N/m$ and $r_0 \in [0, 0.07]m$.

of r_o are shown in Fig. 3.8, where the top plot illustrates all three eigenvalues associated with the fixed point that is initially stable and becomes unstable for mid-range choices of r_0. As we noted before, one of the eigenvalues is always zero, corresponding to the dependence of swing leg position and velocity prior to the collision. As the spring precompression increases, the remaining two eigenvalues first become a complex pair, then separate with one converging to zero, and the other crossing the stability threshold. To summarize, our results show that the uncontrolled AACG model exhibits period-1 stable limit cycles (self-stability) for a range of spring precompression values. This suggests that the use of series-elastic actuation for the ankle joint of a walking platform is feasible with promising passive stability properties.
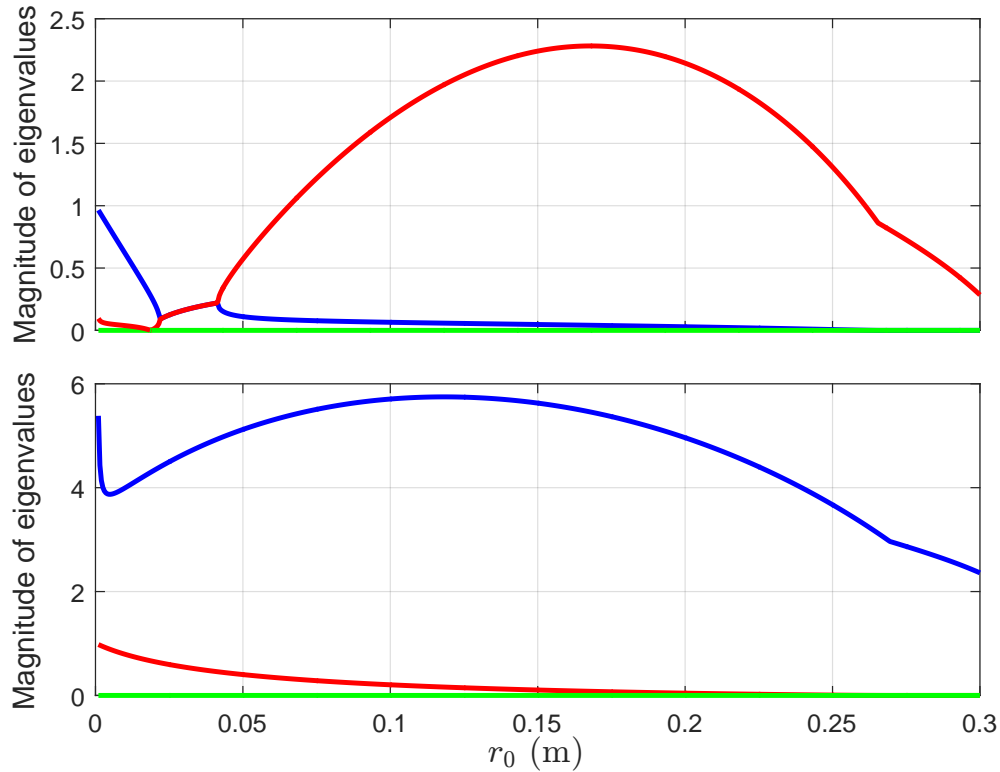
Figure 3.8: Eigenvalues of the linearized apex return map for the fixed point which is stable in a certain parameter range of the spring precompression (top) and the consistently unstable (bottom) fixed point as a function of the ankle spring precompression r_0 with $k = 100\ N/m$.

In the next section, we will explore period doubling behavior outside regions where there are stable gaits. Subsequently, we will propose a feedback controller on the ankle precompression that forces the system to exhibit period-1 stability for any desired forward velocity. The derivations and results given here are presented in [40].

3.3 Bifurcation Regimes for Periodic Walking Gaits

For simplicity, the periodic gait (e.g. limit cycles) corresponding to the fixed points given in section Section 3.1 and Section 3.2 are called period-1 gaits as

well. In addition to period-1 limit cycles, we can also define period-i periodic gaits (e.g. limit cycles) as follows. Let i be a given integer and let us define the i iterate of the apex return map as follows.

$$\mathbf{G}^i = \underbrace{\mathbf{G} \circ \mathbf{G} \circ ... \circ \mathbf{G}}_{i \ times}. \tag{3.4}$$

Similar to fixed points of $\mathbf{G}$, we could also define the fixed points of the map $\mathbf{G}^i$. Let $\mathbf{x}^*$ be a fixed point of $\mathbf{G}^i$. Then the resulting motion is called a period-i periodic motion (or period-i limit cycle) of the AACG model. For illustrative purposes, we give the trajectories of a typical period-2 limit cycle of the AACG model in Fig. 3.12.
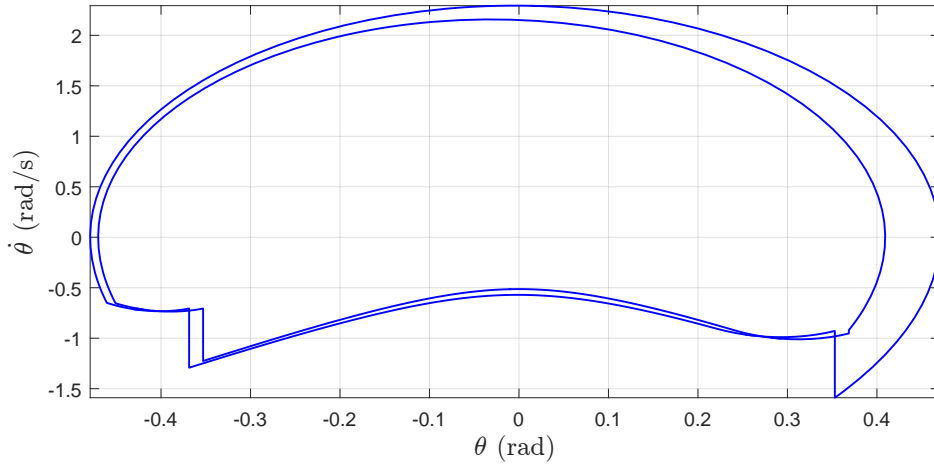
Figure 3.9: Period-2 limit cycle at $r_0 = 0.084$ m and $k = 100$N/m with initial conditions $[\dot{\theta}_s = -0.5705, \theta_n = -0.1463, \dot{\theta}_n = 2.082]$.

Similar to period-1 periodic gaits, period-i periodic gaits could be stable or unstable depending on the eigenvalues of $D\mathbf{G}^i$. Dynamical systems often exhibit *period doubling* behavior coincident with parametric or structural changes in the system behavior, and such phenomena were previously shown to occur with passive dynamic walking models [17]. To explain this phenomena, note that for certain values of r_o the period of the motion bifurcates and such behaviour continually occurs as we increase r_o. This behaviour is called period doubling in dynamical systems and is usually an indication of the existence of chaotic

behaviour beyond a certain r_o value.
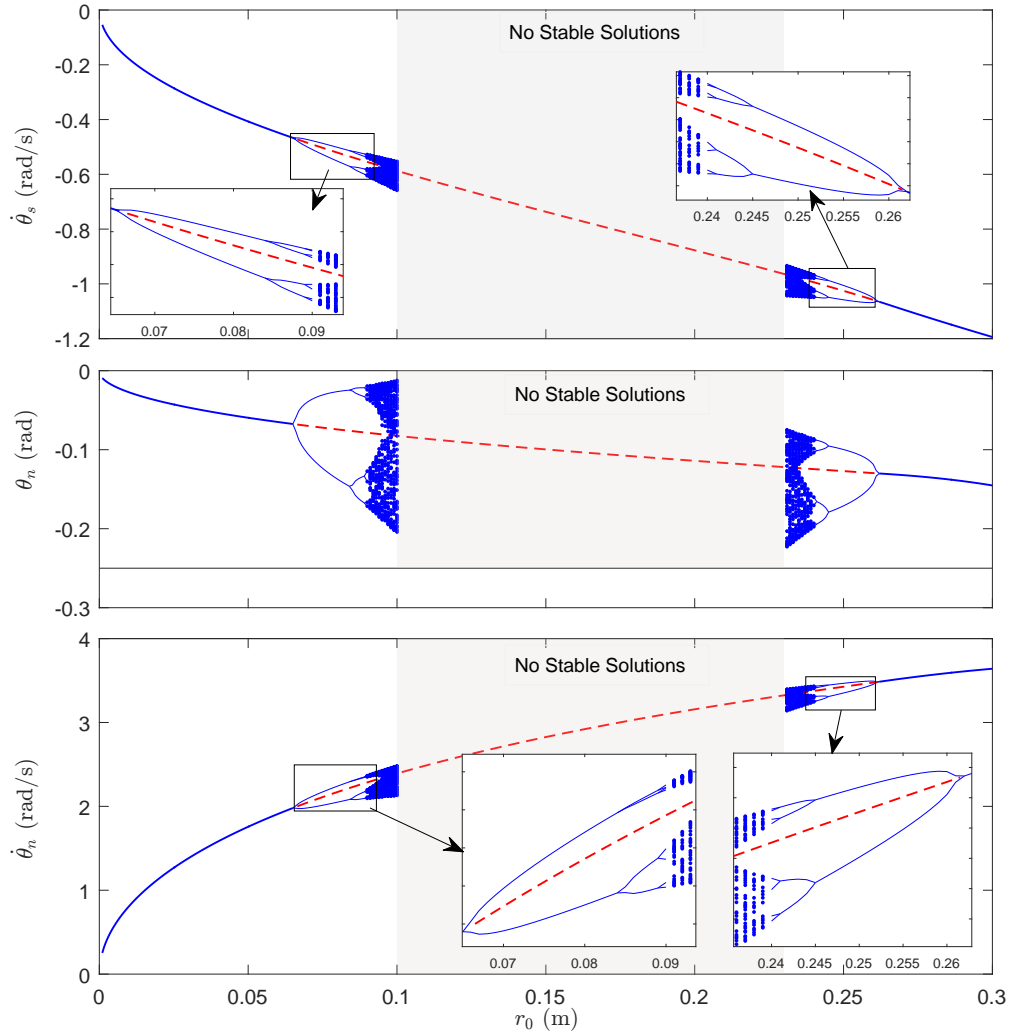
Figure 3.10: The dependence of fixed points of the AACG model on the spring precompression r_0. Solid blue plots show stable fixed points for different periodicities, whereas read dashed plots show unstable, period-1 fixed points only. Regions where period doubling occurs up to period-8 gaits are magnified for clarity.

Stable period-1 AACG walking gaits observed for small values of r_0 eventually become unstable with increasing spring precompression. The parameter value at which one of the eigenvalues crosses outside the unit circle ($r_0 = 0.06573m$ for the example in Fig. 3.6) marks the first bifurcation point, where period doubling

34

occurs and a stable period-2 walking gait is introduced. This gait is increasingly asymmetric, consisting of a short and a long step. For larger values of spring precompression, short step becomes shorter and long step becomes longer. Further increases in the spring precompression parameter eventually destabilize this period-2 gait, leading to a stable period-4 gait. Fig. 3.10 illustrates this period doubling behavior, and Fig. 3.12, Fig. 3.13, Fig. 3.14, Fig. 3.15 shows phase space projections of limit cycles associated with period-2, period-4, period-8 gaits and chaotic behavior, respectively. Finally, Fig. 3.11 illustrates the magnitudes of eigenvalues associated with period-1 to period-4 gaits, showing that period doubling occurs when a particular gait becomes unstable with its largest magnitude eigenvalue crossing the unit circle.
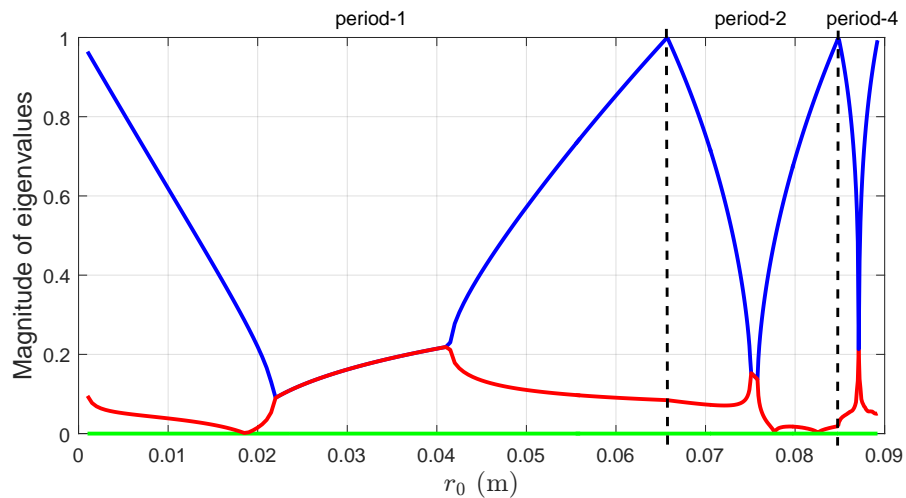
Figure 3.11: Magnitude of eigenvalues associated with stable gait periodicities up to 4. Since the return map covers multiple steps for period-2 and period-4 regions, associated eigenvalues were plotted as $\lambda^{1/2}$ and $\lambda^{1/4}$, respectively, for continuity and better comparison with period-1 eigenvalues. Eigenvalues beyond period-4 were excluded since they are observed in a very narrow region.
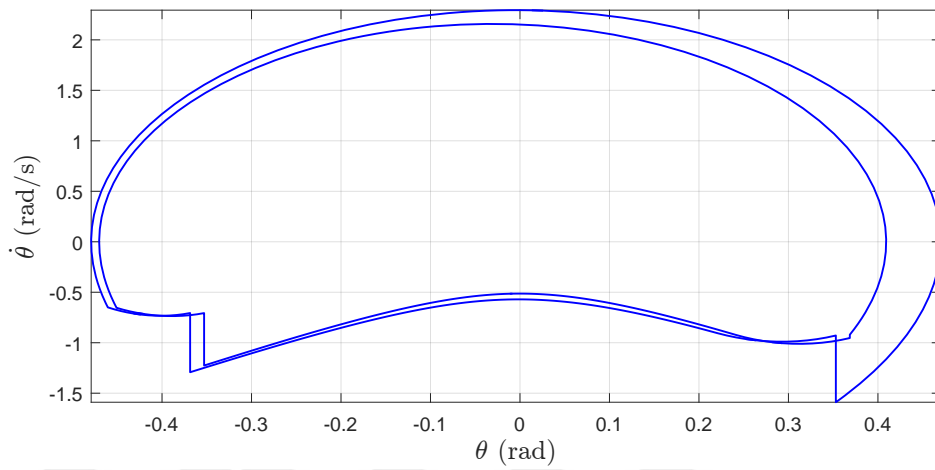
Figure 3.12: Period-2 limit cycle at $r_0 = 0.084$.
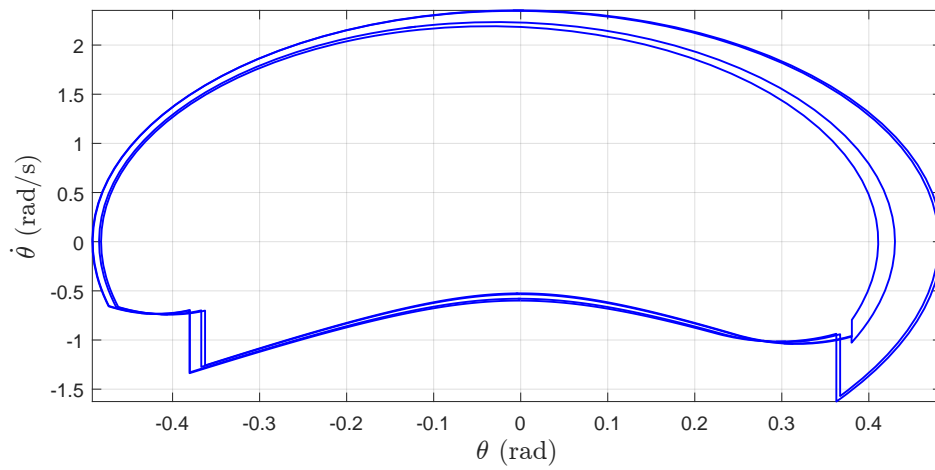
Figure 3.13: Period-4 limit cycle at $r_0 = 0.089$.
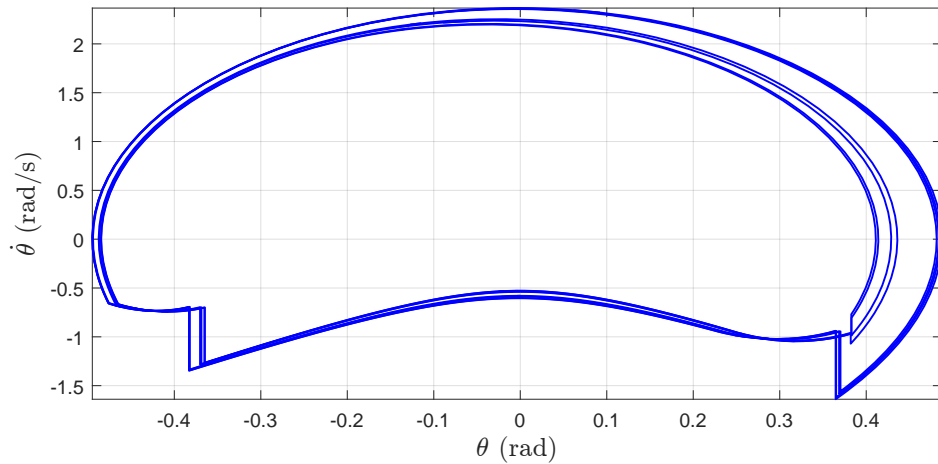
Figure 3.14: Period-8 limit cycle at $r_0 = 0.09$.
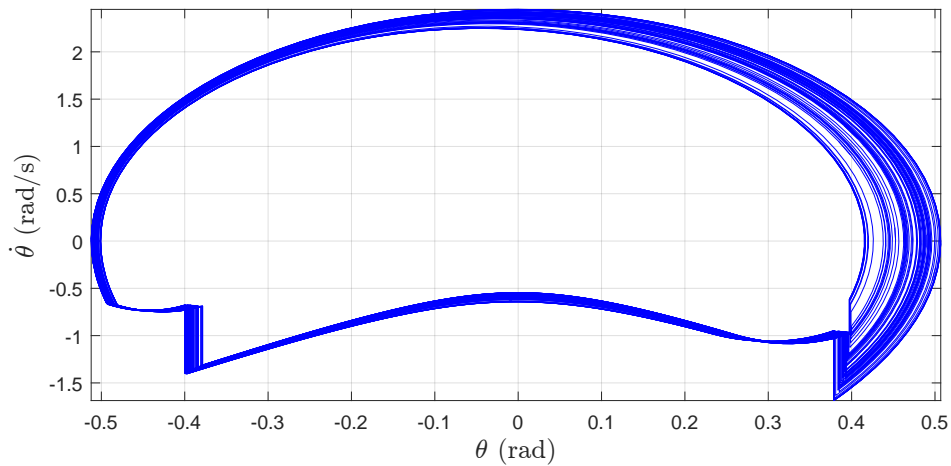
Figure 3.15: Non-periodic, sustained walking at $r_0 = 0.098$.

We have also found, by evaluating parameter values at which period doubling occurs, listed in Table 3.1 for up to period-32 gaits, that the ratio of distances between successive bifurcations seem to converge to the Feigenbaum constant 4.669 [41]. Feigenbaum constant is a universal constant for functions approaching chaos via period doubling bifurcations. The Feigenbaum constant characterizes the geometric approach of the bifurcation parameter to its limiting value.

Beyond $r_0 > 0.0905$ m, we were unable to find any periodic solutions, with

n	New period	$r_0[n]$	$\dfrac{r_0[n-1] - r_0[n-2]}{r_0[n] - r_0[n-1]}$
1	2	0.06573	-
2	4	0.08486	-
3	8	0.08927	4.3379
4	16	0.09023	4.5937
5	32	0.090438	4.6154

Table 3.1: Spring precompression parameter values at which period doubling occurs, together with ratios between successive parameter ranges for each period.

each successive apex state different than previous ones even though the model kept walking indefinitely. This suggests a chaotic gait, where the locomotion is sustained, but no periodicity can be identified. For choices of spring precompression beyond this value, we evaluated the model for over 1000 steps, then recorded the last 100 apex states. Individual dots in Fig. 3.10 plot each step from these runs, showing chaotic behavior. Finally, beyond $r_0 > 0.1$ m the AACG model could no longer sustain locomotion, with its return map having only unstable fixed points.

Interestingly, if r_0 is increased further, the AACG model eventually restarts being able to sustain locomotion. In particular, when the rest length reaches $r_0 = 0.2255$ m, a sustained but chaotic gait is observed, with no periodicity that we could identify. Further increases recover period-2^n gaits, with parameter values at which the periodicity changes shown in Table 3.2. Period-1 gaits are observed again beyond $r_0 = 0.261079$ m. Similar to before, the ratio of the distances between successive bifurcations in this region also seem to converge to the Feigenbaum constant.

The occurrence of chaotic gaits beyond a certain spring precompression and the later recovery of symmetric period-1 stable gaits can be partially explained in terms of the energy input and losses in the AACG model. As the rest length increases, we inject more energy to the system and in response, the model attempts to walk faster causing previously stable fixed points to destabilize. This leads to a regime of period doubling bifurcations, chaos and eventually complete instability, which is consistent with existing literature on the PCG model [17, 18].

n	New period	$r_0[n]$	$\dfrac{r_0[n-1] - r_0[n-2]}{r_0[n] - r_0[n-1]}$
1	2	0.26108	-
2	4	0.24464	-
3	8	0.240624	4.0895
4	16	0.239728	4.47
5	32	0.239534	4.6186

Table 3.2: Spring precompression parameter values at which changes in periodicity occur for large values of r_0, together with ratios between successive parameter ranges for each period doubling (coming backwards from $r_0 = 0.3m$).

Different from those studies, however, the AACG model does not rely on the conservation of angular momentum to derive the collision map. Even though we can not use this principle due to the active double stance phase with both legs remaining on the ground, the recovery of periodic gait for larger values of the spring precompression can be explained with one of our previously described assumptions. In particular, beyond a certain value of precompression (and hence forward speed), the angle between the legs approaches $\pi/2$, at which point the post-collision angular momentum vanishes since the body velocity at the collision is then aligned with the colliding leg. This brings the model to a full stop after the collision. Moreover, since we assumed that the ankle acts in a unidirectional manner with $\dot{r}^+ \geq 0$, inter-leg angles larger than $\pi/2$ also have zero post-collision velocities. We believe that this property of the AACG model is what leads to the recovery of periodic gaits beyond a certain spring precompression, with the increase in collision losses compensating for the larger spring energy injected into the system. Fig. 3.16 depicts the inter-leg angle, $\theta_s + \theta_n$, for the fixed points of the system over the entire range of the spring precompression, showing the disappearance and subsequent recovery of periodic gaits. The derivations and results given here are presented in [42].
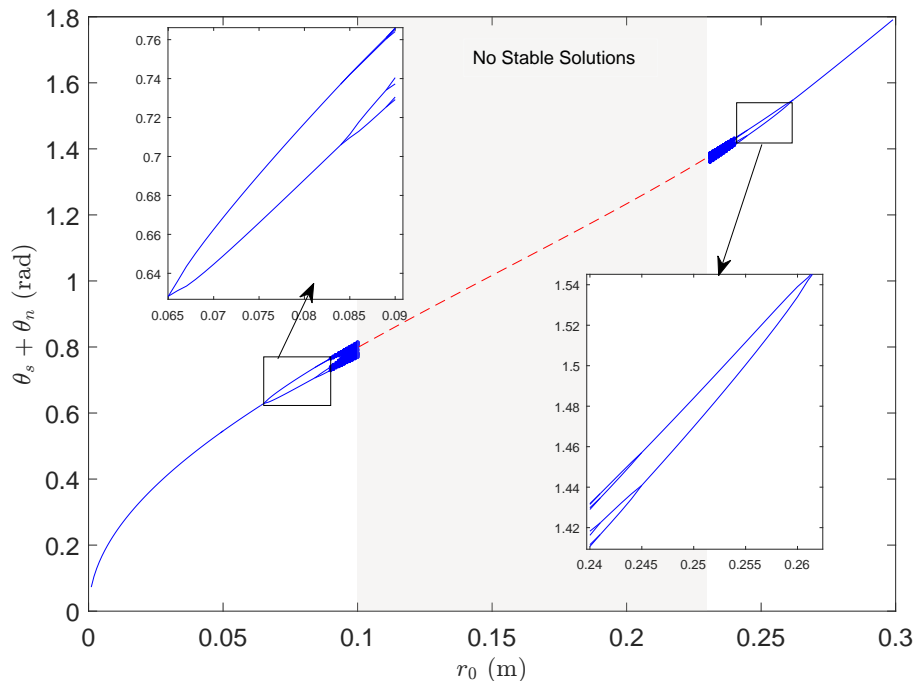
Figure 3.16: Dependence of the inter-leg angle $\theta_s + \theta_n$ for the fixed points of the AACG model on the spring precompression parameter. Solid blue plots shows stable fixed points with different periodicities whereas the red dashed plot shows unstable period-1 fixed points. Bifurcation regions up to period-8 gaits are magnified for a clearer view.

3.4 Period-3 Doubling

In addition to period doubling as indicated in previous section, which leads to period-2^n limit cycles, our model also exhibits period-3 stable limit cycles as well. In other words, illustrated in Fig. 3.17, for $r_o = 0.067$m the AACG model exhibits period-3 motion and the motion for $r_o = 0.068$m is period-6. This leads to a new period doubling sequence leading to period-3 motions. Note that existence of period-3 motions is usually considered as another indicator of chaotic behaviour [43].
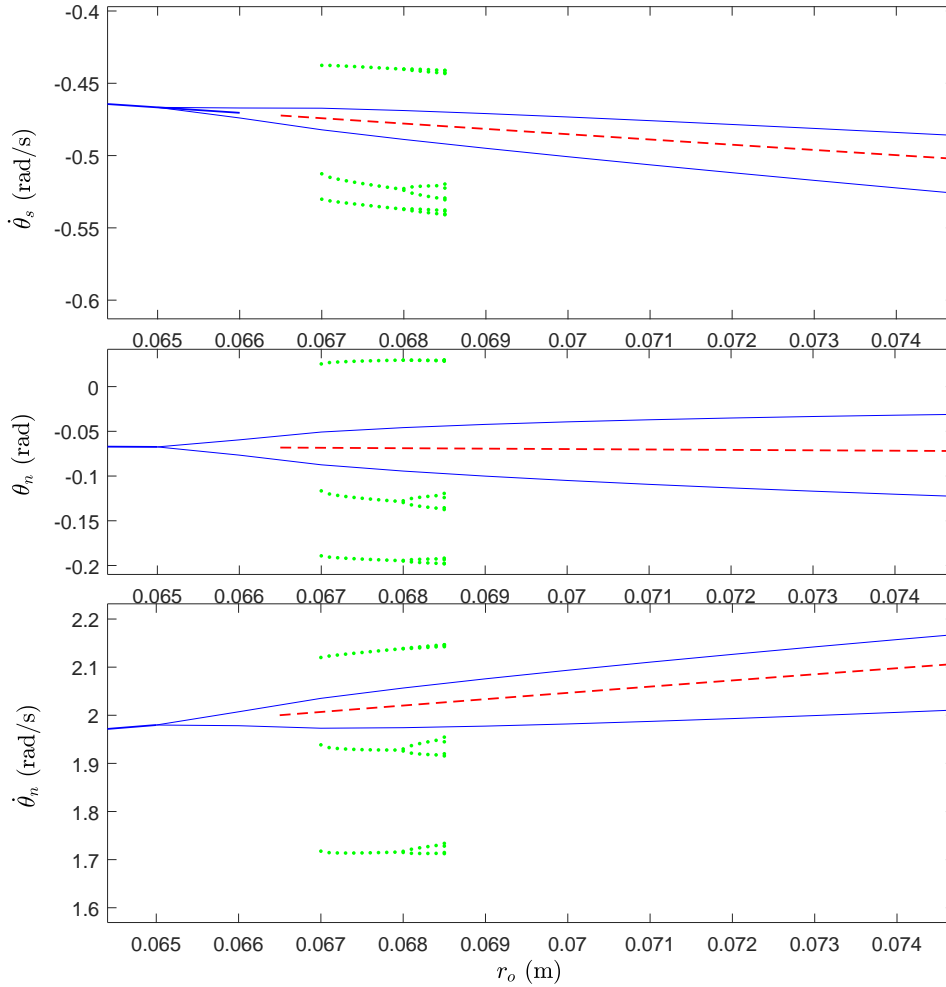
Figure 3.17: The dependence of period-3 fixed points of the AACG model on the spring precompression r_0.

3.5 Feedback Control Through the Ankle Spring

As shown by Fig. 3.6, a fixed choice of the spring precompression r_0 does not always yield a stable limit cycle for walking with the AACG model. It is, however, encouraging to note that period-1 fixed points exist for the entire range of this parameter, covering a wide range of forward velocities, which is directly related to the stance leg velocity $\dot{\theta}_s$ at apex (i.e. the top plot in Fig. 3.6). If it were possible to achieve stable walking for this entire range, we would effectively obtain a

walking model whose walking speed can be effectively controlled.

To this end, we propose to use feedback control on the ankle spring precompression, which can, in practice, be implemented using series-elastic actuation as evidenced by many successful legged platforms with similar designs [35, 36]. This can be accomplished through a simple proportional feedback law that preserves period-1 fixed points of Fig. 3.6, while ensuring that one of the fixed points has all of its eigenvalues within the unit circle. We begin by representing the stance leg angular velocity component of the fixed point which is stable in a certain parameter range of the spring precompression of Fig. 3.6 in functional form as

$$\dot{\theta}_s^{fp} = f(r_0) \, . \tag{3.5}$$

This function characterizes the fixed points and for our choice of dynamic parameters, it is monotonic in r_0 and is hence invertible. Note that, the relation between r_o and $\dot{\theta}_s$ is almost linear hence one can fit a function such as $\dot{\theta}_s = \alpha r_o$. In order to capture the relation between r_o and $\dot{\theta}_s$ for a desired velocity $\dot{\theta}_s^*$, we find an open-loop spring precompression $r_0^* = f^{-1}(\dot{\theta}_s^*)$ that would yield a limit cycle coincident with the desired gait. To address this problem, we propose the discrete-time feedback law

$$r_0[k] = f^{-1}(\dot{\theta}_s^*) - k_p(\dot{\theta}_s^*[k] - \dot{\theta}_s[k]) \, , \tag{3.6}$$

where $k = 0, 1, 2, ..., n$ are the discrete time instances at apex points, k_p is a proportional gain constant which is chosen appropriately to stabilize the fixed point. This law adjusts the spring precompression based on the measured error in the stance leg velocity at apex through negative feedback. As shown in Fig. 3.20, increasing the gain k_p allows us to adjust the eigenvalues associated with the period-1 limit cycle to lie within the unit circle, effectively stabilizing otherwise unstable fixed points for the AACG model. Since the feedback law (3.6) leaves fixed points of the return map unchanged, it allows exact, stable control of walking at a desired apex velocity. Fixed points with larger periodicities seem to disappear under this regime for large enough values of k_p.
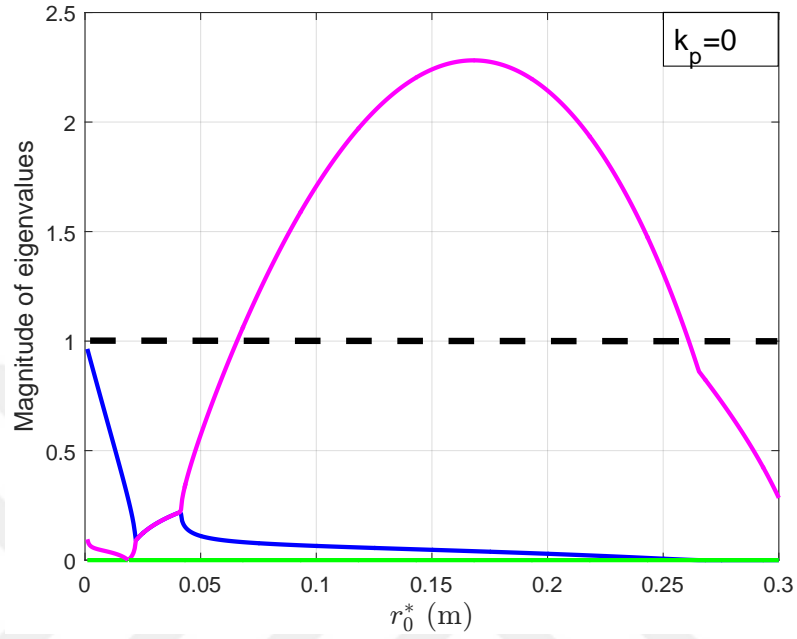
Figure 3.18: The dependence of AACG fixed point stability on the feedback gain k_p. The plot shows the eigenvalues of the uncontrolled system, The dashed lines mark the unit magnitude threshold for the eigenvalues.
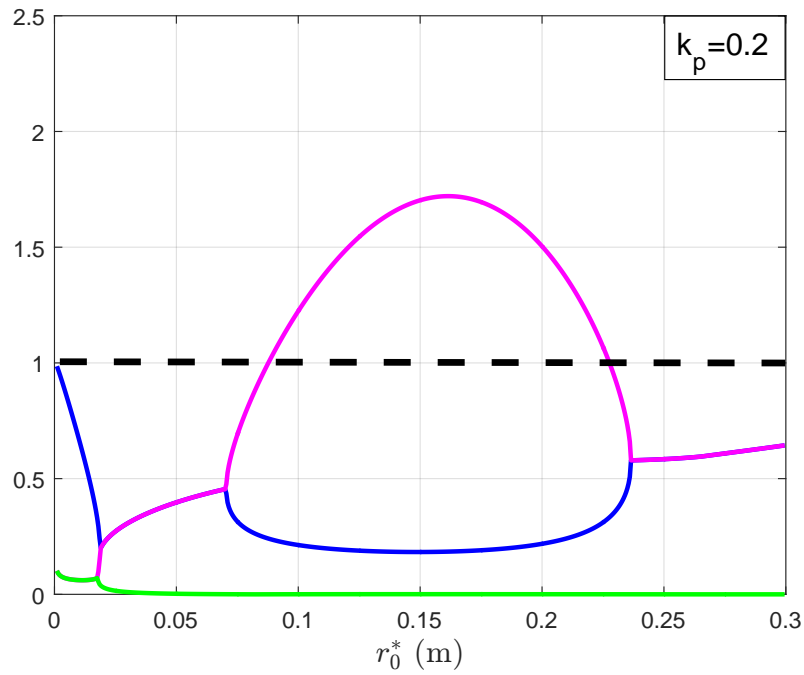

Figure 3.19: The plot shows the eigenvalues with $k_p = 0.02$.
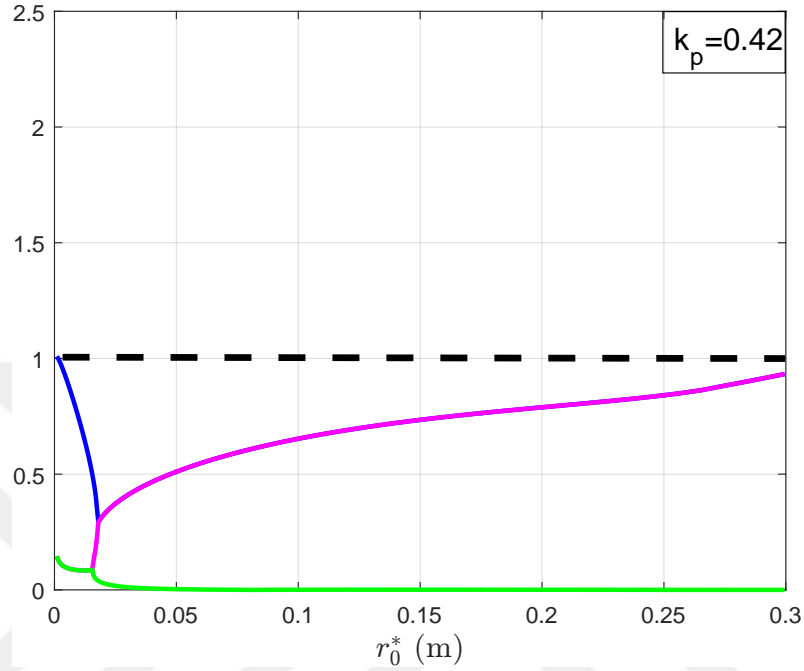
Figure 3.20: The plot shows the eigenvalues with $k_p = 0.042$.

In order to demonstrate the performance of the feedback controller we perturbed the stance leg angular velocity by 0.05 rad/s and evaluated the model for 20 steps with parameters $r_o = 0.05$m, $k = 100$N/m. The initial conditions are $[-0.3570, \ -0.0096, \ 1.8068]$ and the desired apex velocity is $\dot{\theta}_s = -0.4070$. Fig. 3.21 illustrates the error $(\dot{\theta}_s^*[k] - \dot{\theta}_s[k])$ at each apex instant. After 10 steps the controller achieves the desired apex velocity. The derivations and results given here are presented in [44, 45].
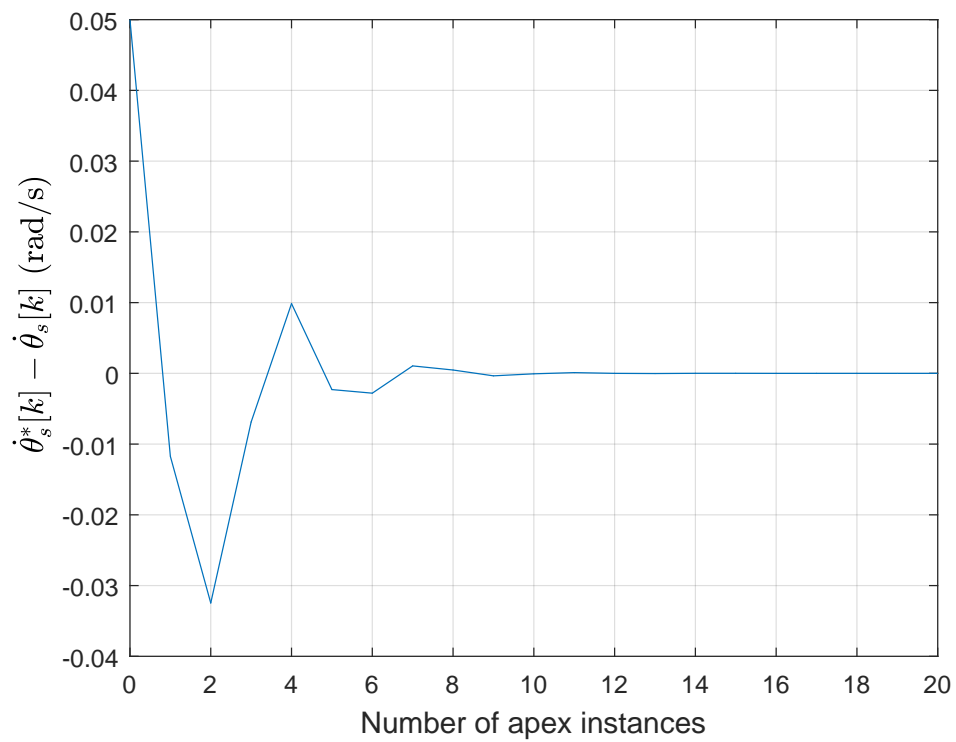
Figure 3.21: The plot shows the error $(\dot{\theta}_s^*[k] - \dot{\theta}_s[k])$ at each apex instant.

Chapter 4

Stability of Uphill and Downhill Walking with the AACG Model

In this chapter, we aim to investigate the walking behaviour of our model on uphill and downhill slope and extend the stability analysis of walking on uphill and downhill terrains.

4.1 Periodic Walking Gaits Apex Return Map

We examine the AACG walking behaviours by identifying periodic limit cycles. To achieve walking on a limit cycle, we fix all the system parameters and evaluate the model at two different ground slopes. For explanatory purposes, we define the swing and support leg as Leg A and Leg B, respectively. Fig. 4.1 and Fig. 4.2 depicts only the phase space trajectories of angle and angular velocity of Leg A for period-1 walking on downhill and uphill slopes, respectively. Similar to level ground walking, at the instant marked with 1, leg B collides with the ground, resulting in a discontinuous change in velocities. Note that, on downhill slope walking due to the potential energy attained during swing phase, the magnitude of impact of downhill slope walking occurring during the collision is larger than

uphill slope walking. Consequently, the ankle spring in leg A injects less energy during downhill slope walking compared to uphill slope walking in order to maintain stable walking. At instants mark with 2 ankle spring in leg A lifts off after and reaches its rest length and Leg A becomes the new swing leg. Instants marked with 3 and 4 correspond to the ground collision of leg A and the liftoff event for leg B completing the limit cycle.
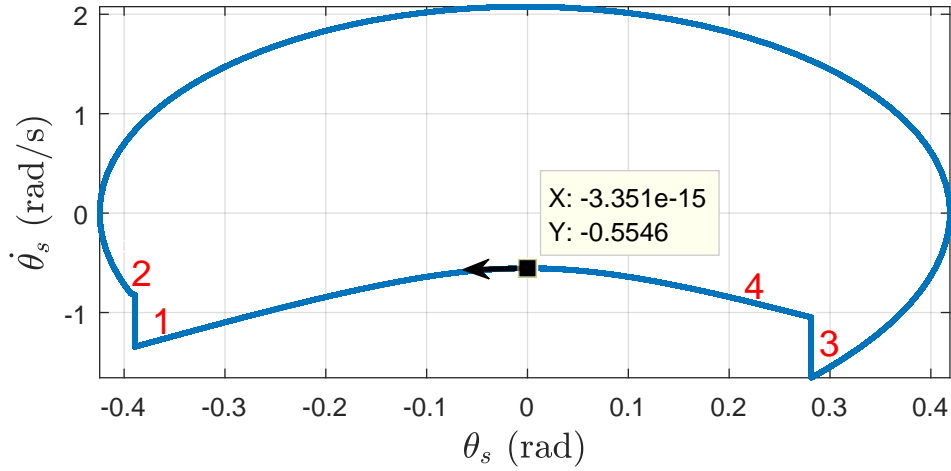
Figure 4.1: Phase space trajectories for an example periodic gait generated by the AACG model for sloped ground. The figure illustrates walking on the downhill for $r_0 = 0.001\ m$, $\phi = -0.054\ rad$ with the model parameters chosen as $M = 1\ kg$, $m = 0.01\ kg$, $l = 1\ m$, $k = 100\ N/m$.

The limit cycle for downhill walking in Fig. 4.1 recurrently intersects Poincaré section at $\theta_s = 0\ rad$, $\dot{\theta}_s = -0.5546\ rad/s$, $\theta_n = -0.0111\ rad$, $\dot{\theta}_n = 2.0463\ rad/s$, and it corresponds to a fixed point of the discrete Poincaré map. Likewise, for uphill walking, $\theta_s = 0\ rad$, $\dot{\theta}_s = -0.1524\ rad/s$, $\theta_n = -0.1563\ rad$, $\dot{\theta}_n = 1.1919\ rad/s$, is a fixed point of the discrete Poincaré map for limit cycle which is illustrated in Fig. 4.2.

During inclined ground walking, the Poincaré section is chosen as the vertical configurations of the supporting leg with $\theta_s = 0$ and $\theta_s > 0$. This configuration corresponds to the apex point. To guarantee that we have a valid Poincaré map we need to eliminate some faulty solutions in which the cross-section of the resulting trajectories are not transversal with the Poincaré section. These faulty cases are listed below.
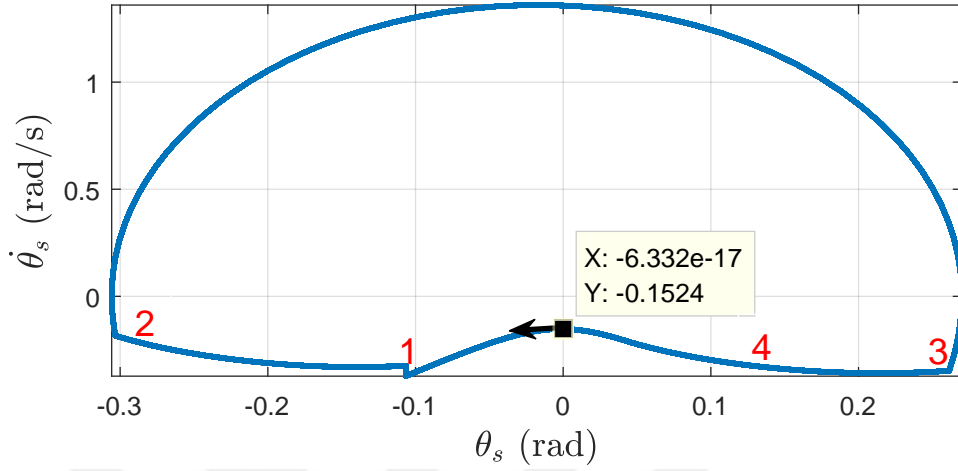
Figure 4.2: Phase space trajectories for an example periodic gait generated by the AACG model for sloped ground. The figure illustrates walking on the uphill for $r_0 = 0.076\ m$, $\phi = 0.076\ rad$ with the model parameters chosen as $M = 1\ kg$, $m = 0.01\ kg$, $l = 1\ m$, $k = 100\ N/m$.

- Model walking backwards, with $\dot{\theta}_s \geq 0$.

- Insufficient distance between legs, with $r_0 \leq d$.

- Trailing heel going underground during the DSS phase, with $\dot{r}^+ < 0$.

- Torso mass M going below the ground, with $\cos(\theta_s + \phi) < 0$.

- The inter-leg angle becoming unreasonably large, with $\theta_s + \theta_n > \pi$.

- Spring thrust being insufficient to ensure liftoff, with $r < r_0$.

Avoiding these faulty conditions ensure that all state trajectories of the AACG model move transversally through the Poincaré section at the apex point during simulations.

To define the return map of the AACG model for walking on inclined slopes, let $x := [\dot{\theta}_s, \theta_n, \dot{\theta}_n]^T$ denote the co-dimension one state vector within the Poincaré section. Given Poincaré states x_i and x_{i+1} for the ith and $i + 1^{th}$ apex points, respectively, the AACG return map is given as

$$\mathbf{x}_{i+1} = \mathbf{G}(\mathbf{x}_i)\ . \tag{4.1}$$

The analytical expression for the map $\mathbf{G}$ given in (3.1) is not available in literature. Hence, we numerically compute this apex return map to identify limit cycles for the AACG model together with their stability. In this context, limit cycles of the model correspond to fixed points x^* of $\mathbf{G}$, defined through

$$\mathbf{x}^* = \mathbf{G}(\mathbf{x}^*) \, . \tag{4.2}$$

After identifying limit cycles, we can determine their local stability by linearizing $\mathbf{G}$ around the corresponding fixed point. The linearization yields a local, linear approximation to the return map with

$$\mathbf{x}_{i+1} - \mathbf{x}^* \approx D\mathbf{G}|_{\mathbf{x}^*}(\mathbf{x}_i - \mathbf{x}^*) \, , \tag{4.3}$$

where $D\mathbf{G}$ denotes the Jacobian of $\mathbf{G}$. The limit cycle is then locally asymptotically stable if all eigenvalues of Jacobian matrix $D\mathbf{G}|_{\mathbf{x}^*}$ are within the unit circle.

The limit cycle in Fig. 4.1 corresponds to the fixed point $\mathbf{x}^* = [-0.5546, -0.0111, 2.0463]$ for the apex return map with slope $= -.054$ radians and the eigenvalues of the Jacobian matrix are $\lambda_1 = -0.9904$, $\lambda_2 = 0$, $\lambda_3 = -0.1460$. Similarly, the limit cycle in Fig. 4.2 corresponds to the fixed point $\mathbf{x}^* = [-0.1524, -0.1563, 1.1919]$ for the apex return map with slope $= 0.076$ and the eigenvalues of the Jacobian matrix are $\lambda_1 = -0.9995$, $\lambda_2 = 0$, $\lambda_3 = -0.0614$. All the eigenvalues being inside unit circle indicates that these two limit cycles are locally asymptotically stable.

Note that for both downhill and uphill walking limit cycles, one of the eigenvalues for the fixed point of the return map is zero, meaning that the system recovers from perturbations along the associated eigenvector in a single step. We have also observed the same behaviour for level ground walking hence, this phenomena seems to be a characteristic property of the model. The eigenvectors associated with the zero eigenvalues are given as $\mathbf{x}_0^d = [0.1585, \; -0.4181, \; 0.8984]$ and $\mathbf{x}_0^u = [0.0875, \; 0.3344, \; 0.9383]$ for downhill and uphill walking, respectively.

Fig. 4.3 and Fig. 4.4 illustrates AACG trajectories (dashed line) recover from a perturbation in this direction in a single step, right after the swing leg collision for downhill and uphill walking respectively.
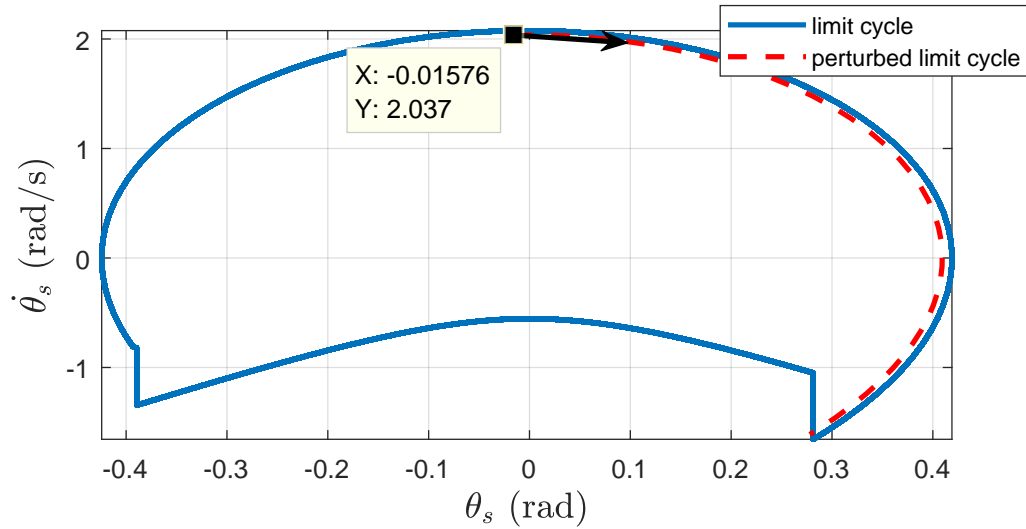

Figure 4.3: AACG trajectories for downhill walking resulting from a perturbation of the limit cycle in the direction of the eigenvector associated with the eigenvalue $\lambda = 0$ for the apex return map.

In this respect, applying and random perturbation to the limit cycles will not recover in single step. Fig. 4.5 and Fig. 4.6 illustrates AACG trajectories (dashed line) recovering from a random perturbation in multiple steps for downhill and uphill walking, respectively.
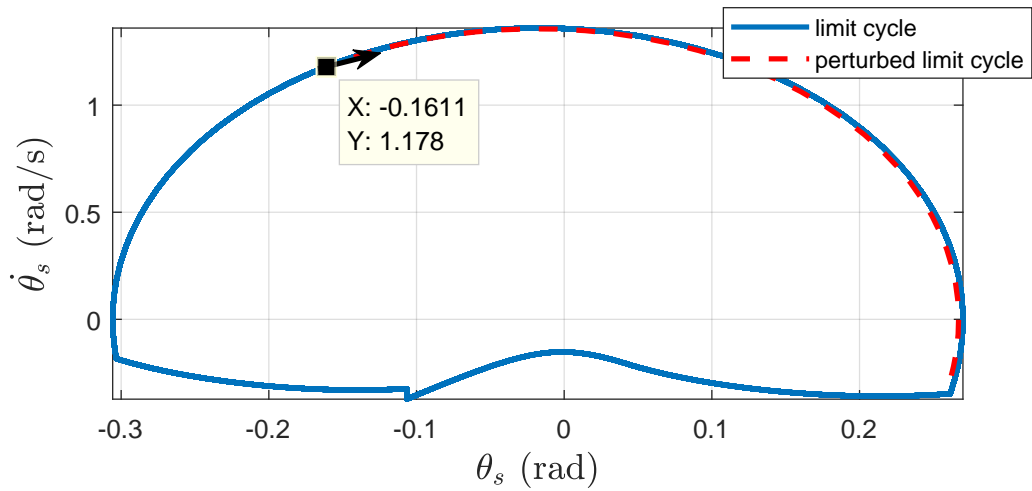
Figure 4.4: AACG trajectories for uphill walking resulting from a perturbation of the limit cycle in the direction of the eigenvector associated with the eigenvalue $\lambda = 0$ for the apex return map.
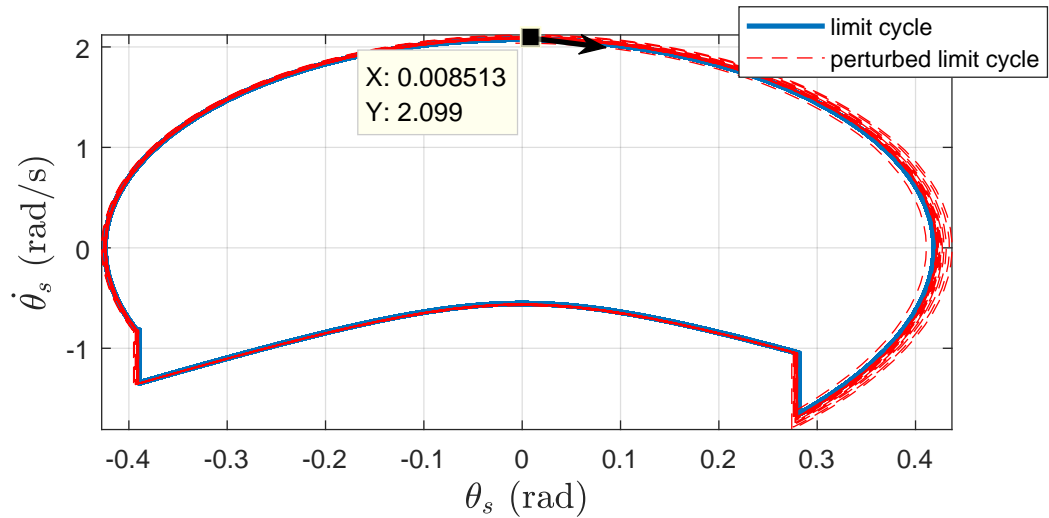
Figure 4.5: AACG trajectories for downhill walking resulting from a random perturbation of the limit cycle. Model recovers from this perturbation after several toe collision.
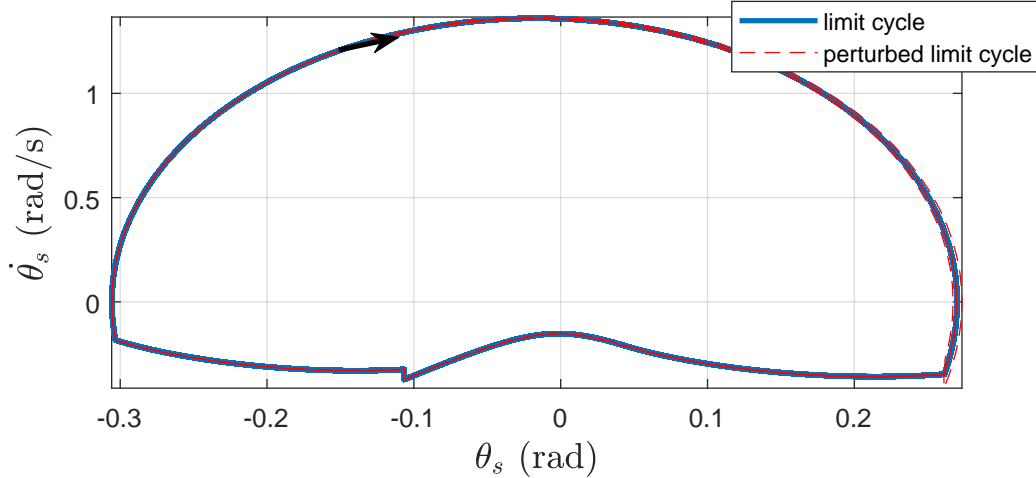
Figure 4.6: AACG trajectories for uphill walking resulting from a random perturbation of the limit cycle. Model recovers from this perturbation after several toe collision.

4.2 Finding Fixed Points

We employ Matlab fminsearch function to find fixed points of the model (i.e. the solutions of (3.1)) as we vary the model parameters of spring precompression r_0 and ground slope ϕ. Initially, we start from one fixed point given a specific set of model parameters. Then we change the precompression r_0 by a small amount and we evaluate the model such that it evolves into a new steady state walking phase. Finally, we utilize fminsearch function to make sure that this steady state walking states corresponds to a new fixed point as follows

$$|\mathbf{G}(\mathbf{x}^*) - \mathbf{x}^*| < \epsilon \,, \tag{4.4}$$

where fminsearch guarantees ϵ to be $\epsilon < 10^{-10}$. We choose to alter precompression variable instead of ground slope since the change in slope yields a drastic change in the kinematics hence the model becomes more fragile to the changes in slope. We iterate this process of fixed point finding and continue increasing precompression parameter until we reach period-2 stable walking gaits. At this point, we sample poincaré map at two successive steps to find the fixed point and we continue

52

increasing precompression parameter until we come across with stable period-4 walking gaits and we sample Poincaré map at four steps. We continue with this process until we reach upto stable period-8 walking gaits where we stop searching for stable fixed points. At this point, we further increase precompression variable to search for chaotic walking patterns where there is no identifiable fixed points, yet the model sustains walking behaviour. This is accomplished by evaluating the model starting from the Poincaré section and labeling this point as chaotic walking if the model successively reaches to 1000 steps. The search for chaotic walking patterns continues until the model no longer sustains walking given the initial conditions.

The above procedure is obtained by varying only precompression variable. We extend this search of period doubling bifurcation scheme to grid search by introducing the ground slope variable. The above process is repeated from negative slope values (downhill slopes) to positive slope values (uphill slopes) where the grid size is 0.0005 m for precompression and 0.0002 rad for ground slope.

4.3 Period Doubling Bifurcation Regions of Uphill and Downhill Walking

We investigate the dependence of limit cycles and their stability on the amount of downhill, uphill slopes and spring precompression r_0 in the ankle spring to investigate the performance of our model on sloped grounds. First, we define various terms and introduce various notations which will be utilized in the rest of the thesis. We start by defining S_Γ to be the Poincaré section at apex state q_a. Hence, $\mathbf{G} : S_\Gamma \to S_\Gamma$ and clearly $\mathbf{G}$ depends on r_o, ϕ, q_a where q_a depends on (r_o, ϕ). Let $p := \{r_o, \phi\}$ denote system parameters of spring precompression and ground slope. Obviously, the map $\mathbf{G}$ depends on p. To denote this dependence, we will refer to the map $\mathbf{G}$ as $\mathbf{G}_p$ in the sequel. Then, the fixed point set Γ_i is defined as

$$\Gamma_i = \left\{ q_e = \{p, q_a\} \ | \ \mathbf{G}_p^i(q_a) = q_a \right\}. \tag{4.5}$$

Here, $\mathbf{G}_p^i(q_a)$ denotes i^{th} iteration of Poincaré map and it is given as

$$\mathbf{G}_p^i(q_a) = \underbrace{\mathbf{G}_p \circ \circ \circ \mathbf{G}_p}_{i}, \tag{4.6}$$

where $i = 1, 2, ...$

For example, period-2 and period-4 limit cycles are illustrated for downhill and uphill walking as in the Fig. 4.7, Fig. 4.8, Fig. 4.9, Fig. 4.10, respectively.
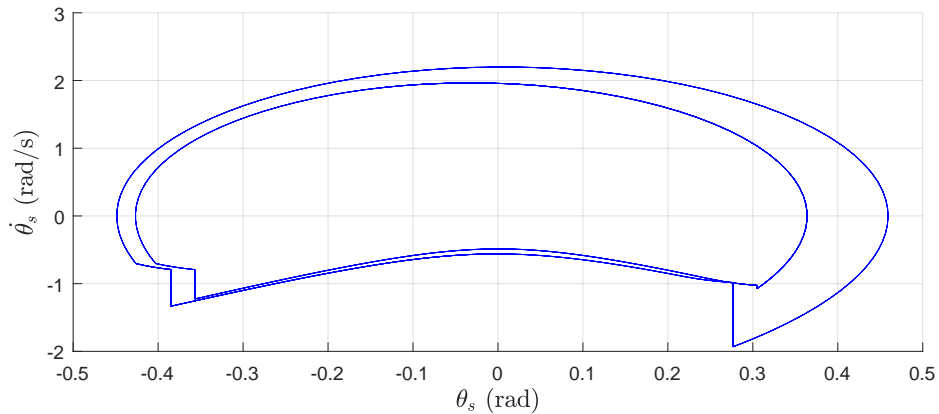
Figure 4.7: AACG trajectories of period-2 motion for downhill walking with model parameters $r_o = 0.034$N/m, $\phi = -0.04$ rad and initial conditions [-0.5608, -0.1402, 1.8894].

Let $p = (r_o, \phi)$ be given and $q_a \in \Gamma_i$ be such that $q_e = (p, q_a) \in \Gamma_i$, i.e. a fixed point of $\mathbf{G}_p^i$. Then, define the eigenvalues of the Jacobian $D\mathbf{G}_p^i$ at q_a as $\{\lambda_1, \ \lambda_2, \ \lambda_3\}$ where the maximum absolute eigenvalue is given as

$$\lambda_{max}(D\mathbf{G}_p^i) = max(|\lambda_1|, \ |\lambda_2|, \ |\lambda_3|). \tag{4.7}$$

Then, define the stable fixed point set as

$$\Gamma_i^s = \left\{ q_e = (p, q_a) \ | \ q_e \in \Gamma_i, \lambda_{max}(D\mathbf{G}_p^i) < 1 \right\}. \tag{4.8}$$

54
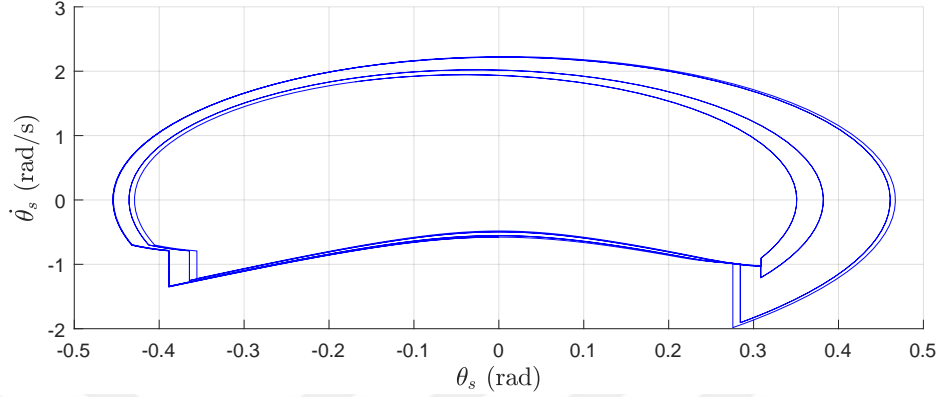
Figure 4.8: AACG trajectories of period-4 motion for downhill walking with model parameters $r_o = 0.0365$N/m, $\phi = -0.04$ rad and initial conditions [-0.5773, -0.1690, 1.8352].
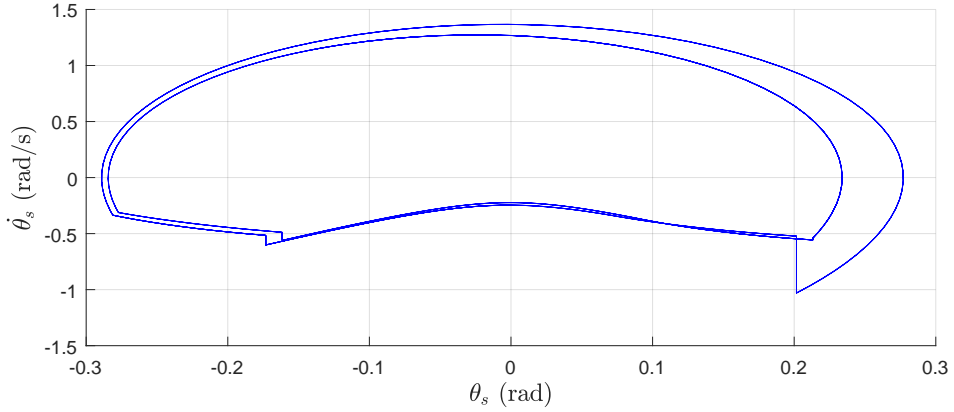
Figure 4.9: AACG trajectories of period-2 motion for uphill walking with model parameters $r_o = 0.4425$N/m, $\phi = 0.02$ rad and initial conditions [-0.2462, -0.1417, 1.1373].

We assume that for a given p, if $(p, q_a) \in \Gamma_i^s$, then q_a is unique. Hence, under this assumption, if $q_e \in \Gamma_i^s$, we can write q_a as a function of p. Since we do not have an analytical expression for the apex return map $\mathbf{G}_p$, the exact mathematical proof of this assumption is quite difficult due to highly nonlinear nature of the problem. It should be noted that during our extensive simulations we did not encounter a counterexample to this assumption. We further define the set S_i^s as

$$S_i^s = \{p \mid \exists\, q_a, \{p, q_a\} \in \Gamma_i^s\}. \tag{4.9}$$
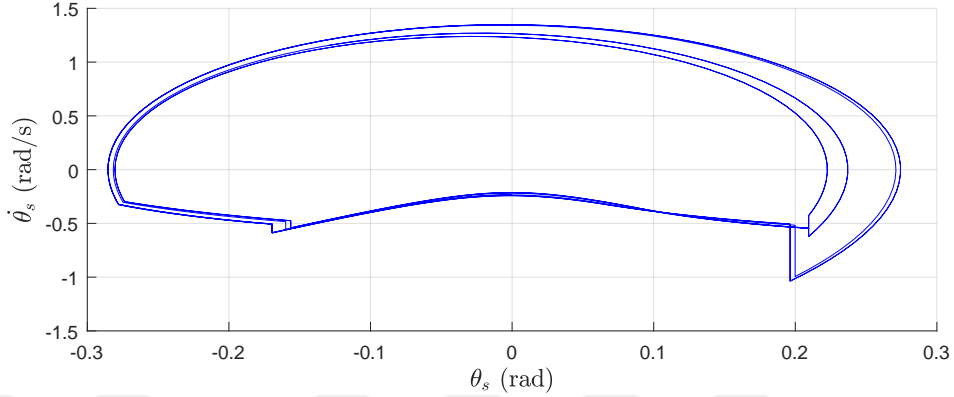
Figure 4.10: AACG trajectories of period-4 motion for uphill walking with model parameters $r_o = 0.0435 \text{N/m}$, $\phi = 0.02$ rad and initial conditions [-0.2353, -0.1298, 1.1548].

Hence, S_i^s is the projection of Γ_i^s on (r_o, ϕ) plane and it is depicted on Fig. 4.11 for $i = 1, 2, 4, 8$. The region in green depicts stable period-1 gaits and note that the range of precompression values that our model can walk is quite large. The blue, purple and grey regions depict period-2, period-4, period-8 walking patterns respectively. In addition to S_i^s, the regions in red represents the walking patterns in chaotic form.

The map given in Fig. 4.11 provides information about choosing the amount of spring precompression, i.e., the amount of energy to be injected to the body, for walking over a given sloped ground. The model is capable of walking on downhill slopes up to -3.9^o and on uphill slopes up to 4.45^o. Walking behaviour is sustained for precompression value up to 0.425 m. In [42], during level ground walking we had observed stable walking gaits of period-1 upto period-32 as well as chaotic walking patterns and finally unstable walking behaviour, respectively as we increase spring precompression. Note that, this corresponds to the $\phi = 0$ line in Fig. 4.11, where the period doubling bifurcation scheme is illustrated in Fig. 3.10. Furthermore, we had observed the recovery of walking patterns starting from sustained but non-periodic chaotic gaits up to period-1 walking if the spring precompression is further increased. Hence, a gap is formed between these two walking patterns. Fig. 4.11 demonstrates that this, no stable region, gap can be reduced for some ground slope and spring precompression pairs enabling the
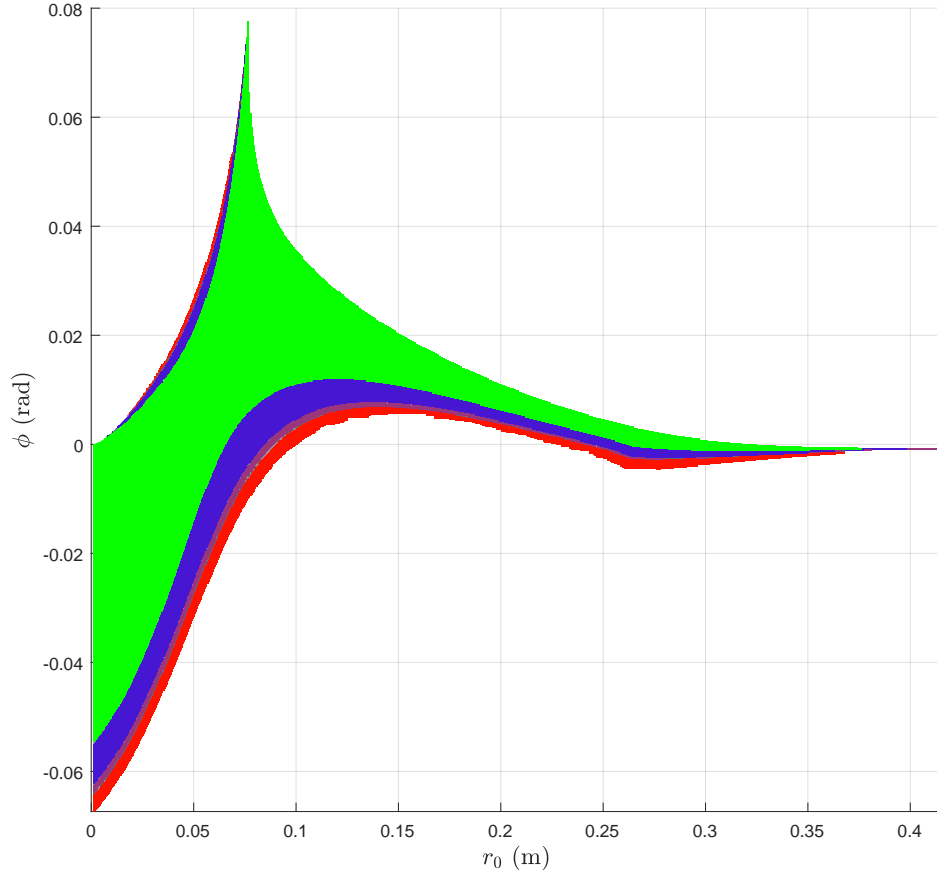
Figure 4.11: The figure depicts the dependence of fixed points of the AACG model on the spring precompression r_0 and ground slope ϕ.

model walk for a broad range of precompression values without falling. It is also interesting to note that the period-doubling bifurcations in Fig. 4.11 does not only occur for a single direction of spring precompression parameter or ground slope parameter but instead it occurs for different combinations (direction) of parameter pairs.

We, then obtain the maximum absolute value of the eigenvalues of the period-1 walking region by using $\lambda_{max}(D\mathbf{G}_p^1)$ as depicted in Fig. 4.12. The color bar on the right of the figure represents the values of the eigenvalues from 1 (least stable) to 0 (most stable). It is clear from the figure that the model becomes less stable at the boundaries and it is more stable at the middle fixed points. The
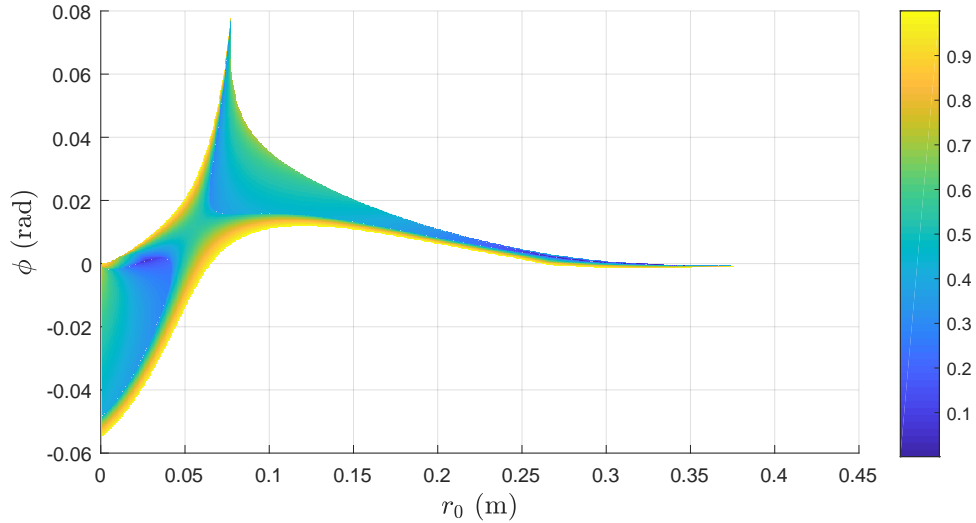
Figure 4.12: The figure depicts the maximum absolute value of the eigenvalues of period-1 fixed points of the AACG model.

map of Fig. 4.12 is utilized in controller design for rough terrain walking in the next section.

Stance leg velocity at the instant of apex for period-1 fixed point gaits for $p \in \Gamma_i^s$ is given as

$$\dot{\theta}_a(p) = \pi_1(q_a(p)), \tag{4.10}$$

which is the first component of $q_a(p)$ and can be depicted on (r_p, ϕ) plane as in Fig. 4.13. Stance leg velocity map is intended to be used controller design purposes for velocity feedback on ankle spring precompression over rough terrains. Note that, the model walks faster on steeper downhill slopes and for large precompression values.

Furthermore, we obtain the amount of maximum leg retraction during the swing phase for period-1 fixed point gaits as in Fig. 4.14. This map can be used for building real-world platforms which is intended for walking over inclined surfaces. The retraction values for downhill slope are the amount of foot scuffing which is ignored during simulations.
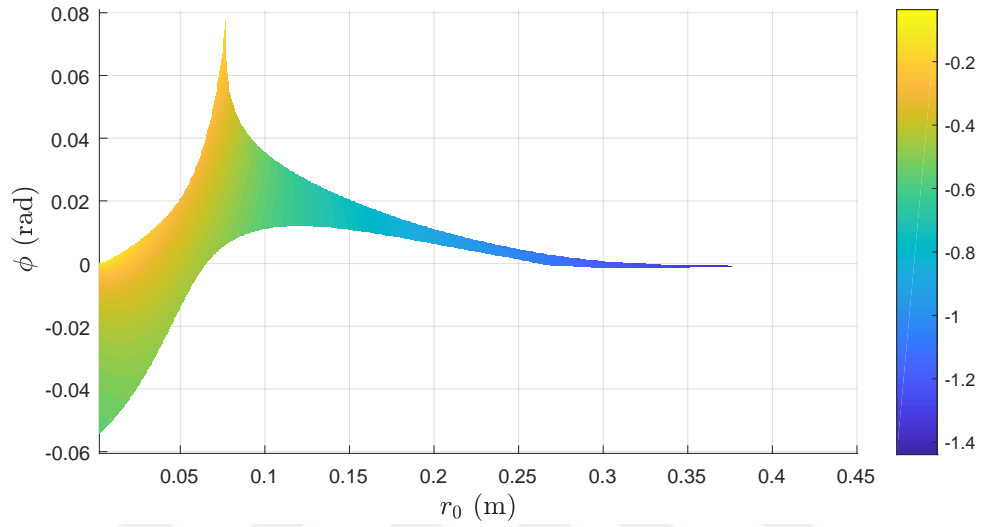
Figure 4.13: Stance leg velocity at the instant of apex of stable period-1 gaits during swing phase.
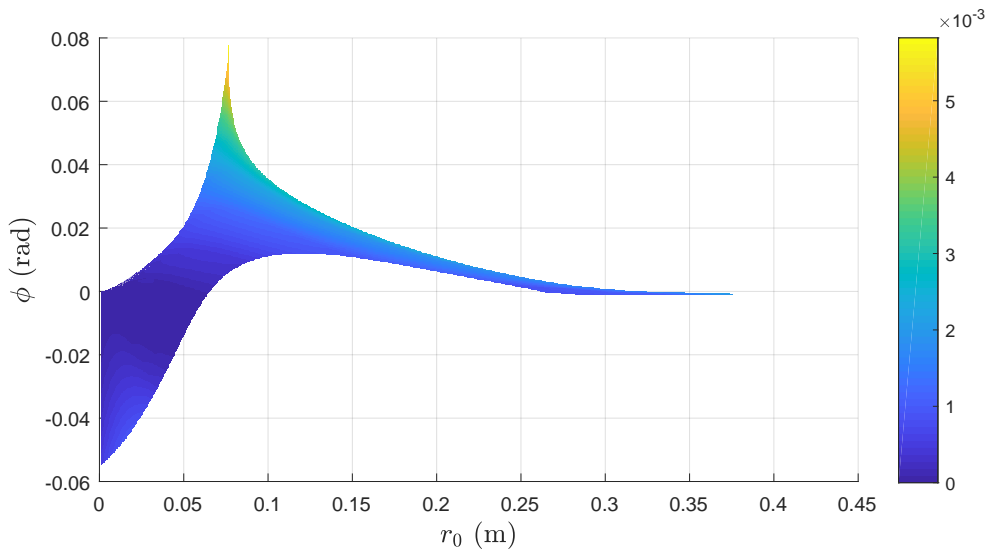
Figure 4.14: The amount of maximum leg retraction of stable period-1 gaits during swing phase.

Chapter 5

Walking over Rough Terrains with the AACG Model

In this chapter, we first generate rough terrain by adding small ground segments where the angle difference between segments are randomly chosen. Then, we evaluate the model over rough terrains and assess the performance for various ankle spring precompression controllers. We utilized the maps obtained in the previous section for controller designs.

5.1 Rough Terrain Walking via Ground Slope Feedback Control

A fixed choice of the spring precompression r_0 does not always yield a stable limit cycle for walking over the entire range of slopes with the AACG model. It is, however, encouraging to note that sustained walking patterns exist for considerable large range of precompression parameter, covering a wide range of forward velocities, which is directly related to the stance leg velocity $\dot{\theta}_s$ at apex. The capabilities of the proposed model is further explored by evaluating the performance of the model on rough terrains. The terrain is formed by merging

small ground segments where the angle differences between ground segments are chosen randomly. These angles are picked from truncated Gaussian distribution where the probability distribution function (PDF) of the distribution is given as for a given angle difference $d\phi^*$

$$\psi(\mu, \sigma^2, -R_{tr}, R_{tr}, d\phi^*) = \begin{cases} 0, & d\phi^* \leq R_{tr}, \\ \frac{P(\mu, \sigma, d\phi^*)}{F(\mu, \sigma^2, -R_{tr}) - P(\mu, \sigma, R_{tr})}, & -R_{tr} < d\phi^* < R_{tr} \\ 0, & -R_{tr} \leq d\phi^* \end{cases}$$

(5.1)

Here, μ and σ represent the mean and variance of the normal PDF respectively. The symmetrical truncation range $-R_{tr}, R_{tr}$ is given as $-\infty < R_{tr} < \infty$. F and P are the cumulative distribution function (CDF) and PDF of the normal distribution, respectively. Given the symmetrical truncations range (R_{tr}) of Gaussian distribution we choose 100 $d\phi^*$ values randomly within the truncation range. Then, we form the terrain by merging 101 ground segments of length 1m with 100 $d\phi^*$ values. Composed of small ground segments, the roughness measure of the terrain can be configured by adjusting truncations range where $d\phi^*$ is chosen. The roughness of the ground can be varied from level ground, $R_{tr} = 0$ (rad), to increasingly rough terrain until the truncation range $R_{tr} = 0.02$ (rad). We use R_{tr} parameter as a performance measure of walking on rough terrains throughout the thesis.

Now, let ϕ_{min} and ϕ_{max} be given as

$$\phi_{min} = min(\{\phi \mid p \in \Gamma_1^s\}),$$

(5.2)

$$\phi_{max} = max(\{\phi \mid p \in \Gamma_1^s\}).$$

(5.3)

Consider the following set for a given $\phi^* \in [\phi_{min}, \phi_{max}]$

$$S_c^s(\phi^*) = \{p \mid p \in S_1^s, \phi = \phi^*, r_o < r_{limit}\}),$$

(5.4)

where $r_{limit} = (r_o, \phi_{max}) \in \Gamma_1^s$ and r_{limit} is assumed to be unique and $r_{limit} =$ 0.0765 m. Furthermore, we assume that $S_c^s(\phi^*)$ is a connected set for every ϕ^*. For a given $\phi^* \in [\phi_{min}, \phi_{max}]$, we define the following functions,

$$r_o^{min}(\phi^*) = \min_{r_o}((r_o, \phi^*) \in S_c^s(\phi^*)), \tag{5.5}$$

$$r_o^{max}(\phi^*) = \max_{r_o}((r_o, \phi^*) \in S_c^s(\phi^*)). \tag{5.6}$$

The definitions given between (5.2) and (5.6) are illustrated in Fig. 5.1.
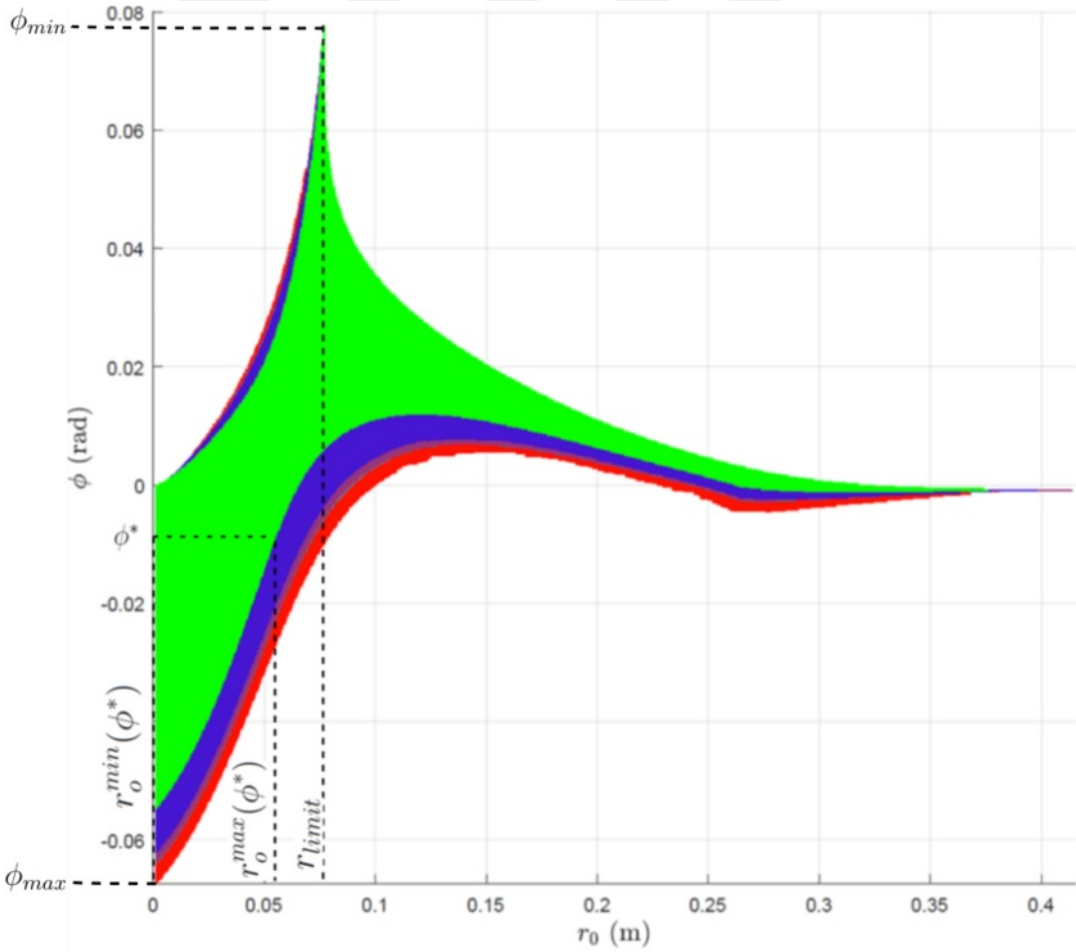
Figure 5.1: Definitions are depicted on fixed point figure.

Now, we can define the following functions which determines the precompression value for a given slope ϕ^*,

$$r_o^{mid}(\phi^*) = (r_o^{min}(\phi^*) + r_o^{max}(\phi^*))/2, \tag{5.7}$$

$$r_o^{mineig}(\phi^*) = \operatorname*{argmin}_{r_o}(\lambda_{max}(D\mathbf{G}_p^1) \mid (r_o, \phi^*, q_a) \in S_c^s(\phi^*)). \tag{5.8}$$

Fig. 5.2 depicts $r_o^{mid}(\phi^*)$ and $r_o^{mineig}(\phi^*)$ for $\phi^* \in [\phi_{min}, \phi_{max}]$. The curve in red color represents the middle precompression values obtained by averaging the precompression for any given slope cross-section where the curve in blue corresponds to the minimum eigenvalues of the containing slope cross-section.
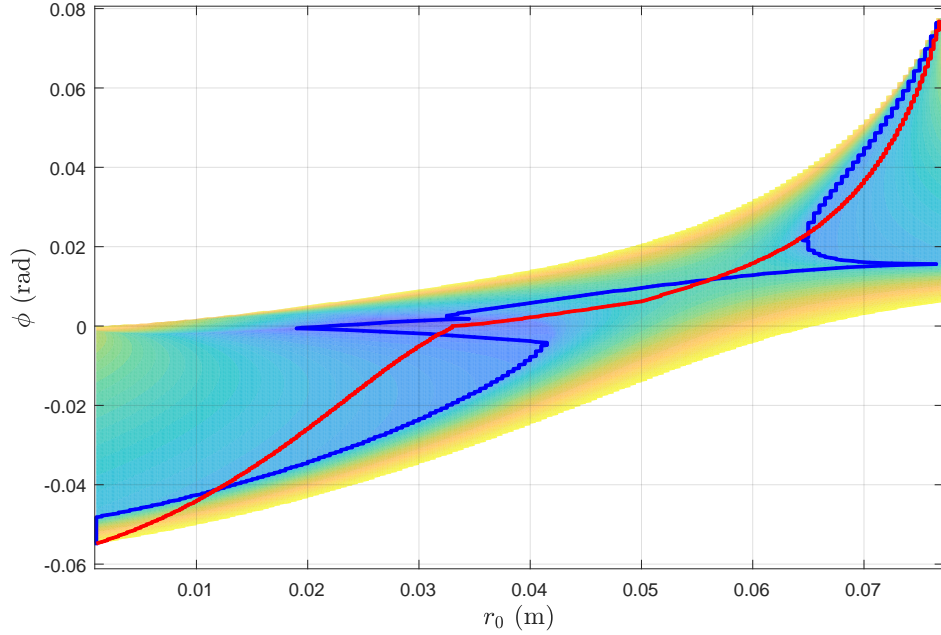
Figure 5.2: The blue and red curves represents minimum eigenvalue and midvalue spring precompression values, respectively.

Let x_{toe} and y_{toe} represent the components of p_{toe}. Then, the measured slope at the instant of collision is

$$\phi(x_{toe}(t_c[k])) = \tan^{-1}(\frac{y_{toe}}{x_{toe}}), \tag{5.9}$$

where $k = 0, 1, 2, ..., m$. are the discrete time indices at ground collision instants and for clarity let $\phi_c[k] = \phi(x_{toe}(t_c[k]))$.

In order to achieve walking over the rough terrain we exploit various ground slope feedback controller on the ankle spring extension. In this respect, the first control law chooses the middle value spring precompression for the given slope cross section, i.e., utilizes the red curve given in Fig. 5.2, as follows,

$$r_o[k] = r_o^{mid}(\phi_c[k]). \tag{5.10}$$

The second control law chooses the precompression value that has the minimum eigenvalue for the given slope cross section, i.e., utilizes the blue curve given in Fig. 5.2, as follows,

$$r_o[k] = r_o^{mineig}(\phi_c[k]). \tag{5.11}$$

To evaluate the performance of the AACG model on rough terrains, first we generate a terrain composed of small segments where the first segment is chosen to be level ground. The roughness of the terrain can be varied by adjusting the relative angles of the remaining segments. We start with the terrain roughness of $R_{tr} = 0$, i.e., level ground. After generating the ground, we evaluate our model on the corresponding ground starting from apex state ($\theta_s = 0$ and $\dot{\theta}_n > 0$) on 18 different positions which are linearly spaced between initial position (0m) and mean stride length for level ground walking (0.43)m in order to observe the walking performance of the model for different initial conditions. We define two different performance measures. The first one is "Perfect Walk" where the model achieves 100 successful steps for all 18 different positions on a given terrain. The second performance measure is "Successive Steps" which is the ratio of number of successful steps over number of expected steps. The performance of the model is evaluated for 100 different grounds for a given roughness and the results are normalized for the corresponding roughness. Consequently, we iterate the above

performance measurement process for $R_{tr} = 0$ until $R_{tr} = 0.02$ with various ankle spring controllers.
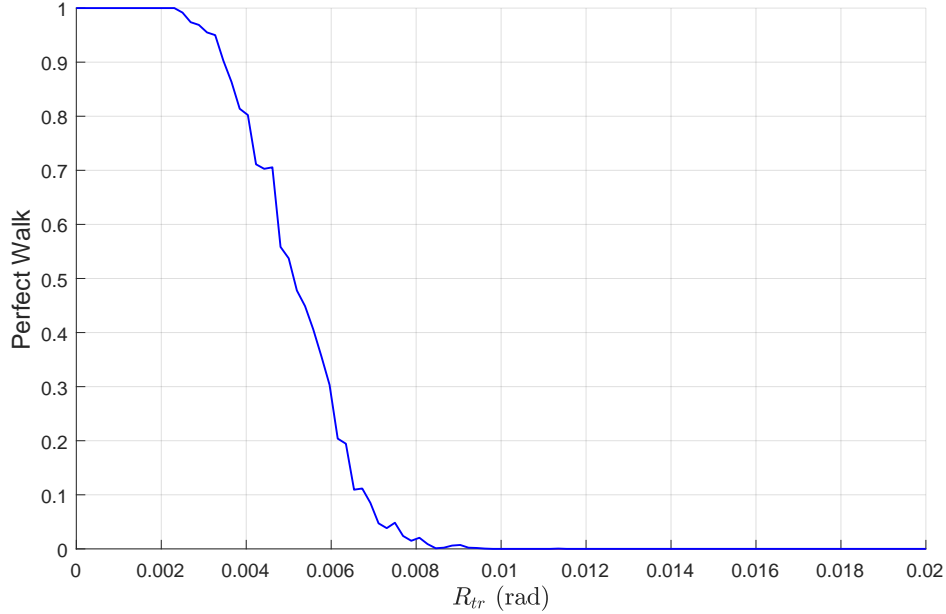
Figure 5.3: Perfect Walk performance measurement for fixed choice of spring precompression.

We exploit various controllers on our model over the terrains which have increasing amount of roughness. The first controller is chosen to be a fixed precompression value of 0.05m since the vertical cross section corresponding to $r_o = 0.05$m mostly covers the fixed points for uphill and downhill slopes. The performance measures of Perfect Walk and Successive Steps are given in Fig. 5.3 and Fig. 5.4, respectively. The fixed precompression controller performs well over the grounds having low roughness and both Perfect Walk and Successive Step measures decrease drastically beyond the terrain roughness range of 0.002 rad.

The second controller measures the ground slope and use this slope as a feedback to choose an appropriate precompression r_0 value at each step utilizing the spring precompression value having the minimum eigenvalue, which is given by the control law in (5.11). Once the precompression value is chosen the corresponding spring is released during double support phase. The performance measures of Perfect Walk and Successive Steps are given in Fig. 5.5 and Fig. 5.6, respectively.

65
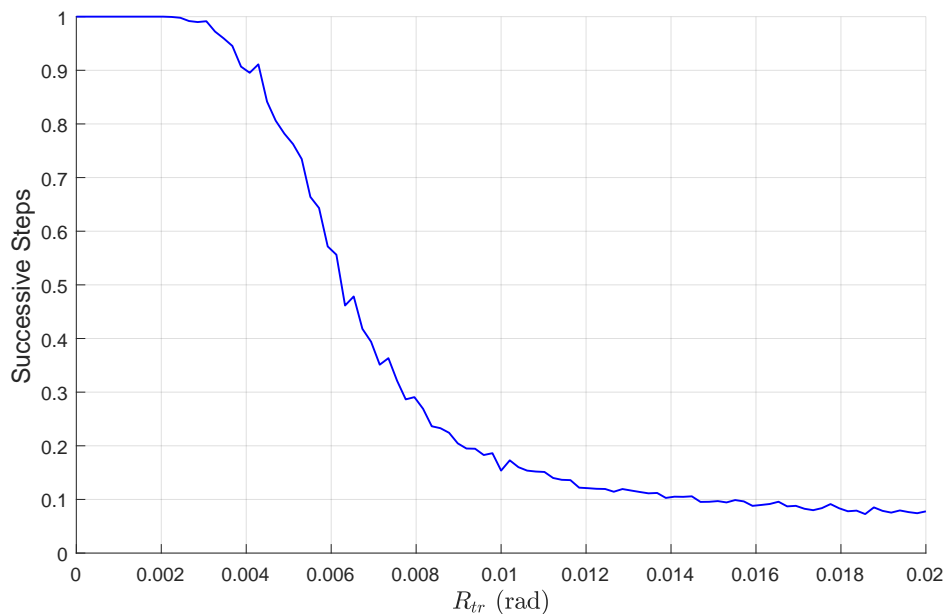
Figure 5.4: Successive Steps performance measurement for fixed choice of spring precompression.

The line in red represent the results where the controller measures the ground slope of the segment that contains stance toe and the results in red represent the controller measuring the ground slope at the instance of collision. The controller has a weak performance for both ground measurement results. One possible explanation for such result is that the controller chooses the precompression values that are quite close to the boundaries in the map of Fig. 5.2 which may destabilize the model.
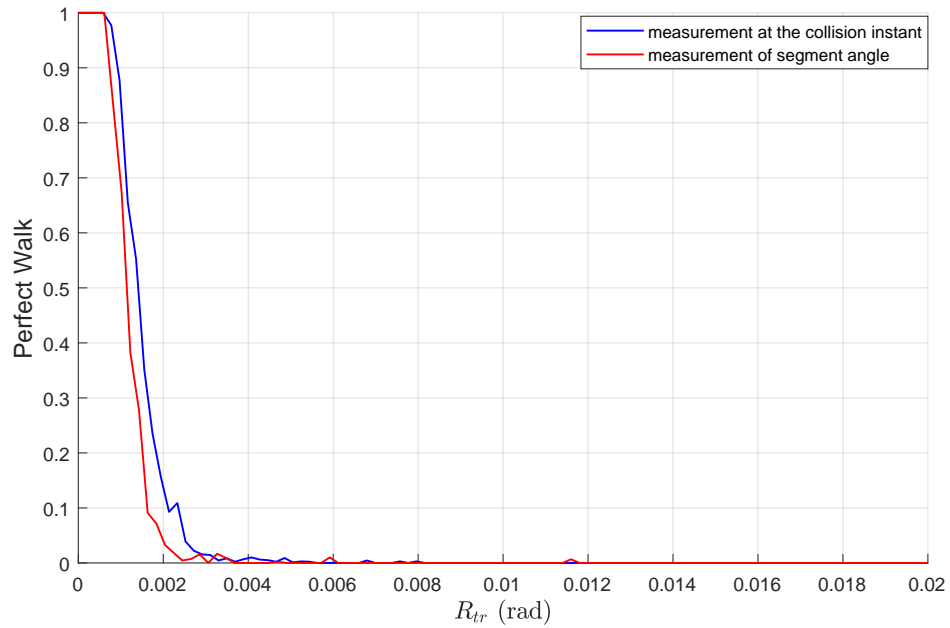
Figure 5.5: Perfect Walk performance measurement for ground slope feedback controller with spring precompression value having the minimum eigenvalue.
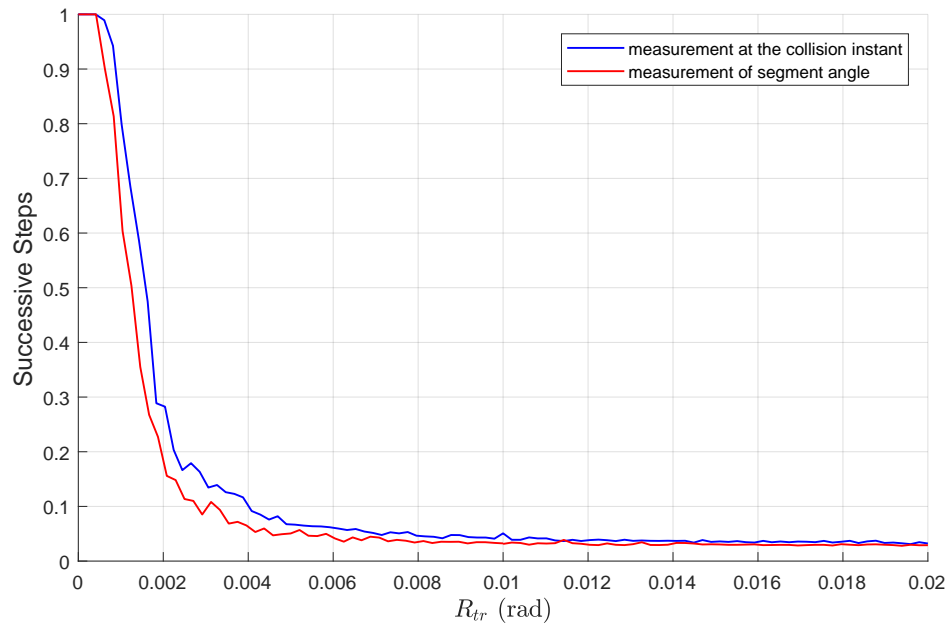
Figure 5.6: Successive Steps performance measurement for ground slope feedback controller with spring precompression value having the minimum eigenvalue.

The third controller utilizes the ground slope measurement as a feedback into the ankle spring precompression by making use of the middle value spring precompression, which is given by the control law in (5.10). The performance measures of Perfect Walk and Successive Steps are given in Fig. 5.7 and Fig. 5.8, respectively. The line in red represents the results where the controller measures the ground slope of the segment that contains stance toe and the results in red represent the controller measuring the ground slope at the instance of collision. The results obtained using the ground slope measured at the instant of collision outperform the results obtained using the ground slope of the segment that contains stance toe since the measurement at the collision provides more precise information about the ground slope.
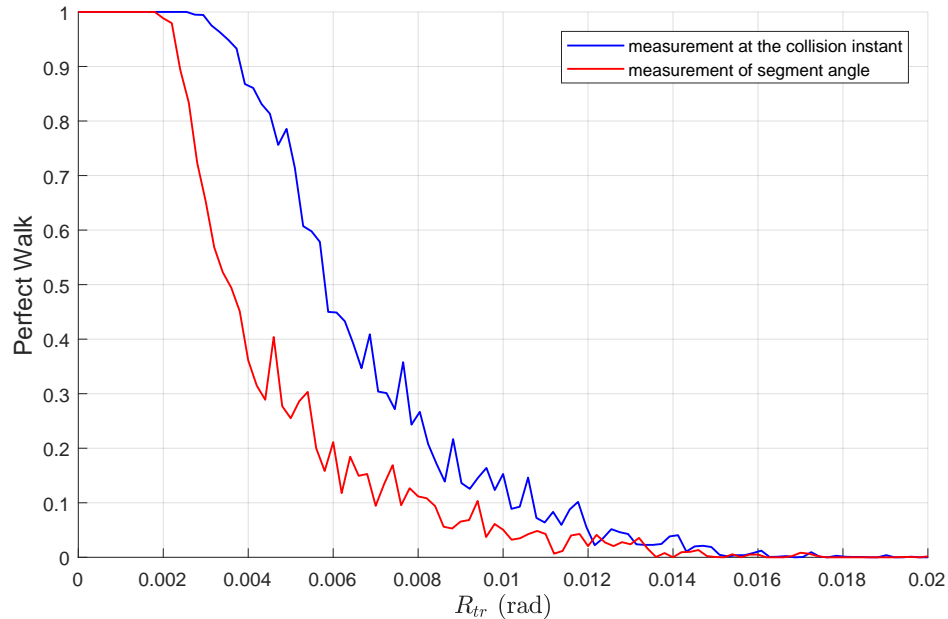
Figure 5.7: Perfect Walk performance measurement for ground slope feedback controller with middle value spring precompression.

For all controllers as the slope difference between two consecutive ground segment increases the success rate of perfect walk decreases. Yet, the best performance is obtained with the middle value precompression controller since the controller utilizes the width of the map given in Fig. 4.11, i.e. it avoids the precompression values which are close to the boundaries.
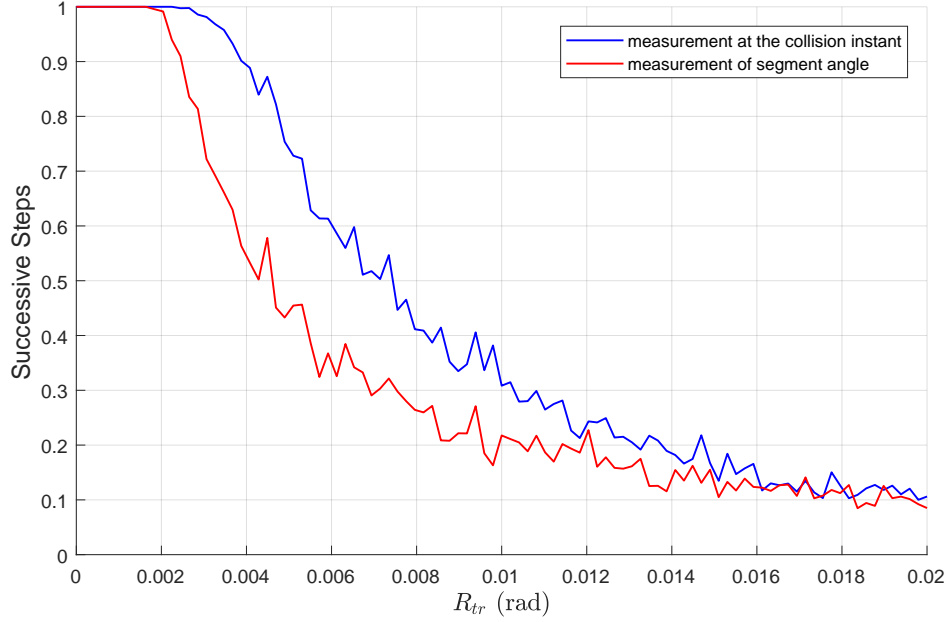
Figure 5.8: Successive Steps performance measurement for ground slope feedback controller with middle value spring precompression.

5.2 Rough Terrain Walking via Velocity Feedback along with Ground Slope Feedback Control

In order to enhance the performance of the model over the rough terrains, we utilize a stance leg forward velocity feedback control along with the ground slope feedback on the ankle precompression. Let q_c^k be the model configuration at the kth ground collision and q_{pc}^{k+1} represent the predicted model configuration of the next ground collision which is assumed to have a constant stride length d_m. Here, d_m is obtained for level ground with $r_o^{mid}(0)$ precompression. Then, let $\phi_c^*[k]$ and $\phi_{pc}^*[k+1]$ represent the ground slopes of the model configurations q_c^k and q_{pc}^{k+1} at the collision indices k and $k+1$ respectively. Consequently, we define the following

$$r_o^{nom} = r_o^{mid}(\phi_{pc}^*[k+1]). \tag{5.12}$$

As a consequence, the velocity feedback controller on the ankle spring is given as follows by utilizing r_o^{nom}, $\phi_{pc}^*[k+1]$ and $\dot{\theta}_a$ map,

$$r_o[k] = r_o^{nom} - k_p(\dot{\theta}_a(r_o^{nom}, \phi_{pc}^*[k+1]) - \dot{\theta}_a^m). \tag{5.13}$$

Here, k_p is the velocity feedback gain and $\dot{\theta}_a^m$ is the measured stance leg velocity at the apex instance. The velocity feedback controller utilizes the velocity map in Fig. 4.13 to predict the desired stance leg velocity of the next apex assuming the next stride length to be d_m. Applying the relation in (5.13) the stance leg velocity and the ground slope information is fed to the ankle spring extension. Hence, the resultant controller enhances the walking performance of our model as the ground roughness increases as seen in Fig. 5.9 and Fig. 5.10.
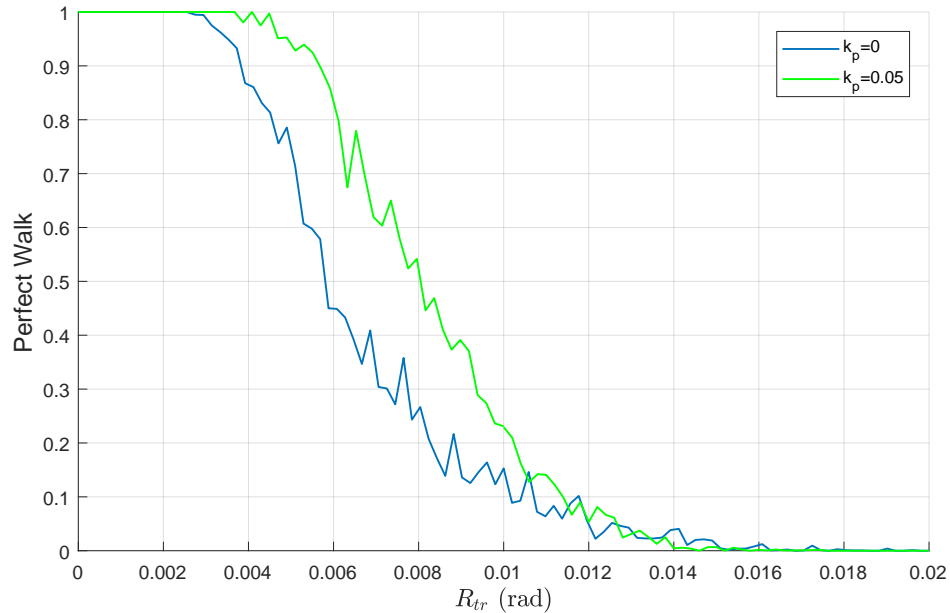
Figure 5.9: Perfect Walk Performance Measurement for ground slope feedback along with stance leg velocity feedback for middle value spring precompression controller .
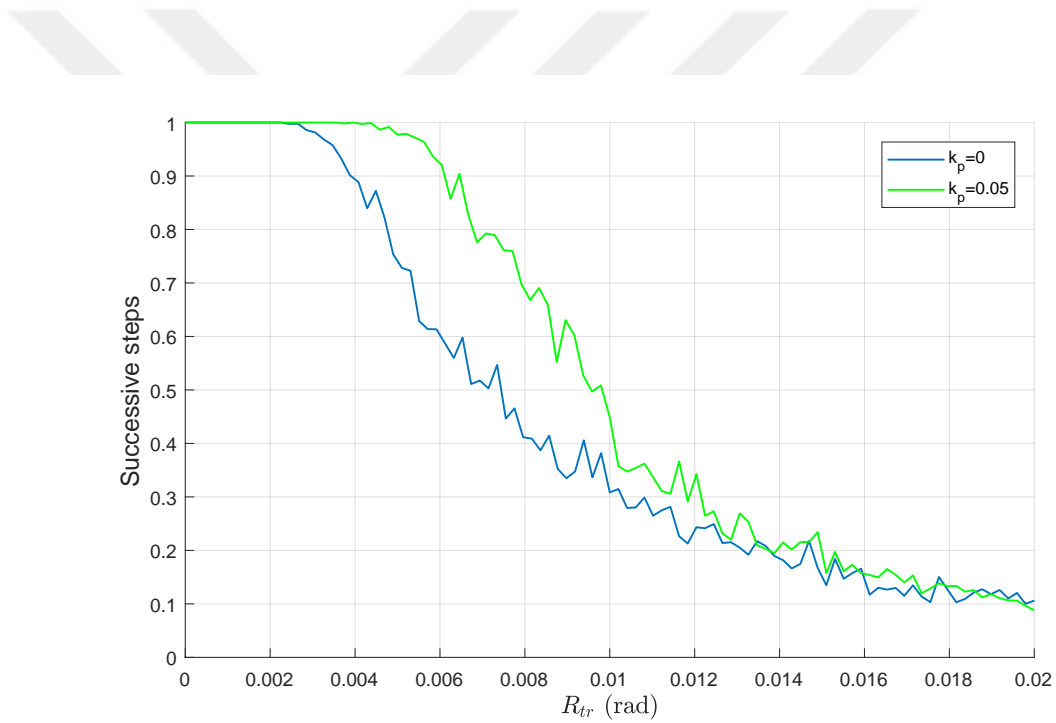
Figure 5.10: Successive Steps Performance Measurement for ground slope feedback along with stance leg velocity feedback for middle value spring precompression controller

Chapter 6

Active Ankle Foot Orthosis Platform

In this chapter, we first review several active ankle foot orthosis and prosthesis platforms in the literature. Then, we present the active ankle foot orthosis platform that we have developed which is motivated by the idea of verifying our stability results and controllers on an actual setup. The experiments indicate that the platform can assist the user during walking. Afterwards, we integrate our platform with an active knee orthosis platform helping the user with knee locking and leg swinging. The test results suggest that the integrated system can support the user and generate natural walking patterns.

Most people with disabled lower extremities are limited to conventional wheelchairs, restricting their mobility to only flat surfaces. Powered robotic orthoses promise to eliminate this limitation by enabling disabled people to ambulate naturally through the use of their lower extremities. Studies on powered robotic orthoses are mainly focused on gait phase detection, gait pattern generation, intention detection, actuation technologies, utilization of active and passive mechanical elements and control methods with the intention of replacing the functions of the knee and hip joints [46, 47, 48]. However, the ankle joint plays key roles for the energetics and stability of human walking. Consequently, the lack

of actuated ankle joints in robotic orthoses limits their energetic efficiency and results in unnatural walking patterns that might impair their utility and adoption. In addition to above observations it is stated in [49] that the ankle joint generates more torque compared to knee and hip joints.

We start by giving various definitions and phases which will be utilized in the rest of the chapter. Orthosis is an orthopedic appliance or apparatus used to support, align, prevent, or correct deformities or to improve function of movable parts of the body. Prosthesis is an artificial device used to replace a missing body part, such as a limb. Dorsiflexion is the movement of the foot upwards and plantarflexion is the movement of the foot downwards. The phases of walking is illustrated in Fig. 6.1. Heel strike, also known as initial contact, is a short period which begins the moment the foot touches the ground. Midstance is the period of foot becoming flat on the ground and during this phase, the body is supported by one single leg. Ankle push-off is the period when the ankle propels the body forward. Heel-off is the phase of heel leaving the ground. Swing phase is the gait cycle during which the foot is off the ground and stance phase is the gait cycle during which the feet are on the ground.

The impairment of ankle joint effects walking and yields unnatural and unhealthy gait schemes. The muscles controlling the ankle joint enables the joint to dorsiflex and plantarflex [50]. Drop foot is the inability to lift the front part of the foot. The two major complications of drop foot are slapping of the foot after heel strike (foot slap) and dragging of the toe during swing (toe drag). At heel strike, the uncontrolled foot falls to the ground, producing a distinctive slapping noise (foot slap). During mid-swing, toe dragging prevents proper limb advancement and increases the risk of tripping.

The basic functions of ankle joint are as follows.

- Shortly after heel strike phase, the ankle joint lifts the foot so that the foot does not hit the ground (slap foot),

- At the heel off phase it supplies the body with the energy required for
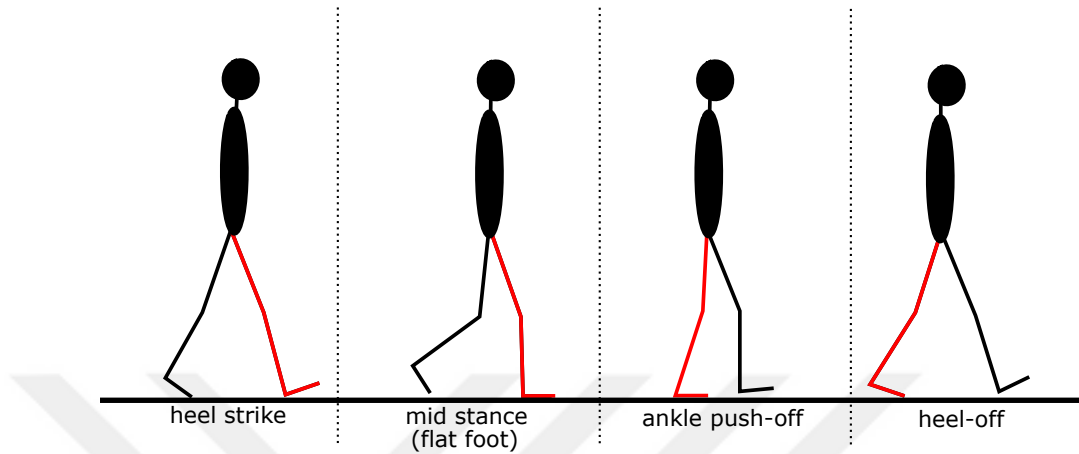
Figure 6.1: Phases of locomotion for a single stride.

walking,

- Ankle joint lifts the foot as the leg swings so that the foot does not collide with the ground.

There are several assistive devices for supporting or replacing the ankle joint as ankle foot orthosis, ankle foot prosthesis (AFP) [51, 52].

There are three different types of AFOs in the literature as follows.

- Standard AFOs are firm devices that are used to support or prevent undesired ankle motions,

- Passive AFOs can store and release energy with passive elements like linear spring but they can not provide energy input to the gait,

- Active AFOs can both store and provide energy to the gait with actuators.

The AFPs on the other hand are classified into two main types as follows.

- Passive AFPs, like passive AFOs, can store and release energy with passive elements like spring but they can not provide energy to the gait,

- Active AFPs are actuated systems that can provide energy input and they can also store and release energy.

The actuation scheme of the orthosis with series elastic actuation is illustrated in Fig. 6.2
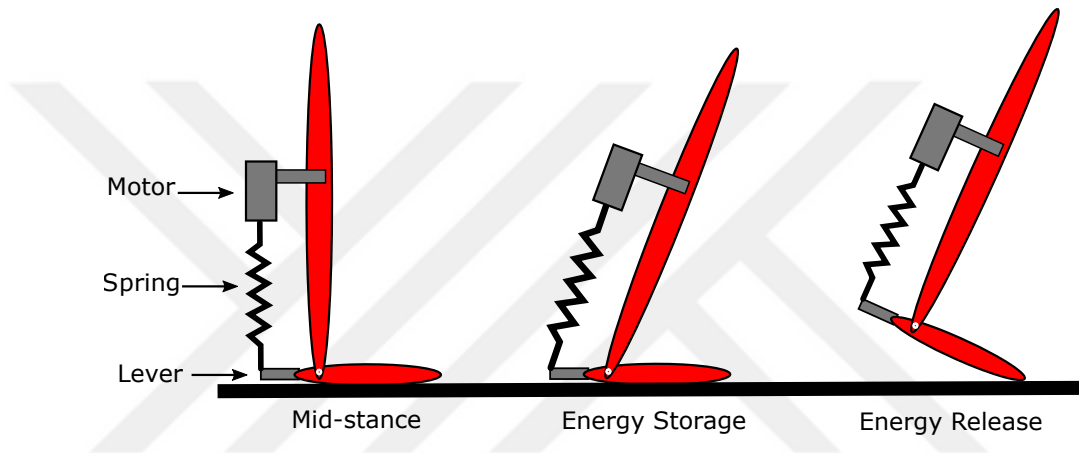
Figure 6.2: actuation scheme of the active orthosis.

At the instance of heel strike, the series elastic actuation mechanism prevents foot slapping. As the ankle rotates during mid-stance phase, the spring is extended both by walking kinematics and position controlled motor yielding assistive torque to be generated at the ankle for push-off. At the end of push-off phase, the foot is lifted up via the SEA in order to prevent drop foot.

The objective of active AFO (AAFO) design is the use of passive energy storage components in conjunction with actuators in the ankle joint, employing natural dynamics of walking. The ankle joint will be utilized to achieve energy efficiency compared to directly actuated ankle joint designs. Among important challenges in this context are the design of a SEA mechanism that is sufficiently strong while being as light as possible with appropriate passive dynamic properties to support natural walking.

As stated in [53], the ankle joint has a key role for walking in terms of torque generated during ankle push-off. For a 100 kg person the maximum peak torque

requirement during healthy walking gait is 150Nm. Given a lever arm of 10cm the motor-ballscrew complex should be able to provide 1500N of force. In order to provide 1500N of force, the maximum torque that should be generated by the motor is calculated using the relations in [54] as follows.

$$\tau = \frac{F * p}{2 * \pi * \eta},\tag{6.1}$$

where τ is the torque value that is the motor is required to generate, F is the linear force that motor applies, p is the pitch of ball screw and η is the efficiency of the ball screw. The required maximum motor torque is 0.65Nm for $F = 1500$Nm, $p = 2$mm and $\eta = 0.75$. In order to calculate the speed requirement of the motor we assume that the patient walks slower than the able-bodied person and the time required for a single stride is two seconds. As stated in [49], 20% of a single stride consist of push-off phase which makes 400ms of push-off time. For 5 cm spring extension, the maximum speed required for the motor is 5cm/0.4s = 0.12m/s. In this respect, Nanotec DB42C01 Brushless DC motor fulfills our speed, power, torque and mechanical demands. The ballscrew shaft is chosen to be of 10cm long with a pitch of 2mm and an efficient nut. The motor driver is chosen to be MAXON EPOS-2 motor controller which has hall sensor, encoder signal, analog/digital inputs and RS232, USB and CAN interfaces. The control of the AAFO is performed on 512 MHz RTD-PC/104 with 256MB DDR SDRAM, 1GB of Flash driver and various peripheral communication units such as RS232, RS485, CAN and Ethernet.

The springs are chosen with 10N/mm stiffness and 100mm length such that at maximum extension they can provide approximately 1500N of force for ankle push-off. The angular position of the ankle can be determined kinematically by measuring the amount of deflection in the spring length and utilizing the motor encoder data. Hence, we considered measuring the linear deflection of the spring with Opkon resistive linear position transducer. In order to determine the heel strike event we also utilize the linear deflection of the spring.

One of the aspects of building the AAFO platform is the integration of the

platform with an AKO system. In order to maintain the rigidity of the integration we decided to manufacture the AAFO system with aluminum (6061) material.

The AAFO mechanism consists of three main parts.

- Ankle-foot component. It acts as a shoe with a lever arm. This lever provides moment arm to assert controlled dorsiflexion and plantarflexion motion to the foot.

- Knee orthosis integration component.

- SEA mechanism. This component actuates the system. By correctly positioning the motor nut, a desired spring extension is obtained. The spring releases its stored energy to provide most of the peak power required during ankle push-off.

The mechanical design specifications of the AAFO system are as follows.

- The SEA mechanism with two identical springs are employed to obtain symmetric force on the lever arm.

- The length of the lever arm is designed to be 10cm.

- A guiding mechanism with bushing is designed in parallel with SEA in order to tolerate spring buckling effects.

- A stopper is placed at end of the ballscrew shaft to limit the motion of ballscrew nut.

- The length of the SEA mechanism can be adjusted.

The AAFO prototype is depicted in Fig. 6.3. The control of the prototype is achieved via the real time operating system QNX over RTD PC/104 microcontroller.
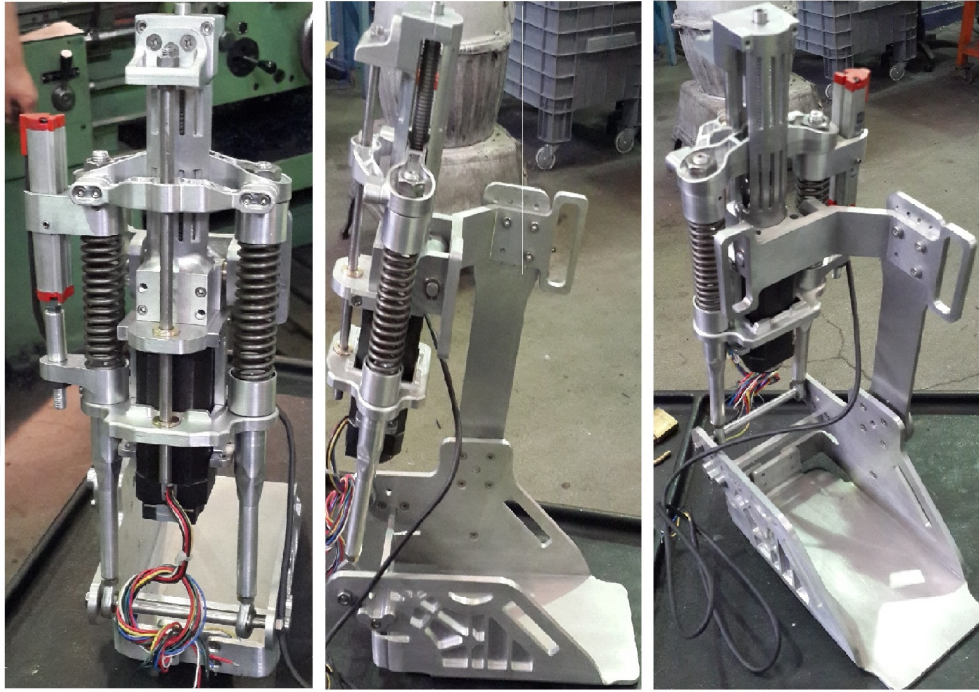
Figure 6.3: Active Ankle Foot Orthosis Platform.

6.1 AAFO Platform Tests

We built the experimentation setup shown in Fig. 6.4 where the tests are performed on a healthy individual.

The SEA mechanism enables us to control the angle of the ankle joint by controlling the position of the motor nut connected to one end of the spring as illustrated in Fig. 6.2. With the use of information obtained from linear potentiometer and motor encoder the platform can achieve the desired locomotion pattern. The state machine for the controller is depicted in the Fig. 6.5 and details are given as follows. The tests are performed with one AAFO on the left leg and initiated from swing phase. In the Heel Strike Detection state as the heel touches the ground, the position controller prevents slap foot by keeping the motor nut position stationary, hence compresses the spring. The amount

Figure 6.4: AAFO Experimentation Setup

of compression in the spring rest length is measured via the linear potentiometer. The heel collision is detected if the spring rest length is below a threshold value. During Mid-Stance Detection state the ankle rotates over the foot, spring starts to extend and once the spring length reaches to its neutral length we detect mid-stance instant. At this moment Spring Extension state begins and position controller starts extending one end of the spring that results in storing energy into the springs. The stored energy in the springs, i.e., the amount of spring extension, is injected into walking during ankle push-off via spring decompression. Once the spring decompresses into its natural length, injecting all the stored energy, we detect the end of ankle push-off phase in Toe Lift-off Detection state and finally in Foot Lift-off state the controller lifts of the foot to avoid drop foot and eventually swing phase starts. The state transition parameter values are chosen heuristically during experiments.

Fig. 6.6 depicts the heel strike and ankle push-off instances during the platform tests, respectively. Fig. 6.7 and Fig. 6.8 shows the motor nut position and the spring length measurement for three consecutive steps, respectively. In Fig. 6.7, the motor extends the spring for 12 mm during Spring Extension state and lifts
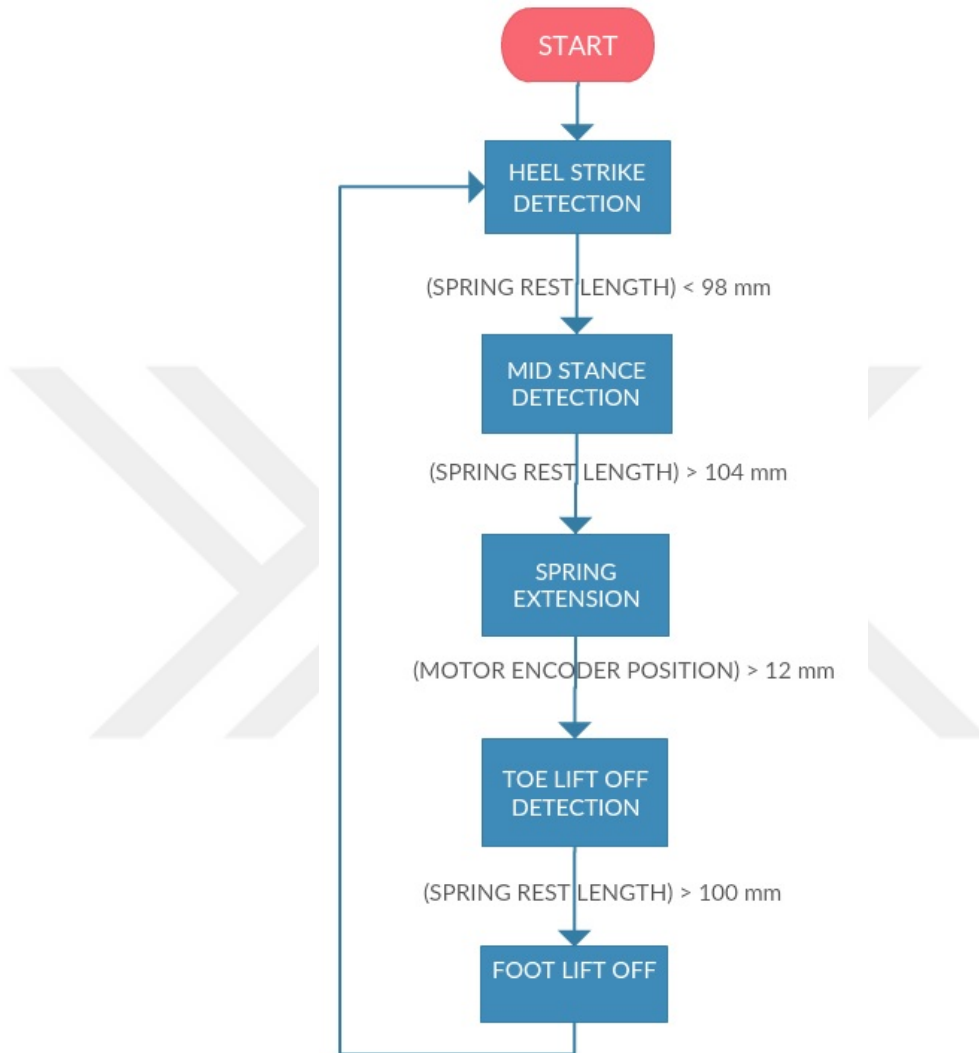
Figure 6.5: AAFO Control State Machine.

the foot up during Foot Lift-off state. In Fig. 6.8 heel strike is detected as the spring length decreases beyond 98 mm. Once the spring starts extending and reaches to 104 mm mid-stance phase is detected. Finally, toe lift-off event is detected when the spring length becomes 100 mm. During ankle roll-over the maximum amount of spring extension is observed to be 15 mm, which generates an approximate of 30 Nm of torque at the ankle during push-off. This torque corresponds to 20% of the torque required during ankle push-off, hence it helps propelling the body forward while decreasing energy loss due to ground collision.

(a) Heel Strike Phase. (b) Ankle Push-off Phase.

Figure 6.6: Walking Phases of the AAFO Test.
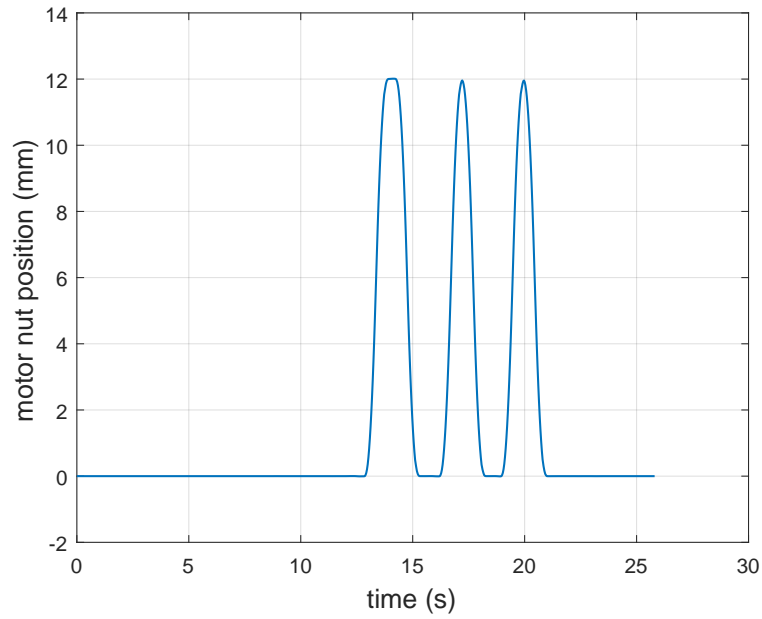
Figure 6.7: AAFO Motor nut position during the experiment.
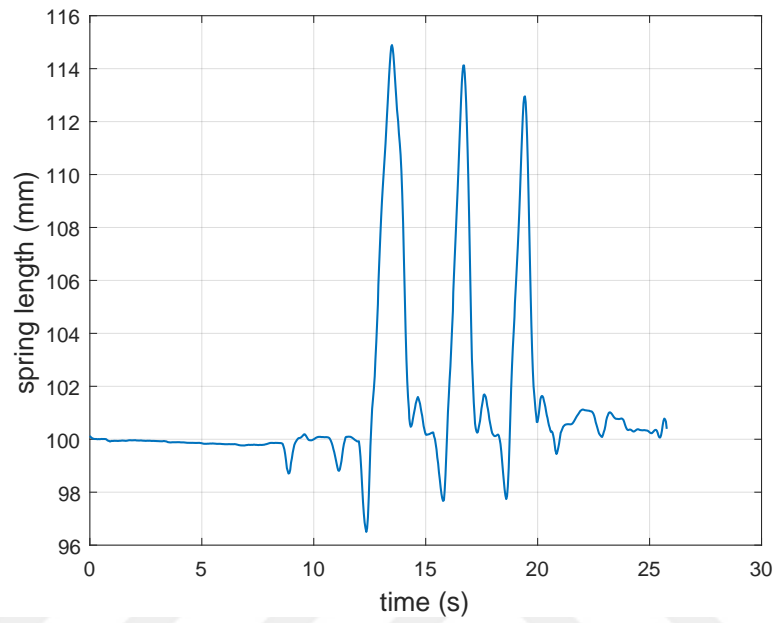
Figure 6.8: AAFO Motor spring length measurement during the experiment.

6.2 AAFO and AKAFO Integration Tests

Another important motivation aspect of realizing the AAFO platform is the integration of the platform with a lower body robotic orthosis. In this respect, the AAFO platform is integrated with the AKO platform on the leg, excluding hip joints. The AKO platform is designed for the patients whose knee does not lock during stance phase and for those who can not perform an effective leg swing.

Figure 6.9: Active Knee Orthosis

As can be seen in Fig. 6.9 the AKO locks the knee joint during stance phase and helps the patient to perform a well defined leg swinging with the help of a Maxon RE45 brushless rotary motor. The integration of AAFO with AKO is achieved as shown in Fig. 6.10. The control of the AAFO-AKO integration prototype is achieved via RTD/104 microcontroller and EPOS2 motor driver over QNX environment.
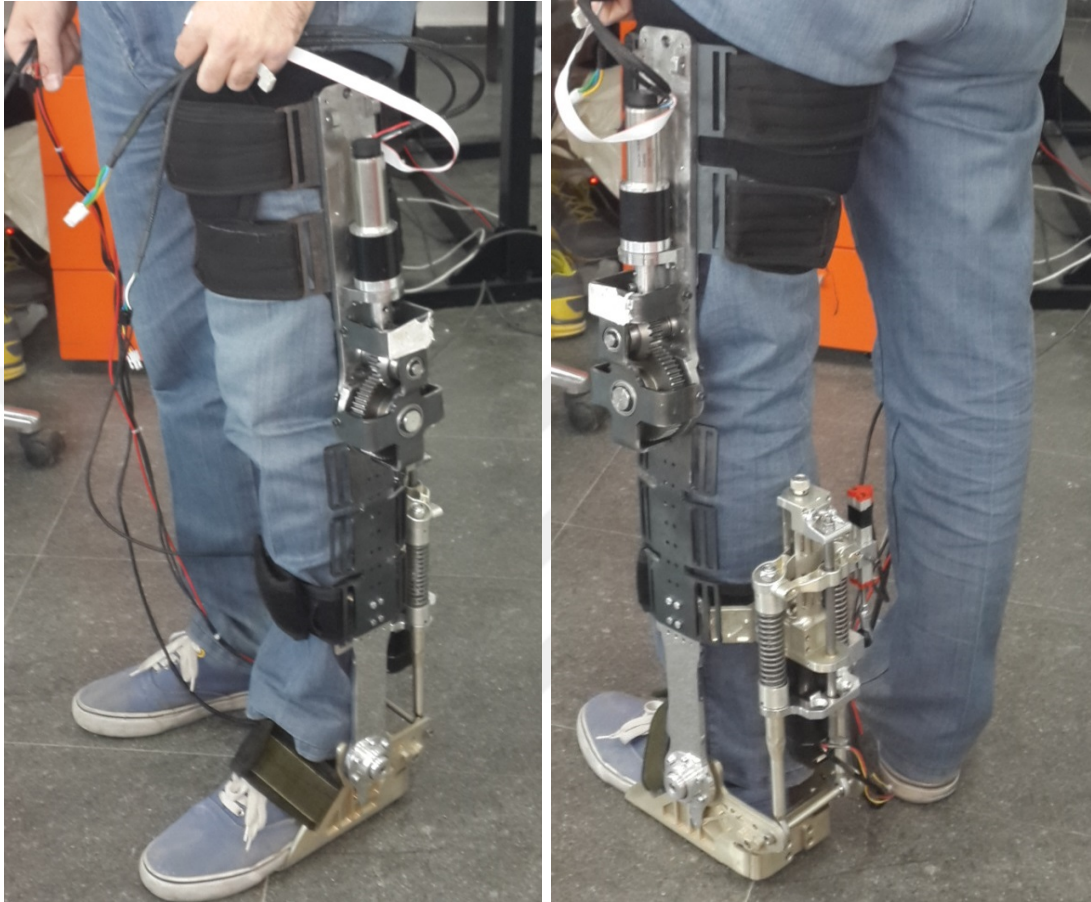
Figure 6.10: AAFO-AKO Integration.

The control state machine of AAFO-AKO integration is extended to include the knee flexion and extension as shown in the Fig. 6.11. After lifting up the foot, algorithm flexes the knee joint in Knee Flexion state to avoid toe dragging. Once the knee flexion reaches up to 40°, the controller starts extending the knee with Knee Extension state helping the user to perform an effective leg swing for the preparation of the next heel strike.

Fig. 6.12 depicts the heel strike, ankle push-off and knee flexion instances during the tests, respectively.

Fig. 6.13, Fig. 6.14 and Fig. 6.15 shows the AAFO motor nut position, the spring length measurement and AKO motor angle for three consecutive steps
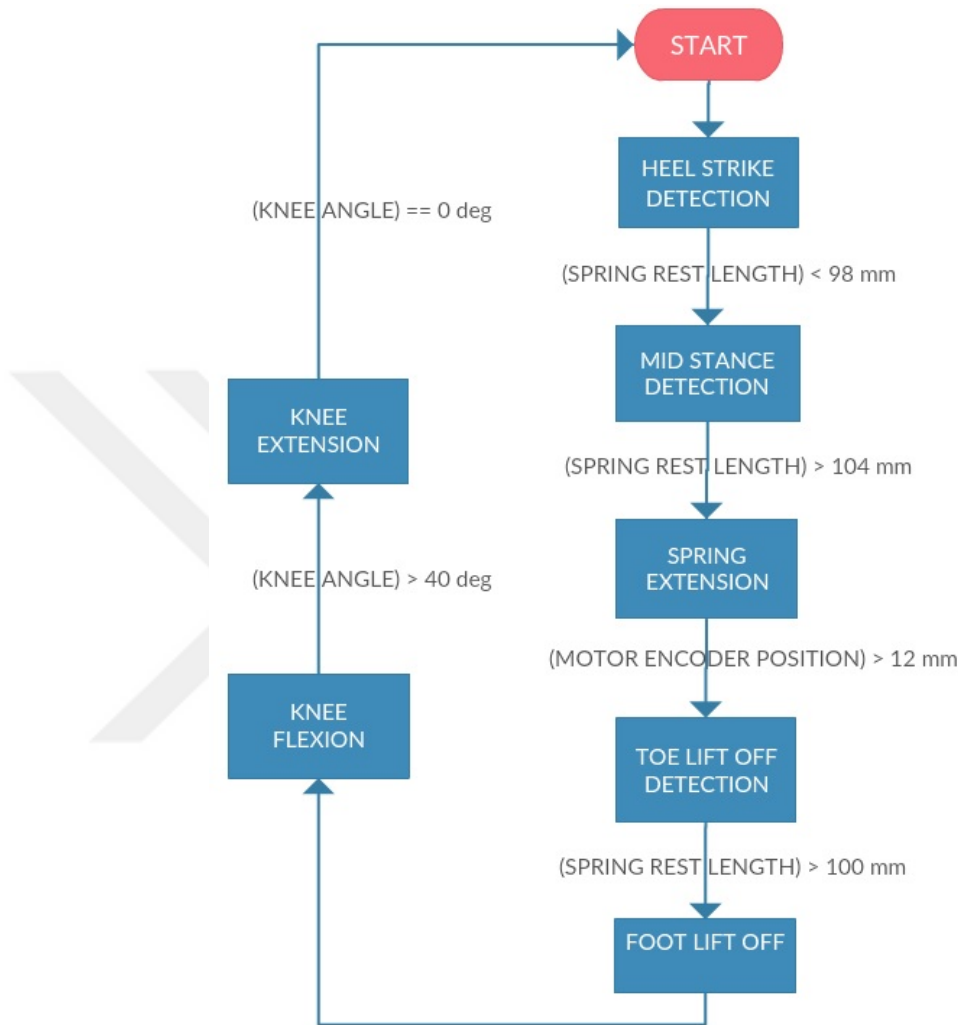
Figure 6.11: AAFO-AKO Control State Machine.

taken with AAFO-AKO system, respectively. In Fig. 6.13, the ankle motor extends the spring for 15 mm during Spring Extension state and lifts the foot up during Foot Lift-off state. In Fig. 6.14 heel strike is detected as the spring length decreases beyond 98 mm. Once the spring starts extending and reaches to 104 mm mid-stance phase is detected. Finally, toe lift-off event is detected when the spring length becomes 100 mm. During ankle roll-over the maximum amount of spring extension is observed to be 22.5 mm, which generates an approximate of 45 Nm of torque at the ankle during push-off. This torque corresponds to 30% of the torque required during ankle push-off, hence it helps propelling the body forward while decreasing energy loss due to ground collision. Finally, in Fig. 6.15
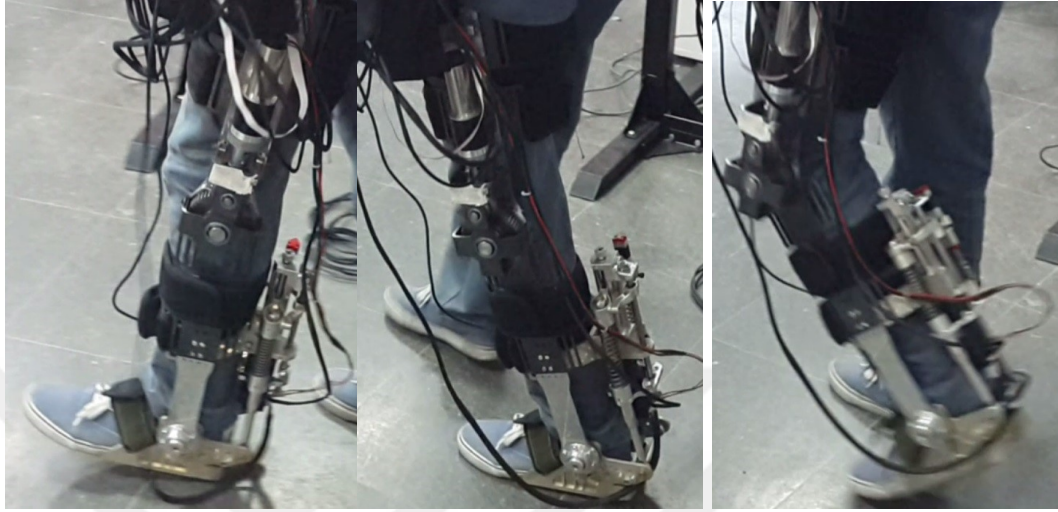
(a) Heel Strike Phase.   (b) Ankle Push-off Phase.   (c) Knee-Flexion Phase.

Figure 6.12: Walking Phases of the AAFO-AKO Test.

following Foot Lift-off state the motor of the knee joint is rotated in Knee Flexion state in order to flex the knee which prevents the collision of foot with ground. Then, the knee joint is extended with Knee Extension state helping the user for an effective leg swing.

The spring energy stored during stance phase both utilizes active motor input and walking kinematics through the lever. During the ankle push-off phase, this energy is injected to the body. Hence, this assistive energy propels the body forward while decreasing energy loss due to ground collision. The ankle joint of a healthy being generates 120-150 Nm of torque during walking. The integrated AAFO-AKO system can generate approximately 45 Nm of torque which compensates 40% of the required torque. Consecutively, the contribution of knee orthosis on walking is twofold. Firstly, during knee flexion it prevents toe dragging and secondly, knee extension assists leg swinging. Motivated by the idea of series elastic ankle ankle actuation our results state that the integrated system generates more effective walking pattern.
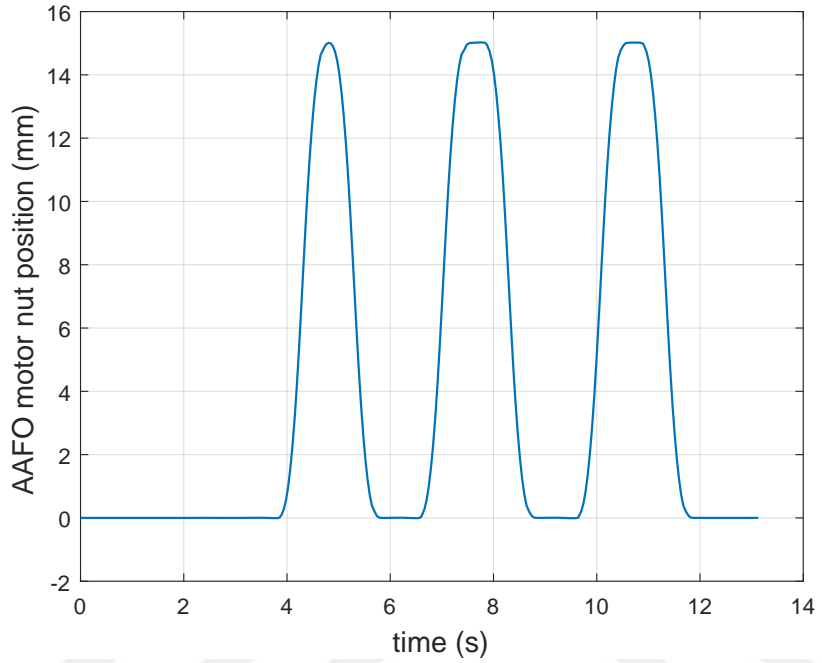
Figure 6.13: Ankle motor nut position of AAFO-AKO integrated system.
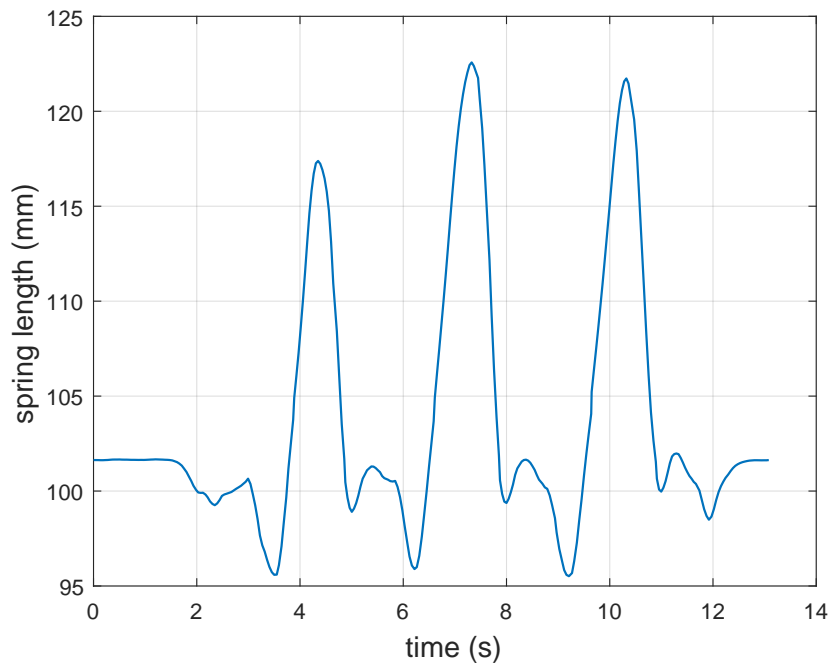
Figure 6.14: Spring length measurement of AAFO-AKO integrated system.
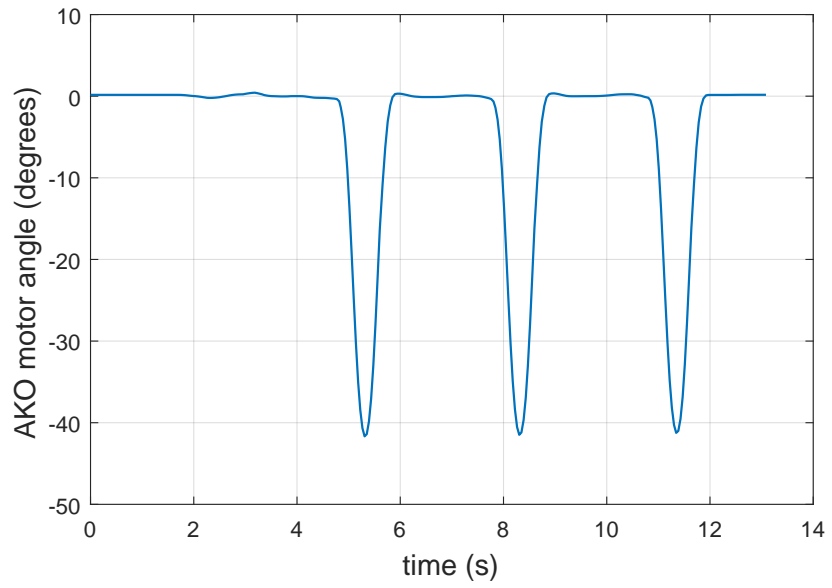
Figure 6.15: Knee motor angle of AAFO-AKO integrated system.

Chapter 7

Conclusion

The passive compass gait model captures the basic properties of biped walking without any actuation, however it depends on a downhill sloped ground. To overcome this limitation, we proposed a novel compass gait model called Ankle Actuated Compass Gait model which utilizes a precompressed ankle spring. The proposed model can walk over level ground and exhibits reasonable performance over significantly inclined and rough terrains.

Our model summarizes the action of the normally rotary ankle joint with a simplified prismatic joint. The spring situated in the ankle joint of the stance leg is activated immediately following the collision of the swing leg with the ground, modeling toe push-off similar to human walking. We derived equations of motion associated with all locomotory phases for this model, namely single stance dynamics, impulsive collision map and double stance dynamics, and we numerically implemented the resulting hybrid dynamics. Subsequently, we defined a Poincaré section at the highest point of the stance phase and used numerical methods to compute the associated Poincaré return map and its Jacobian. Fixed points of this map were then used to identify limit cycles of this system, with the eigenvalues of the corresponding Jacobian matrix leading to a careful characterization of limit cycle stability. Our results showed that the Ankle-Actuated Compass Gait model we proposed in this study exhibits locally asymptotically stable limit

cycles corresponding to feasible, sustained walking gaits on flat ground.

We extended our analysis by investigating the dependence of gait stability of level ground walking on the spring precompression realized prior to the swing leg collision. The increase in this precompression parameter eventually destabilizes period-1 limit cycles and introduces a regime of period doubling bifurcations. Period doublings evolve into non-periodic but sustained walking gaits and further increase of the precompression parameter results in unsustainable locomotion. We observed an interesting recovery of walking gaits for larger values of the spring precompression where a sustained but chaotic gait is reintroduced. Possible explanation for this behavior is due to the use of a unidirectional ankle spring to model the effects of the heel in our collision map. Further increase in the precompression parameter yields period-2^n through period-1 gaits. For both regions of bifurcating behavior, we showed that the ratio of distances between successive period doubling values converge to the Feigenbaum constant. Our results revealed that walking with a fixed spring precompression at each step does not always generate stable, period-1 walking behavior. Consequently, we implemented feedback control adjusting the ankle spring precompression, which enabled us to stabilize the otherwise unstable, period-1 fixed points, allowing explicit, stable control on the walking speed for the model.

We investigated the stability of the model on inclines surfaces by utilizing Poincaré methods. Our proposed model exhibits asymptotically stable limit cycles over uphill and downhill inclined grounds between slopes of -3.9^o and 4.45^o, respectively. We then, analyzed the dependence of gait stability as a function of ground slope and spring precompression parameters yielding a map of regions of period-doubling bifurcations as well as chaotic walking patterns. During downhill walking and for a given slope the increase in spring precompression parameter yields regions of period doubling bifurcations starting from period-1 up to chaotic walking patterns. However, interestingly, during uphill walking we observed period doubling bifurcation regimes in both increasing and decreasing directions of precompression variable. We then obtained several versions of this spring precompression versus ground slope map for the period-1 regions such as stance leg velocity at the apex instant and minimum eigenvalue of the Jacobian matrix.

These maps could be utilized to decide which spring precompression should be chosen during walking for a given desired slope or stance leg velocity. Furthermore we obtained the maximum amount of leg retraction for uphill and downhill slopes which could be utilized for platform implementations.

Since our model can walk over significant uphill and downhill slopes we wanted to test the performance of the model over rough terrains. In this respect, initially we generated random grounds composed of small ground segments where roughness of the overall ground can be adjusted by varying the angles of slope differences. The roughness of the ground can be varied from level ground to significantly rough terrain using truncated Gaussian distribution. Then, we evaluated the walking performance of our model on rough terrains as the ground roughness vary starting from level ground by using various slope based controllers such as midvalue, minimum eigenvalue, fixed precompression. Our results demonstrate that our model can walk over significantly rough terrains. We further improve the performance of our model by introducing a one-step-lookahead velocity feedback control along with ground slope feedback on the ankle spring precompression.

One of our long-term motivations in this research is our goal of implementing stable and energy efficient actuation methods for AAFO systems that can also be integrated with lower-extremity exoskeletons. Such platforms allow people with mobility disorders to stand and walk. In this context, existing research focuses on restoring only the functionalities of the knee and hip joints and ignore ankle joint despite its key role for the energetics and stability of walking. This lack of ankle actuation limits energetic efficiency for these platforms, and results in unnatural walking patterns. Our results provide a step in understanding parametric design and stability trade-offs in achieving dynamic walking with Series-Elastic Actuation on the ankle. In this respect, we built an experimental platform of active ankle foot orthosis enabling people with ankle and foot problems walk efficiently and naturally, over level, inclined and rough terrains. The experiments suggests that the assistive torque generated by the orthosis platform helps propelling the body during ankle push-off by compensating for the energy loss due to ground collision. Furthermore, we integrate the AAFO platform an active knee orthosis platform that is used by the patients who has knee locking and leg

swinging problems. The experimentation results suggest that the AAFO-AKO integrated system generates more effective walking pattern by actively controlling knee locking and leg swinging phases and by injecting energy to the body via SEA mechanism on the ankle.

To summarize, the main contributions of this thesis can be given as follows.

- We proposed a novel compass gait model called Ankle Actuated Compass Gait model.

- Hybrid dynamics of the proposed model are derived.

- We thoroughly explored and investigated the effect of ankle spring parameters on stability of walking which led to discovery of period doubling bifurcation behaviour.

- We proposed an active feedback controller on the spring precompression which stabilize gaits that were previously period 2^n, chaotic and unstable.

- The walking capabilities of the model is extended by introducing inclined grounds. Our model can walk on a large range of uphill and downhill sloped grounds.

- The performance of the model is evaluated on rough terrains by exploiting various controllers on the spring precompression.

- The principle of series elastic ankle actuation is realized with an active ankle foot orthosis platform which is intended for the patients having impaired ankle.

- The active ankle foot orthosis platform is integrated with an active knee orthosis platform. The resulting setup generates effective walking pattern.

In the near future, we plan to explore possible efficiency gains by adjusting the timing of toe push-off, that might enable the model to achieve approximate ground speed matching for the swing toe prior to its collision with the ground.

For walking over rough terrains various feedback controllers could be developed to improve the walking performance. We will explore the pediod-3 motions over a large range of model parameters. In the long term, we hope to conduct further experiments on the AAFO platform to verify our stability results and controllers, eventually leading to integration with full body lower extremity robotic orthosis platforms.

Bibliography

[1] T. McGeer, "Passive dynamic walking," *International Journal of Robotics Research*, vol. 9, pp. 62–82, Mar. 1990.

[2] M. Garcia, A. Chatterjee, A. Ruina, and M. Coleman, "The simplest walking model: Stability, complexity, and scaling," *ASME Journal of Biomechanical Engineering*, vol. 120, pp. 281–288, 1998.

[3] M. Garcia, A. Ruina, M. Coleman, and A. Chatterjee, "Passive-dynamic models of human gait," in *Proc. of the Conf. on Biomechanics and Neural Control of Movement*, pp. 32–33, 1996.

[4] A. D. Kuo, "Energetics of actively powered locomotion using the simplest walking model," *Journal of Biomechanical Engineering*, vol. 124, no. 1, pp. 113–120, 2002.

[5] A. Goswami, B. Espiau, and A. Keramane, "Limit cycles in a passive compass gait biped and passivity-mimicking control laws," *Autonomous Robots*, vol. 4, no. 3, pp. 273–286, 1997.

[6] A. Goswami, B. Espiau, and A. Keramane, "Limit cycles and their stability in a passive bipedal gait," in *Proc. of the IEEE Int. Conf. on Robotics and Automation*, vol. 1, pp. 246–251, 1996.

[7] R. Q. Van Der Linde, "Active leg compliance for passive walking," in *Proc. of the IEEE Int. Conf. on Robotics and Automation*, vol. 3, pp. 2339–2344, 1998.

[8] M. W. Spong and G. Bhatia, "Further results on control of the compass gait biped," in *Proc. of the IEEE/RSJ Int. Conf. on Intelligent Robots and Systems*, vol. 2, pp. 1933–1938, 2003.

[9] J. Ahn and N. Hogan, "A simple state-determined model reproduces entrainment and phase-locking of human walking," *PloS one*, vol. 7, no. 11, p. e47963, 2012.

[10] D. Maykranz and A. Seyfarth, "Compliant ankle function results in landing-take off asymmetry in legged locomotion," *Journal of Theoretical Biology*, vol. 349, pp. 44–49, 2014.

[11] P. A. Bhounsule, "Control of a compass gait walker based on energy regulation using ankle push-off and foot placement," *Robotica*, vol. 33, pp. 1314–1324, July 2015.

[12] F. Asano, Z.-W. Luo, and S. Hyon, "Parametric excitation mechanisms for dynamic bipedal walking," in *Proc. of the IEEE Int. Conf. on Robotics and Automation*, pp. 609–615, 2005.

[13] K. E. Zelik, T.-W. P. Huang, P. G. Adamczyk, and A. D. Kuo, "The role of series ankle elasticity in bipedal walking," *Journal of Theoretical Biology*, vol. 346, pp. 75–85, 2014.

[14] R. Ghorbani, *On controllable stiffness bipedal walking*. PhD thesis, The University of Manitoba, 2008.

[15] C. Tang, G. Yan, Z. Lin, Z. Wang, and Y. Yi, "Stable walking of 3d compass-like biped robot with underactuated ankles using discrete transverse linearization," *Transactions of the Institute of Measurement and Control*, vol. 37, no. 9, pp. 1074–1083, 2015.

[16] Z. Wang, G. Yan, C. Tang, Z. Lin, and Y. Miao, "Coupling mechanical design and control design for energy-efficient and stable walking of a compass-like biped," *Transactions of the Institute of Measurement and Control*, vol. 38, no. 3, pp. 253–265, 2016.

[17] A. Goswami, B. Thuilot, and B. Espiau, "A study of the passive gait of a compass-like biped robot: Symmetry and chaos," *The International Journal of Robotics Research*, vol. 17, no. 12, pp. 1282–1301, 1998.

[18] M. Garcia, A. Chatterjee, and A. Ruina, "Efficiency, speed, and scaling of two-dimensional passive-dynamic walking," *Dynamical Systems*, vol. 15, no. 2, pp. 75–99, 2000.

[19] R. Tedrake, T. W. Zhang, M.-f. Fong, and H. S. Seung, "Actuating a simple 3d passive dynamic walker," in *Proc. of the IEEE Int. Conf. on Robotics and Automation*, vol. 5, pp. 4656–4661, 2004.

[20] D. Hobbelen and M. Wisse, "Ankle actuation for limit cycle walkers," *The International Journal of Robotics Research*, vol. 27, no. 6, pp. 709–735, 2008.

[21] S. Collins and A. Ruina, "A bipedal walking robot with efficient and human-like gait," in *Proc. of the IEEE Int. Conf. on Robotics and Automation*, pp. 1983–1988, April 2005.

[22] D. Hobbelen, T. De Boer, and M. Wisse, "System overview of bipedal robots flame and tulip: Tailor-made for limit cycle walking," in *Proc. of the IEEE/RSJ Int. Conf. on Intelligent Robots and Systems*, pp. 2486–2491, 2008.

[23] S. H. Collins, M. Wisse, and A. Ruina, "A three-dimensional passive-dynamic walking robot with two legs and knees," *The International Journal of Robotics Research*, vol. 20, no. 7, pp. 607–615, 2001.

[24] K. Byl and R. Tedrake, "Approximate optimal control of the compass gait on rough terrain," in *Proc. of the IEEE Int. Conf. on Robotics and Automation*, pp. 1258–1263, 2008.

[25] P. N. Afshar and L. Ren, "Dynamic stability of passive bipedal walking on rough terrain: a preliminary simulation study," *Journal of Bionic Engineering*, vol. 9, no. 4, pp. 423–433, 2012.

[26] T. Erez and W. D. Smart, "Bipedal walking on rough terrain using manifold control," in *Intelligent Robots and Systems, 2007. IROS 2007. IEEE/RSJ International Conference on*, pp. 1539–1544, IEEE, 2007.

[27] H. Dai and R. Tedrake, "L 2-gain optimization for robust bipedal walking on unknown terrain," in *Robotics and Automation (ICRA), 2013 IEEE International Conference on*, pp. 3116–3123, IEEE, 2013.

[28] F. Iida and R. Tedrake, "Minimalistic control of a compass gait robot in rough terrain," in *Proc. of the IEEE Int. Conf. on Robotics and Automation*, pp. 1985–1990, 2009.

[29] J. Spitz, A. Evstrachin, and M. Zacksenhouse, "Minimal feedback to a rhythm generator improves the robustness to slope variations of a compass biped," *Bioinspiration & biomimetics*, vol. 10, no. 5, p. 056005, 2015.

[30] C. Tang, G. Yan, and Z. Lin, "Walking control for compass-like biped robot with underactuated ankle," in *Intelligent Control and Automation (WCICA), 2012 10th World Congress on*, pp. 3852–3857, IEEE, 2012.

[31] G. A. Pratt and M. M. Williamson, "Series elastic actuators," in *Intelligent Robots and Systems 95.'Human Robot Interaction and Cooperative Robots', Proceedings. 1995 IEEE/RSJ International Conference on*, vol. 1, pp. 399–406, IEEE, 1995.

[32] J. Hitt, A. M. Oymagil, T. Sugar, K. Hollander, A. Boehler, and J. Fleeger, "Dynamically controlled ankle-foot orthosis (DCO) with regenerative kinetics: Incrementally attaining user portability," in *Proc. of the IEEE Int. Conf. on Robotics and Automation*, pp. 1541–1546, 2007.

[33] A. M. Oymagil, J. K. Hitt, T. Sugar, and J. Fleeger, "Control of a regenerative braking powered ankle foot orthosis," in *Proc. of the IEEE Int. Conf. on Rehabilitation Robotics*, pp. 28–34, 2007.

[34] J. Blaya, H. Herr, *et al.*, "Adaptive control of a variable-impedance ankle-foot orthosis to assist drop-foot gait," *IEEE Trans. on Neural Systems and Rehabilitation*, vol. 12, no. 1, pp. 24–31, 2004.

[35] J. Hitt, T. Sugar, M. Holgate, R. Bellman, and K. Hollander, "Robotic transtibial prosthesis with biomechanical energy regeneration," *Industrial Robot: An International Journal*, vol. 36, no. 5, pp. 441–447, 2009.

[36] S. K. Au, J. Weber, and H. Herr, "Powered ankle–foot prosthesis improves walking metabolic economy," *IEEE Trans. on Robotics*, vol. 25, no. 1, pp. 51–66, 2009.

[37] J. W. Grizzle, G. Abba, and F. Plestan, "Asymptotically stable walking for biped robots: Analysis via systems with impulse effects," *IEEE Trans. on Automatic Control*, vol. 46, no. 1, pp. 51–64, 2001.

[38] D. Kerimoğlu, Ö. Morgül, and U. Saranlı, "Stability of a compass gait walking model with series elastic ankle actuation," in *Proc. of the Int. Conf. on Advanced Robotics*, pp. 351–356, July 2015.

[39] P. Holmes, "Poincaré, celestial mechanics, dynamical-systems theory and "chaos"," *Physics Reports*, vol. 193, pp. 137–163, Sept. 1990.

[40] D. Kerimoğlu, Ö. Morgül, and U. Saranlı, "Stability of planar compass gait walking with series elastic ankle actuation," in *Dynamic Walking Conference 2015, Columbus Ohio, USA*, 2015.

[41] S. H. Strogatz, *Nonlinear dynamics and chaos: with applications to physics, biology, chemistry, and engineering*. Westview press, 2014.

[42] D. Kerimoğlu, Ö. Morgül, and U. Saranlı, "Stability and control of planar compass gait walking with series-elastic ankle actuation," *Transactions of the Institute of Measurement and Control*, vol. 39, no. 3, pp. 312–323, 2017.

[43] H. Gritli, N. Khraief, and S. Belghith, "Period-three route to chaos induced by a cyclic-fold bifurcation in passive dynamic walking of a compass-gait biped robot," *Communications in Nonlinear Science and Numerical Simulation*, vol. 17, no. 11, pp. 4356–4372, 2012.

[44] D. Kerimoğlu, Ö. Morgül, and U. Saranlı, "Düzlemsel pergel yürüme modelinin bilekte seri yaylı eyleyici ile denetimi ve kararlılığı," in *Türkiye Otomatik Kontrol Konferansı (TOK) 2015 Denizli, Türkiye*, 2015.

[45] D. Kerimoğlu, Ö. Morgül, and U. Saranlı, "Pergel yürüme modelinin seri yaylı eyleyici ile denetimi," in *Türkiye Otonom Robotlar Konferansı (TORK) 2-3 Kasım 2016 Gedik Üniversitesi, İstanbul, Türkiye*, 2016.

[46] P. D. Neuhaus, J. H. Noorden, T. J. Craig, T. Torres, J. Kirschbaum, and J. E. Pratt, "Design and evaluation of mina: A robotic orthosis for paraplegics," in *Rehabilitation Robotics (ICORR), 2011 IEEE International Conference on*, pp. 1–8, IEEE, 2011.

[47] A. Esquenazi, M. Talaty, A. Packel, and M. Saulino, "The rewalk powered exoskeleton to restore ambulatory function to individuals with thoracic-level motor-complete spinal cord injury," *American journal of physical medicine & rehabilitation*, vol. 91, no. 11, pp. 911–921, 2012.

[48] H. A. Quintero, R. J. Farris, and M. Goldfarb, "Control and implementation of a powered lower limb orthosis to aid walking in paraplegic individuals," in *Rehabilitation Robotics (ICORR), 2011 IEEE International Conference on*, pp. 1–6, IEEE, 2011.

[49] D. A. Winter, *Biomechanics and motor control of human movement*. John Wiley & Sons, 2009.

[50] K. Endo and H. Herr, "A model of muscle-tendon function in human walking," in *Robotics and Automation, 2009. ICRA'09. IEEE International Conference on*, pp. 1909–1915, IEEE, 2009.

[51] K. A. Shorter, J. Xia, E. T. Hsiao-Wecksler, W. K. Durfee, and G. F. Kogler, "Technologies for powered ankle-foot orthotic systems: Possibilities and challenges," *IEEE/ASME Transactions on Mechatronics*, vol. 18, pp. 337–347, Feb. 2013.

[52] R. Jiménez-Fabián and O. Verlinden, "Review of control algorithms for robotic ankle systems in lower-limb orthoses, prostheses, and exoskeletons.," *Medical Engineering & Physics*, vol. 34, pp. 397–408, May 2012.

[53] J. L. Pons, *Wearable robots: biomechatronic exoskeletons*. John Wiley & Sons, 2008.

[54] J. A. Ward, T. G. Sugar, and K. W. Hollander, "Using the translational potential energy of springs for prosthetic systems," in *Control Applications (CCA), 2011 IEEE International Conference on*, pp. 1461–1467, IEEE, 2011.

Appendix A

General Collision Map for the AACG Model

In this section, we obtain the Lagrangian for three DOF AACG model with a released spring shown in Fig. 2.3 by writing the system kinetic and potential energy expressions as a function of $\boldsymbol{q}_c$ as follows

$$L = \frac{1}{8}\left(\frac{L_{11}}{L_{12}} + \frac{L_{21}}{L_{22}} + L_3\right). \tag{A.1}$$

$$
\begin{aligned}
L_{11} = {} & 2gl\cos(\theta_s(t))(-3d^4lm + r(t)^2(22d^2lm + 32l^3(2m+3M))) + 12d^2l^3m \\
& + 4r(t)^3(2d^2m + l^2(9m+16M)) + r(t)(-4d^4m + 28d^2l^2m + 8l^4(5m+8M)) \\
& + 8l^5(m+2M) + l(m+16M)r(t)^4 - 4mr(t)^5. \tag{A.2}
\end{aligned}
$$

$$L_{12} = \left(r(t)^2 - d^2\right)(l + r(t))(-d + 2l + r(t))(d + 2l + r(t)). \tag{A.3}$$

$$L_{21} = l((l + r(t))^2 \dot{\theta}_s(t)^2 + \dot{r}(t)^2)(-3d^4 lm + r(t)^2(22d^2 lm + 32l^3(2m + 3M))$$
$$+ 12d^2 l^3 m + 4r(t)^3(2d^2 m + l^2(9m + 16M)) + r(t)(-4d^4 m + 28d^2 l^2 m$$
$$+ 8l^4(5m + 8M)) + 8l^5(m + 2M) + l(m + 16M)r(t)^4 - 4mr(t)^5). \quad \text{(A.4)}$$

$$L_{22} = \left(r(t)^2 - d^2\right)(l + r(t))^2(-d + 2l + r(t))(d + 2l + r(t)). \quad \text{(A.5)}$$

$$L_3 = +4gm(l(\cos(\theta_n(t)) - 3\cos(\theta_s(t))) - 4r(t)\cos(\theta_s(t))) - 4k(r_o - r(t))^2$$
$$+ m((5l^2 + 12lr(t) + 8r(t)^2)\dot{\theta}_s(t)^2 + l^2\dot{\theta}_n(t)^2$$
$$- 4l(l + r(t))\dot{\theta}_s(t)\dot{\theta}_n(t)\cos(\theta_s(t) - \theta_n(t)) - 4l\dot{\theta}_n(t)\dot{r}(t)\sin(\theta_s(t) - \theta_n(t)) + 8\dot{r}(t)^2).$$
$$\text{(A.6)}$$

In order to obtain equations of motion for the model, we apply the following Lagrangian formula

$$\frac{d}{dt}\left(\frac{\partial L}{\partial \dot{\boldsymbol{q}}_c}\right) - \frac{\partial L}{\partial \boldsymbol{q}_c} = 0. \quad \text{(A.7)}$$

which yields (2.10). Then, we provide the open forms of the components of (2.10)

$$\mathbf{M}_c(\mathbf{q}_c)\ddot{\mathbf{q}}_c + \mathbf{B}_c(\mathbf{q}_c, \dot{\mathbf{q}}_c)\dot{\mathbf{q}}_c + \mathbf{G}_c(\mathbf{q}_c) = \mathbf{J}_c^T(\mathbf{q}_c)\mathbf{F}_I\delta(t - t_c) . \quad \text{(A.8)}$$

Here, $\mathbf{M}_c(\mathbf{q}_c)$ is given as

$$\mathbf{M}_c(\mathbf{q}_c) := \begin{bmatrix} \frac{M_{11}^n}{M_{11}^d} & M_{12} & M_{13} \\ M_{21} & M_{22} & M_{23} \\ M_{31} & M_{32} & \frac{M_{33}^n}{M_{33}^d} \end{bmatrix}, \quad \text{(A.9)}$$

where the components of $\mathbf{M}_c(\mathbf{q}_c)$ are given as follows.

$$M_{11}^n = (l + r(t))^2(-2d^4m + r(t)(8d^2lm + 2l^3(3m + 4M))$$
$$+ r(t)^2(4d^2m + l^2(4M - 3m)) + 8d^2l^2m + 2l^4(m + 2M)$$
$$- 8lmr(t)^3 - 2mr(t)^4). \tag{A.10}$$

$$M_{11}^d = (d^2 - r(t)^2)(d - 2l - r(t))(d + 2l + r(t)). \tag{A.11}$$

$$M_{12} = -\frac{1}{2}lm(l + r(t))\cos(\theta_s(t) - \theta_n(t)). \tag{A.12}$$

$$M_{13} = 0. \tag{A.13}$$

$$M_{21} = -\frac{1}{2}lm(l + r(t))\cos(\theta_s(t) - \theta_n(t)). \tag{A.14}$$

$$M_{22} = \frac{l^2m}{4}. \tag{A.15}$$

$$M_{23} = -\frac{1}{2}lm\sin(\theta_s(t) - \theta_n(t)). \tag{A.16}$$

$$M_{31} = 0. \tag{A.17}$$

$$M_{32} = -\frac{1}{2}lm\sin(\theta_s(t) - \theta_n(t)).s \tag{A.18}$$

$$M_{33}^n = 11d^4l^2m - 44d^2l^4m + r(t)^3(4l^3(15m - 16M) - 72d^2lm) + r(t)^4(l^2(103m$$
$$- 16M) - 16d^2m) + 4r(t)(5d^4lm - 31d^2l^3m - 2l^5(5m + 8M)) + 2r(t)^2(4d^4m$$
$$- 67d^2l^2m - 16l^4(m + 3M)) - 8l^6(m + 2M) + 52lmr(t)^5 + 8mr(t)^6.$$

$$(A.19)$$

$$M_{33}^d = 4(r(t)^2 - d^2)(l + r(t))^2(-d + 2l + r(t))(d + 2l + r(t)). \qquad (A.20)$$

The coriolis matrix, $\mathbf{B}_c(\mathbf{q}_c, \dot{\mathbf{q}}_c)\dot{\mathbf{q}}_c$ is given as

$$\mathbf{B}_c(\mathbf{q}_c, \dot{\mathbf{q}}_c)\dot{\mathbf{q}}_c := \begin{bmatrix} \frac{B_{11}^n}{B_{11}^d} & B_{12} & \frac{B_{13}^n}{B_{13}^d} \\ B_{21} & B_{22} & B_{23} \\ B_{31} & B_{32} & B_{33} \end{bmatrix}, \qquad (A.21)$$

where the components of $\mathbf{B}_c(\mathbf{q}_c, \dot{\mathbf{q}}_c)\dot{\mathbf{q}}_c$ are given as follows.

$$B_{11}^n = 2(l + r(t))\dot{r}(t)(r(t)^5(62l^3m - 48d^2lm) - 8m(d^2 - 6l^2)r(t)^6 + 4r(t)^3(12d^4lm$$
$$+ d^2l^3(8M - 23m) + l^5(5m + 8M)) + r(t)^4(12d^4m + 2d^2l^2(4M - 51m)$$
$$+ l^4(33m + 8M)) + r(t)^2(-8d^6m + 2d^4l^2(35m - 4M) + 4d^2l^4(m + 16M)$$
$$+ 8l^6(3m + 5M)) + 2lr(t)(-8d^6m + d^4l^2(25m - 8M) + 4d^2l^4(7m + 8M)$$
$$+ 4l^6(m + 2M)) + d^2(2d^6m - 16d^4l^2m + d^2l^4(27m - 8M) + 8l^6(2m + 3M))$$
$$+ 16lmr(t)^7 + 2mr(t)^8) \qquad (A.22)$$

$$B_{11}^d = (d^2 - r(t)^2)^2(-d + 2l + r(t))^2(d + 2l + r(t))^2. \qquad (A.23)$$

$$B_{12} = 0. \qquad (A.24)$$

$$B_{13}^n = 2(l + r(t))\dot{\theta}_s(t)(r(t)^5(62l^3m - 48d^2lm) - 8m(d^2 - 6l^2)r(t)^6 + 4r(t)^3(12d^4lm$$
$$+ d^2l^3(8M - 23m) + l^5(5m + 8M)) + r(t)^4(12d^4m + 2d^2l^2(4M - 51m)$$
$$+ l^4(33m + 8M)) + r(t)^2(-8d^6m + 2d^4l^2(35m - 4M) + 4d^2l^4(m + 16M)$$
$$+ 8l^6(3m + 5M)) + 2lr(t)(-8d^6m + d^4l^2(25m - 8M) + 4d^2l^4(7m + 8M)$$
$$+ 4l^6(m + 2M)) + d^2(2d^6m - 16d^4l^2m + d^2l^4(27m - 8M) + 8l^6(2m + 3M))$$
$$+ 16lmr(t)^7 + 2mr(t)^8) \tag{A.25}$$

$$B_{13} = (d^2 - r(t)^2)^2(-d + 2l + r(t))^2(d + 2l + r(t))^2. \tag{A.26}$$

$$B_{21} = -lm\dot{r}(t)\cos(\theta_s(t) - \theta_n(t)). \tag{A.27}$$

$$B_{22} = 0. \tag{A.28}$$

$$B_{23} = -lm\dot{\theta}_s(t)\cos(\theta_s(t) - \theta_n(t)). \tag{A.29}$$

$$B_{31} = 0. \tag{A.30}$$

$$B_{32} = 0. \tag{A.31}$$

$$B_{33} = 0. \tag{A.32}$$

$\mathbf{G}_c(\mathbf{q}_c)$ matrix is given as

$$\mathbf{G}_c(\mathbf{q}_c) := \begin{bmatrix} \frac{G_{11}}{G_{12}} \\ G_2 \\ \frac{G_{311} + G_{312}}{G_{32}} \end{bmatrix}, \tag{A.33}$$

where the components are given as follows.

$$
\begin{aligned}
G_{11} = {} & 2m(l\sin(\theta_s(t) - \theta_n(t))\dot{\theta}_n(t)^2 + 4g\sin(\theta_s(t)) + 8\dot{\theta}_s(t)\dot{r}(t))r(t)^{10} \\
& + 2lm(10l\sin(\theta_s(t) - \theta_n(t))\dot{\theta}_n(t)^2 + 41g\sin(\theta_s(t)) + 80\dot{\theta}_s(t)\dot{r}(t))r(t)^9 \\
& - (2l(4d^2 - 41l^2)m\sin(\theta_s(t) - \theta_n(t))\dot{\theta}_n(t)^2 + g(32md^2 + l^2(16M \\
& - 325m))\sin(\theta_s(t)) + 16(4d^2 - 41l^2)m\dot{\theta}_s(t)\dot{r}(t))r(t)^8 - 8l(2l(4d^2 \\
& - 11l^2)m\sin(\theta_s(t) - \theta_n(t))\dot{\theta}_n(t)^2 + g(33md^2 + l^2(16M - 77m))\sin(\theta_s(t)) \\
& + 2(32d^2 - 87l^2)m\dot{\theta}_s(t)\dot{r}(t))r(t)^7 + 4(l(3d^4 - 54l^2d^2 + 52l^4)m\sin(\theta_s(t) \\
& - \theta_n(t))\dot{\theta}_n(t)^2 + g(12md^4 + l^2(8M - 219m)d^2 + l^4(127m - 104M))\sin(\theta_s(t)) \\
& + 2(12md^4 + 2l^2(4M - 103m)d^2 + l^4(205m + 8M))\dot{\theta}_s(t)\dot{r}(t))r(t)^6 + 4l(2l(9d^4 \\
& - 50l^2d^2 + 16l^4)m\sin(\theta_s(t) - \theta_n(t))\dot{\theta}_n(t)^2 + g(75md^4 + 2l^2(24M - 191m)d^2 \\
& - 2l^4(3m + 88M))\sin(\theta_s(t)) + 8(18md^4 + 2l^2(6M - 43m)d^2 + l^4(37m \\
& + 12M))\dot{\theta}_s(t)\dot{r}(t))r(t)^5 - 2(2l(2d^6 - 47l^2d^4 + 108l^4d^2 - 8l^6)m\sin(\theta_s(t) \\
& - \theta_n(t))\dot{\theta}_n(t)^2 + g(16md^6 + l^2(8M - 393m)d^4 + 8l^4(89m - 32M)d^2 + 164l^6(m \\
& + 2M))\sin(\theta_s(t)) + 4(8md^6 + 2l^2(4M - 89m)d^4 + 2l^4(141m - 68M)d^2 - l^6(97m \\
& + 112M))\dot{\theta}_s(t)\dot{r}(t))r(t)^4 - 8l(2d^2l(2d^4 - 17l^2d^2 + 16l^4)m\sin(\theta_s(t) - \theta_n(t))\dot{\theta}_n(t)^2 \\
& + g(17md^6 + l^2(8M - 141m)d^4 + 32l^4(2m - 3M)d^2 + 8l^6(3m + 5M))\sin(\theta_s(t)) \\
& + 2(16md^6 + l^2(16M - 119m)d^4 + 14l^4(m - 8M)d^2 - 2l^6(19m \\
& + 32M))\dot{\theta}_s(t)\dot{r}(t))r(t)^3 + 2(d^2l(d^6 - 28l^2d^4 + 120l^4d^2 - 32l^6)m\sin(\theta_s(t) \\
& - \theta_n(t))\dot{\theta}_n(t)^2 + 2(g(2md^8 - 61l^2md^6 + l^4(247m - 24M)d^4 + 24l^6(2m + 7M)d^2 \\
& - 8l^8(m + 2M))\sin(\theta_s(t)) + 2(2md^8 - 56l^2md^6 + l^4(197m - 48M)d^4 + 12l^6(11m \\
& + 18M)d^2 + 8l^8(5m + 9M))\dot{\theta}_s(t)\dot{r}(t)))r(t)^2 + 2l(2l(d^4 - 12l^2d^2 + 32l^4)m\sin(\theta_s(t) \\
& - \theta_n(t))\dot{\theta}_n(t)^2d^4 + g(9md^6 - 108l^2md^4 + 4l^4(67m - 8M)d^2 + 32l^6(3m \\
& + 5M))\sin(\theta_s(t))d^2 + 16(md^8 - 12l^2md^6 + 2l^4(13m - 4M)d^4 + 2l^6(11m + 14M)d^2 \\
& + 2l^8(m + 2M))\dot{\theta}_s(t)\dot{r}(t))r(t) + d^2l^2(2d^2l(d^2 - 4l^2)^2m\sin(\theta_s(t) - \theta_n(t))\dot{\theta}_n(t)^2 \\
& + g(d^2 - 4l^2)(9md^4 - 36l^2md^2 - 8l^4(m + 2M))\sin(\theta_s(t)) + 8(2md^6 - 16l^2md^4 \\
& + l^4(27m - 8M)d^2 + 8l^6(2m + 3M))\dot{\theta}_s(t)\dot{r}(t)). \tag{A.34}
\end{aligned}
$$

$$
G_{12} = 4(l + r(t))(-d + 2l + r(t))^2(d + 2l + r(t))^2(d^2 - r(t)^2)^2. \tag{A.35}
$$

$$G_2 = \frac{1}{2}lm(g\sin(\theta_n(t)) + (l+r(t))\dot{\theta}_s(t)^2 \sin(\theta_s(t) - \theta_n(t)) + 2\dot{\theta}_s(t)\dot{r}(t)\cos(\theta_s(t) - \theta_n(t))).$$

$$\text{(A.36)}$$

$$
\begin{aligned}
G_{311} &= 4(k - 2m\dot{\theta}_s(t)^2)r(t)^{12} + 2(-48lm\dot{\theta}_s(t)^2 + lm\cos(\theta_s(t) - \theta_n(t))\dot{\theta}_n(t)^2 + 22kl \\
&\quad - 2kr_o + 4gm\cos(\theta_s(t)))r(t)^{11} + (-16kd^2 + 204kl^2 + 16(2d^2 - 31l^2)m\dot{\theta}_s(t)^2 \\
&\quad + 22l^2m\cos(\theta_s(t) - \theta_n(t))\dot{\theta}_n(t)^2 - 44klr_o + 88glm\cos(\theta_s(t)))r(t)^{10} + (516kl^3 \\
&\quad - 204kr_ol^2 + 429gm\cos(\theta_s(t))l^2 + 16gM\cos(\theta_s(t))l^2 + 8(40d^2 - 179l^2)m\dot{\theta}_s(t)^2l \\
&\quad + 2(51l^2 - 4d^2)m\cos(\theta_s(t) - \theta_n(t))\dot{\theta}_n(t)^2l - 2m\dot{r}(t)^2l - 144d^2kl + 16d^2kr_o \\
&\quad - 32d^2gm\cos(\theta_s(t)))r(t)^9 + (24kd^4 - 560kl^2d^2 + 144klr_od^2 - 288glm\cos(\theta_s(t))d^2 \\
&\quad + 768kl^4 - 4(12md^4 + 2l^2(4M - 171m)d^2 + l^4(635m + 8M))\dot{\theta}_s(t)^2 + 6l^2(43l^2 \\
&\quad - 12d^2)m\cos(\theta_s(t) - \theta_n(t))\dot{\theta}_n(t)^2 + 3l^2m\dot{r}(t)^2 + 16l^2M\dot{r}(t)^2 - 516kl^3r_o \\
&\quad + 1189gl^3m\cos(\theta_s(t)) + 144gl^3M\cos(\theta_s(t)))r(t)^8 + 4(168kl^5 - 192kr_ol^4 \\
&\quad + 521gm\cos(\theta_s(t))l^4 + 152gM\cos(\theta_s(t))l^4 + 20m\dot{r}(t)^2l^3 + 32M\dot{r}(t)^2l^3 - 308d^2kl^3 \\
&\quad + 140d^2kr_ol^2 - 271d^2gm\cos(\theta_s(t))l^2 + 8d^2gM\cos(\theta_s(t))l^2 + (3d^4 - 70l^2d^2 \\
&\quad + 96l^4)m\cos(\theta_s(t) - \theta_n(t))\dot{\theta}_n(t)^2l + 2d^2m\dot{r}(t)^2l + 42d^4kl - 4((183m + 16M)l^5 \\
&\quad + d^2(16M - 205m)l^3 + 24d^4ml)\dot{\theta}_s(t)^2 - 6d^4kr_o + 12d^4gm\cos(\theta_s(t)))r(t)^7 - 4(4kd^6 \\
&\quad - 130kl^2d^4 + 42klr_od^4 - 84glm\cos(\theta_s(t))d^4 + 416kl^4d^2 - 13l^2m\dot{r}(t)^2d^2 - 308kl^3r_od^2 \\
&\quad + 553gl^3m\cos(\theta_s(t))d^2 - 56gl^3M\cos(\theta_s(t))d^2 - 80kl^6 + (-8md^6 + 2l^2(167m \\
&\quad - 4M)d^4 - 24l^4(49m - 10M)d^2 + 2l^6(299m + 108M))\dot{\theta}_s(t)^2 - 7l^2(3d^4 - 22l^2d^2 \\
&\quad + 12l^4)m\cos(\theta_s(t) - \theta_n(t))\dot{\theta}_n(t)^2 - 78l^4m\dot{r}(t)^2 - 112l^4M\dot{r}(t)^2 + 168kl^5r_o \\
&\quad - 637gl^5m\cos(\theta_s(t)) - 392gl^5M\cos(\theta_s(t)))r(t)^6 - 2(-32kl^7 + 160kr_ol^6 \\
&\quad - 1220gm\cos(\theta_s(t))l^6 - 1320gM\cos(\theta_s(t))l^6 - 308m\dot{r}(t)^2l^5 - 448M\dot{r}(t)^2l^5 \\
&\quad + 688d^2kl^5 - 832d^2kr_ol^4 + 1228d^2gm\cos(\theta_s(t))l^4 - 384d^2gM\cos(\theta_s(t))l^4 \\
&\quad - 76d^2m\dot{r}(t)^2l^3 - 460d^4kl^3 + 260d^4kr_ol^2 - 493d^4gm\cos(\theta_s(t))l^2 + 24d^4gM\cos(\theta_s(t))l^2 \\
&\quad + 2(2d^6 - 65l^2d^4 + 208l^4d^2 - 40l^6)m\cos(\theta_s(t) - \theta_n(t))\dot{\theta}_n(t)^2l + 6d^4m\dot{r}(t)^2l + 40d^6kl \\
&\quad - 4(-(209m + 200M)l^7 + 4d^2(117m - 68M)l^5 + 3d^4(8M - 111m)l^3 + 24d^6ml)\dot{\theta}_s(t)^2 \\
&\quad - 8d^6kr_o + 16d^6gm\cos(\theta_s(t)))r(t)^5.
\end{aligned}
$$

$$\text{(A.37)}$$

$$
\begin{aligned}
G_{312} =\ & 2(2kd^8 - 88kl^2d^6 + 40klr_od^6 - 80glm\cos(\theta_s(t))d^6 \\
& + 512kl^4d^4 - 37l^2m\dot{r}(t)^2d^4 - 8l^2M\dot{r}(t)^2d^4 - 460kl^3r_od^4 + 801gl^3m\cos(\theta_s(t))d^4 \\
& - 120gl^3M\cos(\theta_s(t))d^4 - 320kl^6d^2 + 148l^4m\dot{r}(t)^2d^2 + 16l^4M\dot{r}(t)^2d^2 + 688kl^5r_od^2 \\
& - 488gl^5m\cos(\theta_s(t))d^2 + 800gl^5M\cos(\theta_s(t))d^2 - 2(2md^8 - 128l^2md^6 + l^4(851m \\
& - 120M)d^4 + 2l^6(400M - 103m)d^2 + l^8(289m + 440M))\dot{\theta}_s(t)^2 + 2l^2(-10d^6 + 115l^2d^4 \\
& - 172l^4d^2 + 8l^6)m\cos(\theta_s(t) - \theta_n(t))\dot{\theta}_n(t)^2 + 358l^6m\dot{r}(t)^2 + 552l^6M\dot{r}(t)^2 - 32kl^7r_o \\
& + 968gl^7m\cos(\theta_s(t)) + 1448gl^7M\cos(\theta_s(t)))r(t)^4 + 2(-8((41m + 72M)l^9 + 3d^2(27m \\
& + 64M)l^7 + 8d^4(23m - 5M)l^5 - 48d^6ml^3 + 2d^8ml)\dot{\theta}_s(t)^2 + d^2l(d^6 - 44l^2d^4 + 256l^4d^2 \\
& - 160l^6)m\cos(\theta_s(t) - \theta_n(t))\dot{\theta}_n(t)^2 + 2(k((3l - r_o)d^6 + (44l^2r_o - 52l^3)d^4 + 8l^4(23l \\
& - 32r_o)d^2 - 32l^6(l - 5r_o))d^2 + 2(2(31m + 52M)l^7 + 2d^2(25m + 8M)l^5 - 2d^4(11m \\
& + 4M)l^3 + d^6ml)\dot{r}(t)^2 + g(2md^8 - 89l^2md^6 + l^4(409m - 120M)d^4 + 8l^6(28m \\
& + 65M)d^2 + 16l^8(18m + 31M))\cos(\theta_s(t))))r(t)^3 + 2l(-8(2(7m + 13M)l^9 \\
& + d^2(81m + 116M)l^7 + 6d^4(18m - 5M)l^5 - 42d^6ml^3 + 3d^8ml)\dot{\theta}_s(t)^2 + d^2l(3d^6 \\
& - 52l^2d^4 + 184l^4d^2 - 32l^6)m\cos(\theta_s(t) - \theta_n(t))\dot{\theta}_n(t)^2 + 2(k(3(l - r_o)d^6 + 4l^2(13r_o \\
& - 8l)d^4 + 8l^4(10l - 23r_o)d^2 + 32l^6r_o)d^2 + (8(6m + 11M)l^7 + 12d^2(7m + 4M)l^5 \\
& - 2d^4(25m + 12M)l^3 + 5d^6ml)\dot{r}(t)^2 + g(6md^8 - 107l^2md^6 + l^4(281m - 120M)d^4 \\
& + 8l^6(41m + 51M)d^2 + 8l^8(13m + 24M))\cos(\theta_s(t))))r(t)^2 + l(64gm\cos(\theta_s(t))l^9 \\
& + 128gM\cos(\theta_s(t))l^9 + 32m\dot{r}(t)^2l^8 + 64M\dot{r}(t)^2l^8 + 608d^2gm\cos(\theta_s(t))l^7 \\
& + 704d^2gM\cos(\theta_s(t))l^7 + 160d^2m\dot{r}(t)^2l^6 + 128d^2M\dot{r}(t)^2l^6 + 64d^4kl^6 \\
& - 320d^4kr_ol^5 + 504d^4gm\cos(\theta_s(t))l^5 - 240d^4gM\cos(\theta_s(t))l^5 - 120d^4m\dot{r}(t)^2l^4 \\
& - 64d^4M\dot{r}(t)^2l^4 - 32d^6kl^4 + 128d^6kr_ol^3 - 272d^6gm\cos(\theta_s(t))l^3 - 8(4md^8 \\
& - 40l^2md^6 + l^4(79m - 24M)d^4 + 20l^6(3m + 4M)d^2 + 4l^8(m + 2M))\dot{\theta}_s(t)^2l^2 \\
& + 2d^4(3d^4 - 32l^2d^2 + 80l^4)m\cos(\theta_s(t) - \theta_n(t))\dot{\theta}_n(t)^2l^2 + 24d^6m\dot{r}(t)^2l^2 + 4d^8kl^2 \\
& - 12d^8kr_ol + 25d^8gm\cos(\theta_s(t))l - 2d^8m\dot{r}(t)^2)r(t) + d^2l^2(96gm\cos(\theta_s(t))l^7 \\
& + 128gM\cos(\theta_s(t))l^7 + 32m\dot{r}(t)^2l^6 + 32M\dot{r}(t)^2l^6 - 64d^2kr_ol^5 + 112d^2gm\cos(\theta_s(t))l^5 \\
& - 48d^2gM\cos(\theta_s(t))l^5 - 28d^2m\dot{r}(t)^2l^4 - 16d^2M\dot{r}(t)^2l^4 + 32d^4kr_ol^3 \\
& - 72d^4gm\cos(\theta_s(t))l^3 + 2d^2(d^2 - 4l^2)^2m\cos(\theta_s(t) - \theta_n(t))\dot{\theta}_n(t)^2l^2 + 8d^4m\dot{r}(t)^2l^2 \\
& - 4d^6kr_ol + 9d^6gm\cos(\theta_s(t))l - 4(8(2m + 3M)l^8 + d^2(27m - 8M)l^6 - 16d^4ml^4 \\
& + 2d^6ml^2)\dot{\theta}_s(t)^2 - d^6m\dot{r}(t)^2). \qquad 108 \qquad\qquad\qquad (A.38)
\end{aligned}
$$

$$G_{32} = 4(l + r(t))^3(-d + 2l + r(t))^2(d + 2l + r(t))^2(d^2 - r(t)^2)^2. \qquad \text{(A.39)}$$

We, then present detailed expressions for the collision map, mapping velocities before and after the collision event with $\dot{\mathbf{q}}_c^+ = \mathbf{H}_c(\mathbf{q}_c^-)\dot{\mathbf{q}}_c^-$. We define

$$\boldsymbol{H_c} := \frac{1}{H_d} \begin{bmatrix} H_{11} & H_{12} & H_{13} \\ H_{21} & H_{22} & H_{23} \\ H_{31} & H_{32} & H_{33} \end{bmatrix}, \qquad \text{(A.40)}$$

whose components are obtained from (2.17) to yield

$$H_d := -l^2(7m + 8M) - 16l(m + M)r^- - 2(5m + 4M)(r^-)^2$$
$$+ ml(3l + 4r^-)\cos(2(\theta_s^- - \theta_n^-)), \qquad \text{(A.41)}$$

and

$$H_{11} := -2\cos(\theta_s^- - \theta_n^-)^2(l^2(3m + 4M) + 8l(m + M)r^- + 2(3m + 2M)(r^-)^2)$$

$$H_{12} := 2ml\cos(\theta_s^- - \theta_n^-)(l + r^-)$$

$$H_{13} := -(6m + 4M)(l + r^-)\sin(2(\theta_s^- - \theta_n^-))$$

$$H_{21} := -2\cos(\theta_s^- - \theta_n^-)(l + r^-)(l^2(3m + 4M) + 8l(m + M)r^- + (6m + 4M)(r^-)^2)/l$$

$$H_{22} := 2m(l + r^-)^2$$

$$H_{23} := -4(3m + 2M)(l + r^-)^2\sin(\theta_s^- - \theta_n^-)/l$$

$$H_{31} := -(l + r^-)\sin(2(\theta_s^- - \theta_n^-))(l^2(3m + 4M) + (6m + 4M)(r^-)^2)$$

$$H_{32} := 2ml(l + r^-)^2\sin(\theta_s^- - \theta_n^-)$$

$$H_{33} := -(12m + 8M)(l + r^-)^2\sin(\theta_s^- - \theta_n^-)^2.$$

This general form of the collision map is further simplified for the AACG model, whose single stance ends with $r^- = 0$ and $\dot{r}^- = 0$ to yield the simplified map of (2.18).

Appendix B

Dynamics of the Double Support Phase for the AACG Model

We present the Lagrangian of the single DOF AACG model having both legs fixated to the ground with a released spring.

$$
\begin{aligned}
L = \frac{1}{2}\Big(&-gm\big((l + 2r(t))\sin(\cos^{-1}(\frac{d^2 + 2lr(t) + r(t)^2}{2dl + 2dr(t)}) + \phi) \\
&+ l\cos(\csc^{-1}(\frac{2dl}{d^2 - r(t)(2l + r(t))}) + \phi) + 2d\sin(\phi)\big) \\
&- 2gM(l\cos(\csc^{-1}(\frac{2dl}{d^2 - r(t)(2l + r(t))}) + \phi) + d\sin(\phi)) \\
&- \frac{4l^2 M(l + r(t))^2 \dot{r}(t)^2}{(d^2 - r(t)^2)(d - 2l - r(t))(d + 2l + r(t))} \\
&- \frac{L_1}{4(r(t)^2 - d^2)(l + r(t))^2(-d + 2l + r(t))(d + 2l + r(t))} - k(r_o - r(t))^2).
\end{aligned}
$$

$$\text{(B.1)}$$

$$
\begin{aligned}
L_1 = lm\dot{r}(t)^2\big(&-3d^4 l + 12d^2 l^3 + r(t)(-4d^4 + 28d^2 l^2 + r(t)(r(t)(8d^2 + 36l^2 + r(t)(l \\
&- 4r(t))) + 22d^2 l + 64l^3) + 40l^4) + 8l^5\big).
\end{aligned}
$$

$$\text{(B.2)}$$

The general form of equations of motion for the single DOF double support phase is given as follows,

$$\mathbf{M}_r(\mathbf{q}_r)\ddot{\mathbf{q}}_r + \mathbf{B}_r(\mathbf{q}_r, \dot{\mathbf{q}}_r)\dot{\mathbf{q}}_r + \mathbf{G}_r(\mathbf{q}_r) = 0. \tag{B.3}$$

Here, $\mathbf{M}_r(\mathbf{q}_r)$ is given as

$$\mathbf{M}_r(\mathbf{q}_r) = -\frac{M_r^n}{4(r(t)^2 - d^2)(l + r(t))^2(-d + 2l + r(t))(d + 2l + r(t))}. \tag{B.4}$$

$$
\begin{aligned}
M_r^n = & \, l(-3d^4 lm + r(t)^2(22d^2 lm + 32l^3(2m + 3M)) + 12d^2 l^3 m + 4r(t)^3(2d^2 m \\
& + l^2(9m + 16M)) + r(t)(-4d^4 m + 28d^2 l^2 m + 8l^4(5m + 8M)) + 8l^5(m + 2M) \\
& + l(m + 16M)r(t)^4 - 4mr(t)^5).
\end{aligned} \tag{B.5}
$$

$$\mathbf{B}_r(\mathbf{q}_r, \dot{\mathbf{q}}_r) = \frac{B_r^n \dot{\mathbf{q}}_r}{4(d^2 - r(t)^2)^2(l + r(t))^3(-d + 2l + r(t))^2(d + 2l + r(t))^2}. \tag{B.6}$$

$$
\begin{aligned}
B_r^n = & \, l(-d^2 + 2l^2 + 2lr(t) + r(t)^2)(r(t)^5(6d^2 m + 2l^2(35m + 48M)) + lr(t)^4(d^2(47m \\
& + 16M) + 2l^2(79m + 112M)) + r(t)^2(-15d^4 lm + 32d^2 l^3(4m + 3M) + 16l^5(5m \\
& + 9M)) + r(t)^3(-6d^4 m + 4d^2 l^2(29m + 16M) + 32l^4(5m + 8M)) + d^2 l(d^4 m \\
& - 6d^2 l^2 m + 16l^4(m + M)) + 2r(t)(d^6 m - 9d^4 l^2 m + 4d^2 l^4(9m + 8M) + 8l^6(m \\
& + 2M)) + l(7m + 16M)r(t)^6 - 2mr(t)^7).
\end{aligned} \tag{B.7}
$$

$$\mathbf{G}_r(\mathbf{q}_r) = \frac{G_r^n}{G_r^{d1} G_r^{d2}}. \tag{B.8}$$

$$G_r^n = 2(\sqrt{\frac{(d^2 - r(t)^2)(-d^2 + 4l^2 + r(t)^2 + 4lr(t))}{d^2(l + r(t))^2}}(g(m + 2M)\sin(\phi$$

$$+ \csc^{-1}(\frac{2dl}{d^2 - r(t)(2l + r(t))})) + dk\sqrt{\frac{(d^2 - r(t)^2)(-d^2 + 4l^2 + r(t)^2 + 4lr(t))}{d^2 l^2}})$$

$$- gm\cos(\phi + \cos^{-1}(\frac{d^2 + r(t)^2 + 2lr(t)}{2dl + 2dr(t)}))\sqrt{\frac{(d^2 - r(t)^2)(-d^2 + 4l^2 + r(t)^2 + 4lr(t))}{d^2 l^2}})r(t)^3$$

$$+ (2\sqrt{\frac{(d^2 - r(t)^2)(-d^2 + 4l^2 + r(t)^2 + 4lr(t))}{d^2(l + r(t))^2}}(3gl(m + 2M)\sin(\phi$$

$$+ \csc^{-1}(\frac{2dl}{d^2 - r(t)(2l + r(t))})) + dk(2l - r_o)\sqrt{\frac{(d^2 - r(t)^2)(-d^2 + 4l^2 + r(t)^2 + 4lr(t))}{d^2 l^2}}$$

$$+ dgm\sin(\phi + \cos^{-1}(\frac{d^2 + r(t)^2 + 2lr(t)}{2dl + 2dr(t)}))\sqrt{\frac{(d^2 - r(t)^2)(-d^2 + 4l^2 + r(t)^2 + 4lr(t))}{d^2 l^2}})$$

$$- 5glm\cos(\phi + \cos^{-1}(\frac{d^2 + r(t)^2 + 2lr(t)}{2dl + 2dr(t)}))\sqrt{\frac{(d^2 - r(t)^2)(-d^2 + 4l^2 + r(t)^2 + 4lr(t))}{d^2 l^2}})r(t)^2$$

$$+ 2(g(d^2 - 3l^2)m\cos(\phi +$$

$$\cos^{-1}(\frac{d^2 + r(t)^2 + 2lr(t)}{2dl + 2dr(t)}))\sqrt{\frac{(d^2 - r(t)^2)(-d^2 + 4l^2 + r(t)^2 + 4lr(t))}{d^2 l^2}} + l(3gl(m$$

$$+ 2M)\sin(\phi + \csc^{-1}(\frac{2dl}{d^2 - r(t)(2l + r(t))})) + dk(l$$

$$- 2r_o)\sqrt{-\frac{(d^2 - r(t)^2)(d^2 - 4l^2 - r(t)^2 - 4lr(t))}{d^2 l^2}} + 2dgm\sin(\phi$$

$$+ \cos^{-1}(\frac{d^2 + r(t)^2 + 2lr(t)}{2dl + 2dr(t)}))V_1)\sqrt{\frac{(d^2 - r(t)^2)(-d^2 + 4l^2 + r(t)^2 + 4lr(t))}{d^2(l + r(t))^2}})r(t)$$

$$+ l(g(d^2 - 2l^2)m\cos(\phi + \cos^{-1}(\frac{d^2 + r(t)^2 + 2lr(t)}{2dl + 2dr(t)}))V_1$$

$$- 2l\sqrt{\frac{(d^2 - r(t)^2)(-d^2 + 4l^2 + r(t)^2 + 4lr(t))}{d^2(l + r(t))^2}}(-gl(m + 2M)\sin(\phi$$

$$+ \csc^{-1}(\frac{2dl}{d^2 - r(t)(2l + r(t))})) - dgm\sqrt{-\frac{(d^2 - r(t)^2)(d^2 - 4l^2 - r(t)^2 - 4lr(t))}{d^2 l^2}}\sin(\phi$$

$$+ \cos^{-1}(\frac{d^2 + r(t)^2 + 2lr(t)}{2dl + 2dr(t)})) + dkr_o\sqrt{-\frac{(d^2 - r(t)^2)(d^2 - 4l^2 - r(t)^2 - 4lr(t))}{d^2 l^2}})).$$

$$(B.9)$$

$$V_1 = \sqrt{-\frac{(d^2 - r(t)^2)(d^2 - 4l^2 - r(t)^2 - 4lr(t))}{d^2l^2}}. \qquad \text{(B.10)}$$

$$G_r^{d1} = 2d(l + r(t))^2 \sqrt{-\frac{(r(t)^2 - d^2)(-d^2 + 4l^2 + r(t)^2 + 4lr(t))}{d^2l^2}}. \qquad \text{(B.11)}$$

$$G_r^{d2} = \sqrt{-\frac{(r(t)^2 - d^2)(-d^2 + 4l^2 + r(t)^2 + 4lr(t))}{d^2(l + r(t))^2}}. \qquad \text{(B.12)}$$